

Electronic Thesis and Dissertation Repository

8-19-2021 10:30 AM

X-ray Absorption Spectroscopy, and Optical Luminescence Studies of Undoped and P-doped ZnO Nano/Microparticles

Zhi Liang Dong, *The University of Western Ontario*

Supervisor: Sham, Tsun-Kong, *The University of Western Ontario*

A thesis submitted in partial fulfillment of the requirements for the Master of Science degree in Chemistry

© Zhi Liang Dong 2021

Follow this and additional works at: <https://ir.lib.uwo.ca/etd>

Recommended Citation

Dong, Zhi Liang, "X-ray Absorption Spectroscopy, and Optical Luminescence Studies of Undoped and P-doped ZnO Nano/Microparticles" (2021). *Electronic Thesis and Dissertation Repository*. 8052. <https://ir.lib.uwo.ca/etd/8052>

This Dissertation/Thesis is brought to you for free and open access by Scholarship@Western. It has been accepted for inclusion in Electronic Thesis and Dissertation Repository by an authorized administrator of Scholarship@Western. For more information, please contact wlsadmin@uwo.ca.

Abstract

Over the past decades, Zinc Oxide (ZnO) semiconductor and its derivatives have been extensively developed because of its optoelectronic properties. Since ZnO is an intrinsic n-type semiconductor; therefore, how to synthesize high-quality p-type ZnO semiconductors and investigate their optoelectronic properties and local chemical structures are important and necessary. This thesis presents two studies of synthesizing both undoped and phosphorus doped ZnO microstructures by hydrothermal method and Vapor-Liquid-Solid (VLS) technique, respectively. The local chemical structure and the optical properties of both undoped and P-doped ZnO microparticles are determined by the X-ray absorption near-edge structures (XANES) and X-ray excited optical luminescence (XEOL) technique, respectively. As a result, the P-doped into ZnO lattice and substitute the Zn. The P-doped ZnO products have better crystallinity and less oxygen-based surface defect than the undoped ZnO products. The bandgap for the undoped ZnO are 3.20 and 3.22eV. The bandgap for P-doped ZnO is 3.21eV.

Keywords:

ZnO nano/microparticles, hydrothermal method, chemical vapor deposition (CVD), X-ray absorption near edge structures (XANES), X-ray excited optical luminescence (XEOL), surface defect

Summary for Lay Audience

Zinc Oxide (ZnO) is one of the important II-VI semiconductors and remains a popular research topic in today's scientific field due to its optoelectronic properties such as photocatalytic and intrinsic n-type semiconductor properties. It is a versatile wide bandgap semiconductor that has been used widely for a range of applications including sensors, lasers and photovoltaic devices. With a wide bandgap of 3.4 eV and a large exciton binding energy of 60 meV, ZnO has been recognized as one of the most promising materials in the next generation optoelectronic devices area. In this thesis, two studies of synthesizing both undoped and P-doped ZnO nano/microstructures by hydrothermal method and chemical vapor deposition (CVD) technique are presented. Two laboratory techniques and two synchrotron-based techniques are used for characterization in this thesis. Scanning electron microscopy (SEM) and laboratory X-ray diffraction (XRD) are used to track the surface morphology and the crystalline structure of both undoped and P-doped ZnO nano/microstructures, respectively. X-ray absorption near-edge structures (XANES) and X-ray excited optical luminescence (XEOL) are also used to determine the local chemical information of both undoped and P-doped ZnO nano/microstructures such as local symmetry and optical properties. It is found that the P is successfully doped into the ZnO lattice. The P-doped ZnO products have better crystallinity and less oxygen-based surface defect than the undoped ZnO products. The bandgap for the undoped ZnO structure prepared by the hydrothermal method and the CVD technique are 3.20 and 3.22eV, respectively. The bandgap for P-doped ZnO structure prepared by the CVD technique is 3.21eV.

Co-Authorship Statement

The X-ray absorption near-edge structures (XANES) measurement across Zn K -edge of both undoped and P-doped ZnO nano/microstructures in Chapter 3 were carried out with the help of Dr. Zou Finfroock and Dr. Debora Motta Meira at the Beamline 20-BM of Advanced Photon Source (APS). The XANES measurement across and Zn L_{3,2}-edge and O K-edge of both undoped and P-doped ZnO nano/microstructures in Chapter 3 were carried out with the help of Dr. Tom Regier and Dr. Zachary Arthur at the spherical grating monochromator (SGM) beamline of the Canadian Light Source (CLS). The XANES measurement across P K-edge of P-doped ZnO nano/microstructures in Chapter 3 and chapter 4 were carried out with the help of Dr. Yongfeng Hu and Dr. Mohsen Shakouri at the Soft X-Ray Microcharacterization Beamline (SXRMB) of CLS. The XANES and X-ray excited optical luminescence (XEOL) measurements across Zn K-edge of both undoped and P-doped ZnO nano/microstructures in Chapter 4 were carried out with the help of Dr. Bi-Hsuan Lin and f Lo-Yueh Chang at the 23A X-ray Nanoprobe beamline of Taiwan Photon Source (TPS). The XEOL measurements across Zn K-edge of undoped ZnO nano/microstructures in Chapter 3 were also were carried out with the help of Dr. Bi-Hsuan Lin and f Lo-Yueh Chang at the 23A X-ray Nanoprobe beamline of TPS.

The laboratory XRD data in Chapter 3 and Chapter 4 were collected with the help of Ms. Kim Law at the Department of Earth Science, University of Western Ontario (UWO). The scanning electron microscopy (SEM) images of both undoped and P-doped ZnO nano/microstructures in Chapter 3 and Chapter 4 were collected with the help of Dr. Todd Simpson and Mr. Tim Goldhawk at Nanofabrication Faculty, UWO.

Acknowledgments

First, I would like to express my most sincere thanks to my supervisor, Dr. Tsun-Kong Sham for his altruistic guidance and help during my graduate education career. His kindness and patience make me successfully transition from an undergraduate student to a graduate student and learn a lot of things as well. It is my great pleasure to work with a supervisor like him, and I extremely appreciate what he has offered me.

Next, I would like to thank my current group members: Dr. YunMui Yiu, Dr. Zhiqiang Wang, Dr. Weihan Li, Dr. Jiatang Chen, Mr. Xuchun Wang, Ms. Minsi Li, Ms. Xuejie Gao, Ms. Shumin Zhang, Mr. Yipeng Sun, Mr. Jiamin Fu for their helpful suggestions and constructive feedback.

At the meantime, I want to thank the technical support provided by the following people: Dr. Tom Regier, Dr. Zachary Arthur, Dr. Yongfeng Hu and Dr. Mohsen Shakouri from CLS, Dr. Zou Finfroock and Dr. Debora Motta Meira from APS, Dr. Bi-Hsuan Lin and Lo-Yueh Chang from TPS, Ms. Kim Law at Department of Earth Science, Dr. Todd Simpson and Mr. Tim Goldhawk at Nanofabrication Faculty from UWO.

Research at the University of Western Ontario is supported by the fund from the Natural Science and Engineering Research Council of Canada (NSERC), Canadian Research Chair (CRC) program, Canada Foundation for Innovation (CFI). The CLS is funded by NSERC, National Research Council (NRC), Canadian Institutes of Health Research (CIHR) and the University of Saskatchewan.

Last but not least, I would like to thank my family members especially my parent. Without their altruistic support and continuous encouragement, I cannot finish my academic career with an active and healthy mindset. Therefore, I also would like to appreciate what they did to me. I also want to thank my friends for providing help and comfort when I feel low.

Table of Content

ABSTRACT	I
SUMMARY FOR LAY AUDIENCE	II
CO-AUTHORSHIP STATEMENT	III
ACKNOWLEDGMENTS	IV
TABLE OF CONTENT	V
LIST OF TABLES	VIII
LIST OF FIGURES	IX
LIST OF ABBREVIATIONS	XII
CHAPTER 1	1
1. Introduction	1
1.1. Zinc Oxide.....	1
1.1.1 Background.....	1
1.1.2 Crystal Structure.....	1
1.1.3 P-type ZnO semiconductor synthesise limitations and solutions	2
1.2. Synthesis method of ZnO nanoparticles.....	5
1.2.1 Hydrothermal method.....	5
1.2.2 Chemical Vapor Deposition (CVD) method via Vapor-Liquid-Solid (VLS) mechanism	9
1.3. Introduction to synchrotron radiation technique	11
1.4. Objective and arrangement of thesis	17
1.5. Reference.....	17

CHAPTER 2.....	23
2. Synchrotron Radiation Facilities and Characterization Techniques.....	23
2.1. Synchrotron radiation facilities and beamlines	23
2.1.1. Canadian Light Source (CLS)	23
2.1.1.1. High Resolution Spherical Grating Monochromator (SGM) at CLS	24
2.1.1.2. Soft X-ray Microcharacterization Beamline (SXRMB) at CLS	25
2.1.2. Taiwan Photon Source (TPS)	25
2.1.2.1. 23A X-ray Nanoprobe.....	26
2.1.3. The Advanced Photon Source (APS)	28
2.1.3.1. Spectroscopy: Beamline 20-BM.....	28
2.2. Synchrotron Based Technique	29
2.2.1. The X-ray absorption fine structures (XAFS)	29
2.2.2. Detection Mode	33
2.2.3. X-ray Excited Optical Luminescence (XEOL)	36
2.3. Other Characterization Methods	38
2.3.1 X-ray Diffraction (XRD)	38
2.3.2. Scanning Electron Microscopy (SEM) and Energy Dispersive X-ray (EDX)	39
2.4. Reference.....	41
 CHAPTER 3.....	 44
3 XANES and XEOL studies of both undoped and P-doped ZnO nano/microparticles prepared by hydrothermal method.....	44
3.1. Introduction	44
3.2. Experimental	45
3.2.1. Synthesis of both undoped and P-doped ZnO particles.....	45
3.2.2. Characterization.....	47
3.3. Results and discussion.....	48
3.3.1. SEM.....	48
3.3.2. EDX.....	51
3.3.3. XRD.....	52

3.3.4. XANES	54
3.3.5. XEOL.....	60
3.4. Conclusion.....	61
3.5. Reference.....	62
CHAPTER 4.....	64
4. XANES and XEOL studies of both undoped and P-doped ZnO nano/microparticles prepared by chemical vapor deposition (CVD) method via vapor-liquid-solid (VLS) mechanism	64
4.1. Introduction	64
4.2. Experimental	65
4.2.1. Synthesis of both undoped and P-doped ZnO particles.....	65
4.2.2. Characterization.....	67
4.3. Results and Discussion.....	67
4.3.1. XRD.....	67
4.3.2. SEM.....	69
4.3.3. EDX.....	73
4.3.4. XANES	75
4.3.5. XEOL.....	79
4.4. Conclusion.....	83
4.5. Reference:.....	85
CHAPTER 5.....	87
5. Summary and Future Work	87
5.1. Summary	87
5.2. Future Work	90
5.3. Reference:.....	91
CURRICULUM VITAE.....	92

List of Tables

Table 3-1. A summary of sample names, descriptions, reaction temperatures and $\text{NH}_4\text{H}_2\text{PO}_4$ concentrations for each sample.	46
Table 3-2. A summary of the morphology and the average diameter of undoped and P-doped ZnO prepared via hydrothermal method.	49
Table 3-3. A summary of atomic percentage and percentage ratio for zinc, oxygen and phosphorus of ZnO: p-100-2 and ZnO: p-100-1.5.....	51
Table 4-1. A summary of all sample names, descriptions, gas flow rates and substrate position distances for all ZnO samples	66
Table 4-2. A summary of the morphology and the average diameter of undoped and P-doped ZnO prepared via CVD technique.....	71
Table 4-3. A summary of atomic percentage and percentage ratio for zinc, oxygen and phosphorus of ZnO: p-75-16 and ZnO: p-80-16.....	73

List of Figures

Figure 1-1. Stick-and-ball representation of ZnO crystal structure: hexagonal wurtzite and cubic zincblende. White and blue spheres denote Zn and O respectively [6].....	2
Figure 1-2. The difference among the insulator, semiconductor, and metal	3
Figure 1-3. The different position of the Fermi level in p-type and n-type semiconductor respectively.....	4
Figure 1-4. Autoclaves have been used during hydrothermal experiments.....	6
Figure 1-5. Schematic illustration of the general experimental preparation and procedure for the ZnO hydrothermal synthesis.....	8
Figure 1-6. Schematic illustration of the general experimental set up for the CVD technique via VLS mechanism	10
Figure 1-7. Schematic illustration of the general growth mechanism for the ZnO via VLS mechanism.....	11
Figure 1-8. The schematic diagram of the CLS SR facility [45].....	12
Figure 1-9. The schematic illustration of the spatial distribution of the photons emitted from the bending magnet, wiggler and undulator (left panel) and the energy distribution in a flux vs energy plot (right panel) [46, 47].	14
Figure 1-9. Schematic diagram of a grating monochromator with rotated positions	15
Figure 1-10. (a)Schematic illustration of a double-crystal monochromator, (b)illustration of Bragg diffraction	16
Figure 2-1. The schematic layout of the CLS experiment hall [2]	23
Figure 2-2. The layout of the SGM beamline [4]	24
Figure 2-3. The layout of the SXRMB beamline [5].....	25
Figure 2-4. The schematic layout of the TPS beamlines [7].	26
Figure 2-5. The schematic diagram of X-ray Nanoprobe [8]	27
Figure 2-6. The layout of the APS [11]	28
Figure 2-7. The layout of the 20-BM at APS [12].....	29
Figure 2-8. Absorption edges in the plot of absorption of coefficient as a function of wavelength [13]	30
Figure 2-9. The absorption edge of B, N in the plot of the attenuation length as a function of photon energy [14]	31
Figure 2-10. (a). Schematic illustration of X-ray absorption of a free atom via the photoelectric process. (b). X-ray absorption fine structure of a diatomic system via scattering of photo-electron with neighboring atom [18]......	33
Figure 2-11. Schematic illustration of transmission mode of XANES.....	34
Figure 2-12. Attenuation lengths extracted from the SR measured spectra [20].....	35
Figure 2-13. Detection modes for XANES; fluorescence yield (FY) and total electron yield (TEY).....	36
Figure 2-14. (a) electron-hole excitation and electron-hole recombination by (b) direct path, (c) indirect path and (d) defect path.....	37
Figure 2-15. An illustrating diagram of Bragg's diffraction.....	39
Figure 2-16. A schematic diagram of the SEM setup [27].....	40
Figure 3-1. A photo of the undoped ZnO grown on the Si wafer via hydrothermal method.	45

Figure 3-3. Low magnification SEM images of undoped and P-doped ZnO. a) ZnO: p-100-2. b) ZnO: n-100.	48
Figure 3-4. SEM images of undoped and P-doped ZnO. a) ZnO: p-100-2. b) ZnO: p-120-2. c) ZnO: n-100. d) ZnO: n-120.	49
Figure 3-5. the EDX mapping of zinc, oxygen, phosphorus in ZnO: p-100-2 structures and ZnO: p-100-1.5 structures.	52
Figure 3-6. the XRD pattern of ZnO: n-100, ZnO: n-120, ZnO: p-100-2, ZnO: p-120-2, ZnO: p-100-1.5 and ZnO: p-120-1.5 at (1010), (0002) and (1011) diffraction peak.	53
Figure 3-7. XANES spectrum of undoped and P-doped ZnO at Zn K-edge. a) XANES spectrum of ZnO: n-100, ZnO: n-120, ZnO: p-100-2 and ZnO: p-1-120-2 at the Zn K-edge in FY b) Zoom in of FY XANES of ZnO: n-100 and ZnO: p-100-2 at the Zn K-edge in FY	55
Figure 3-8. XANES spectrum of undoped and P-doped ZnO at Zn K-edge. a) XANES spectrum of ZnO: n-100, ZnO: n-120, ZnO: p-100-2 and ZnO: p-1-120-2 at the Zn K-edge in FY b) Zoom in of FY XANES of ZnO: n-100 and ZnO: p-100-2 at the Zn K-edge in FY	56
Figure 3-9. Zoom in of XANES spectrum of ZnO: n-100, ZnO: p-100-2, ZnO: p-, ZnO: p-100-1.5 at Zn $L_{3,2}$ -edge in TEY and PFY.	56
Figure 3-10. XANES spectrum of ZnO: n-100, ZnO: n-120, ZnO: p-100-2, ZnO: p-120-2, ZnO: p-100-1.5 and ZnO: p-120-1.5 at O K-edge in TEY and PFY.	57
Figure 3-11. Zoom in of XANES spectrum of ZnO: n-100, ZnO: p-100-2, ZnO: p-, ZnO: p-100-1.5 at O K-edge in TEY and PFY.	58
Figure 3-12. XANES spectrum of ZnO: p-100-2, ZnO: p-120-2, ZnO: p-100-1.5 and ZnO: p-120-1.5, $NH_4H_2PO_4$, black phosphorus at P K-edge in TEY and PFY.	59
Figure 3-13. XEOL spectra of ZnO: n-100 under the excitation X-ray energy set across the Zn K-edge.	60
Figure 3-14. The intensity ratio (I_{NBE}/I_{DE}) with different X-ray energies at Zn K-edge.	60
Figure 4-1. A photo of the ZnO products grown on Si wafer via CVD technique under UV excitation.	65
Figure 4-2. The schematic diagram for the general experimental set up for the ZnO synthesis by CVD technique in my project.	66
Figure 4-3. XRD pattern of ZnO: n-80-16, ZnO: p-75-16, ZnO: p-80-16, ZnO: p-80-19 and ZnO: p-80-21 at (1010), (0002) and (1011) diffraction peak.	68
Figure 4-4. SEM images for both undoped and P-doped ZnO particles. a) ZnO: n-80-16, b) ZnO: p-80-16, c) ZnO: p-80-19, and d) ZnO: p-80-21.	70
Figure 4-5. SEM images for P-doped ZnO particles under different gas flow rate. a) ZnO: p-80-16, b) ZnO p-75-16.	70
Figure 4-6. EDX mapping of zinc, oxygen, phosphorus in ZnO: p-80-16 structures and ZnO: p-75-16 structures.	74
Figure 4-7. XANES spectra of ZnO: n-80-16, ZnO: p-75-16 and ZnO: p-80-16 at Zn K-edge in FY mode.	75
Figure 4-8. XANES spectrum of ZnO: p-75-16 and ZnO: p-80-16, P_2O_5 and black phosphorus at P K-edge in TEY and FY mode.	77
Figure 4-9. XEOL spectrum of ZnO: n-80-16 under the excitation X-ray energy set across the Zn K-edge measured at room temperature. The insert figure is the XANES spectra of ZnO: n-80-16 at FY mode.	79
Figure 4-10. The ratio between the intensity of NBE and the intensity of DE with the six X-ray energies at 9.64, 9.659, 9.665, 9.6705, 9.6765 and 9.7 keV respectively.	79

Figure 4-11. XEOL spectrum of ZnO: p-80-16 under the excitation X-ray energy set across the Zn K-edge measured at room temperature. The insert figure is the XANES spectra of ZnO: p-80-16 at FY mode. 81

Figure 4-12. The ratio between the intensity of NBE and the intensity of DE with the six X-ray energies at 9.64, 9.659, 9.665, 9.6705, 9.6765 and 9.7 keV respectively. 81

List of Abbreviations

APS	Advanced Photon Source
CB	conduction band
CLS	Canadian Light Source
DCM	Double-crystal monochromator
EDX	Energy-dispersive X-ray spectroscopy
FY	Fluorescence yield
PFY	Partial fluorescence yield
SEM	Scanning electron microscopy
SGM	Spherical Grating Monochromator
SR	Synchrotron radiation
SXRMB	Soft X-ray Microcharacterization Beamline
TEY	Total electron yield
TPS	Taiwan Photon Source
VB	valence band
VLS-PGM	Variable Line Spacing Plane Grating Monochromator
XRD	X-ray diffraction
XAFS	X-ray absorption fine structure
XANES	X-ray absorption near edge structure
XEOL	X-ray excited optical luminescence
XRD	X-ray diffraction
UWO	University of Western Ontario

Chapter 1

1. Introduction

1.1. Zinc Oxide

1.1.1 Background

Over the past decades, semiconductor nanostructures have attracted extensive attraction, because they can transport electrons/holes and function as building blocks for nanoscale electronics and optoelectronics assembled without the need for complex and costly fabrication facilities [1]. Therefore, synthesizing large-scale, high-quality nanoscale p-n junctions in a controlled way is important for industrial applications in nanodevices.

Zinc Oxide (ZnO) is one of the important II-VI semiconductors and remains a popular research topic in today's scientific field due to its optoelectronic properties, such as photocatalytic, and intrinsic n-type semiconducting properties [2]. ZnO is a versatile wide bandgap semiconductor that has been used widely for a range of applications including sensors, lasers and photovoltaic devices [3]. With a wide bandgap of 3.4 eV and a large exciton binding energy of 60 meV¹, ZnO has been recognized as one of the most promising materials in the next-generation optoelectronic devices [4]. However, due to its native defects, such as zinc interstitial and oxygen vacancy [5], ZnO is well known as an intrinsic n-type semiconductor. Therefore, how to synthesize high-quality p-type ZnO semiconductors with doping and investigate their optoelectronic properties and local chemical structures are important and necessary. During my MSc project, my research topic is synthesizing both undoped and P-doped ZnO nano/microstructures and investigating their local electronic structures and optical properties.

1.1.2 Crystal Structure

It is well known that ZnO has two main crystal structures. One is wurtzite (hexagonal, space group P6₃mc) and another is zincblende (cubic, space group F-43m) [2, 6]. ZnO is stable with the hexagonal wurtzite phase at room temperature due to its ionicity that resides exactly at the borderline between the covalent and the ionic material [6, 7]. ZnO is a prototype of a tetragonally coordinated ionic semiconductor. According to the relationship

among Phillip's ionicity, the energy of stacking faults and related material as a function of c/a ratio, the higher the c/a ratio in the crystal, the lower is the stacking fault energy and the smaller ionicity [6]. Therefore, ZnO is stable thermodynamically with the wurtzite phase. For a clear demonstration of both hexagonal wurtzite and cubic zincblende phases, the basic crystal structure of hexagonal wurtzite and cubic zincblende ZnO are represented in Figure 1-1. The Zn and O atoms are denoted as white and blue spheres respectively. In my MSc project, both undoped and P-doped ZnO products are hexagonal wurtzite.

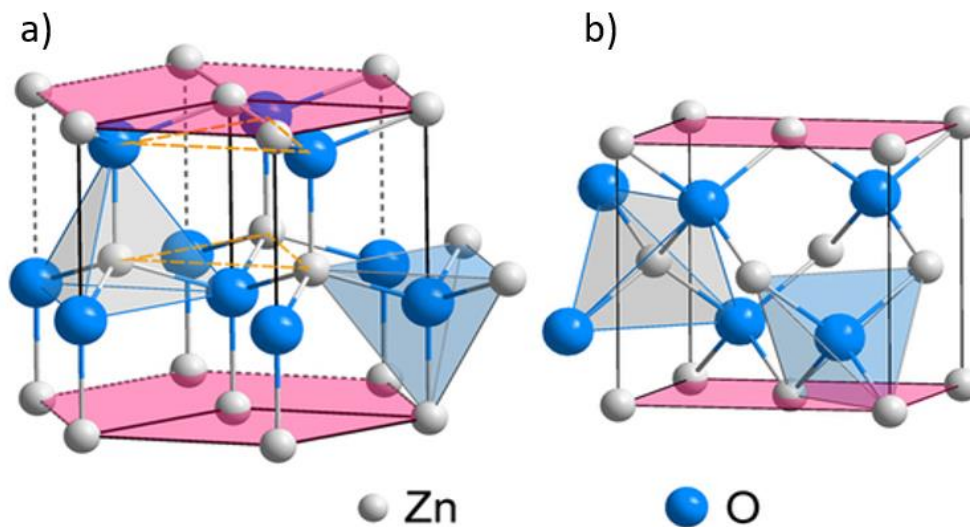


Figure 1-1. Stick-and-ball representation of ZnO crystal structure: hexagonal wurtzite and cubic zincblende. White and blue spheres denote Zn and O respectively [6]

1.1.3 P-type ZnO semiconductor synthesis limitations and solutions

According to the band theory, materials can be divided into insulators, semiconductors and metal depending on the width of the band gap. Figure 1-2 shows the difference among the insulator, semiconductor, and metal by the width of their bandgaps. The width of the bandgap generally refers to the energy difference between the top of the valence band and the bottom of the conduction band. Essentially, the distance of the band gap represents the minimum energy that is required to promote a valence electron bound to an atom to become a conduction electron that is free to move within the crystal lattice and serve as a charge carrier to conduct electric current. If the valence band is full and the conduction is empty,

then electrons cannot move in the solid; however, if some electrons transfer from the valence to the conduction band, then the current can flow. Therefore, the bandgap is an important factor to determine the electrical conductivity of the material. The bandgap is also important since it can help to determine the optical property of the material. The color of absorbed and emitted light both depend on the bandgap of the semiconductor. For example, the bandgap for ZnO semiconductor is around 3.4 eV which corresponds to about 364 nm which is in the UV region, therefore the color of ZnO is white. However, with the UV energy excited, the hole in the valence band and the electron in the conduction band recombined and form the exciton which would cause the luminescence. Therefore, bandgap is a major factor to study the optoelectronic properties of materials especially the wide bandgap semiconductor area.

- Insulator vs semi-conductor vs metal

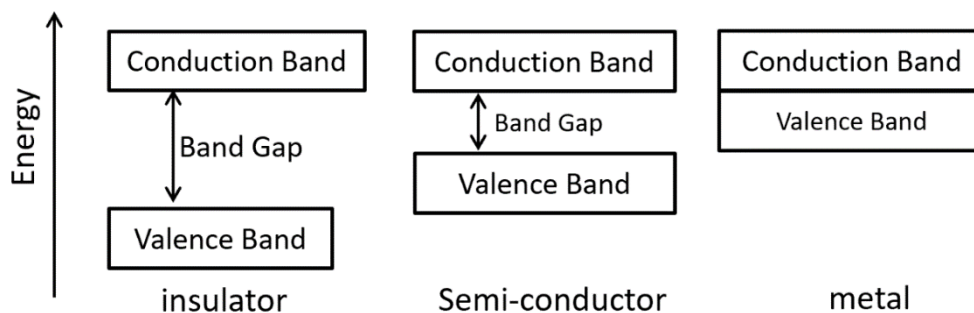


Figure 1-2. The difference among the insulator, semiconductor, and metal

Semiconductors can be divided into 2 groups: n-type semiconductors and p-type semiconductors. “n-type” comes from the negative charge of the electron. In an n-type semiconductor, electrons are the majority carrier, and holes are the minority carrier. “P-type” comes from the positive charge of a hole. In a p-type semiconductor, holes are the majority carrier, and electrons are the minority carrier. The difference between the n-type and p-type semiconductors is the position of the Fermi level. Figure 1-3 shows the different positions of the Fermi level in p-type and n-type semiconductors, respectively. Fermi level is the term used to describe the top of the collection of electron energy levels at absolute zero temperature. Shifting of the Fermi level in an extrinsic semiconductor from the equilibrium Fermi level is the explanation of the probability of finding the maximum dominant carriers of the type. For example, in an n-type semiconductor, the probability of

finding an electron near the conduction band edge is larger than the probability of finding a hole at the valence band edge. Thus, the Fermi level is close to the conduction band in an n-type semiconductor. On the other hand, the Fermi level is close to the valence band in a p-type semiconductor, because the probability of finding a hole at the valence band edge is larger than the probability of finding an electron at the conduction band edge.

- p-type semi-conductor vs n-type semiconductor

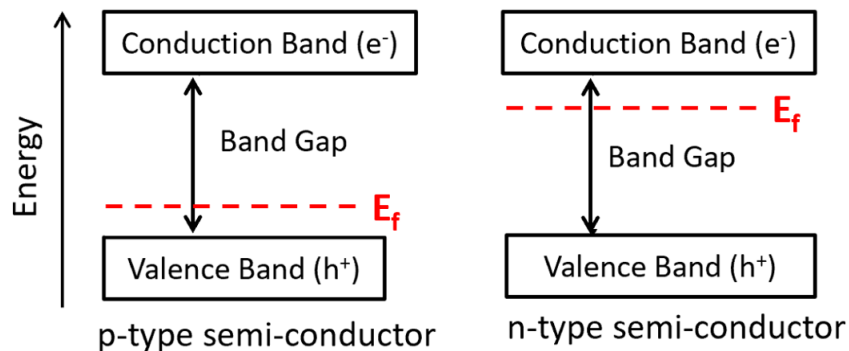


Figure1-3. The different position of the Fermi level in p-type and n-type semiconductor respectively

ZnO is well known as an intrinsic n-type semiconductor due to its native defects such as oxygen vacancy and zinc interstitial [5]. In order to obtain p-type ZnO, it is necessary to provide the compensation of native donor defects by introducing electron acceptors. Even with the dopant, p-type ZnO semiconductor is still hard to synthesize, and this is because of the low solubility of dopants, high concentration of deep level impurities, and native defects compensating the holes [3]. For the synthesis of p-type ZnO, both group I and group V elements have been chosen as the dopant since these two groups of elements can form shallow acceptor levels by substituting either oxygen or zinc. In theory, the group I elements are better dopants than group V elements, because the group I elements are easier to form shallow acceptor levels by substituting zinc [8]. However, the compensation effect by interstitial defects or self-compensation limits the use of group I elements [9]. Group V elements also have attracted much attention as the dopants for the synthesis of p-type ZnO. Nitrogen is one of the most representative group V elements that has been used as the dopants. Since it has a similar atomic radius and valence energy of 2p orbital as that of the oxygen [1], nitrogen would substitute the oxygen in ZnO lattice and form the shallow

acceptor levels. However, the doping effect of nitrogen cannot be sustained due to the out-diffusion of the dopant from ZnO and the electron-hole binding energy is around 400 meV which is too large for appreciable ionization to occur at room temperature [9,10]. Therefore, nitrogen is not a perfect dopant to synthesize p-type ZnO semiconductors. Phosphorus is another representative group V element that has been used as a p-type ZnO semiconductors dopant. By comparing with nitrogen, phosphorus can provide high hole concentrations with low resistivity [9,11] and a deeper electron acceptor level. However, unlike nitrogen, the mechanism of how phosphorus is doped into ZnO semiconductors is still not clear. Many pieces of literatures have been published showing that phosphorus can be doped into ZnO lattice by substituting zinc through either experiments or the first-principle calculation. In the meantime, some literatures have been published show that phosphorus may involve the synthesis of p-type ZnO semiconductors by substitute oxygen through synchrotron experiments [12, 13]. Since ZnO is an intrinsic n-type semiconductor, the p-type conductivity in ZnO plays a key role in the formation of homojunction. Therefore, it is necessary and important to investigate the role of phosphorus in p-type ZnO synthesis. In my MSc. project, I am focusing on synthesizing both undoped and P-doped ZnO nano/microstructures and investigating their local electronic structures and optoelectronic properties.

1.2. Synthesis method of ZnO nanoparticles

1.2.1 Hydrothermal method

The hydrothermal method is one of the most common methods to synthesize nanomaterials in an aqueous phase. It refers to the heterogeneous reaction for synthesizing inorganic material in aqueous media above ambient temperature and pressure [14]. The term “hydrothermal” is of geologic origin. It is first used by the British geologist, Sir Roderick Murchison to describe the action of water at an elevated temperature and pressure in bringing about changes in the earth’s crust leading to the formation of various rocks and minerals [15]. The hydrothermal method was used to help the earth scientists to determine complex geological processes of the formation of rocks, minerals, and ore deposits. Now, the hydrothermal technique has found its place in several branches of science and technology, especially for nanomaterial synthesis. Many literature and reports have already

shown that ZnO nanostructures and heterojunctions can be synthesized on a substrate with a ZnO seeds layer by hydrothermal technique [16, 17]. However, how to synthesis p-type ZnO nanostructures with controlling its doping concentration and ZnO p-n junction remains many unsolved challenges. In my MSc. project, how to synthesize P-doped ZnO nanoparticles by hydrothermal method, investigating the relationship between the dopant concentration and the morphology and studying the local electronic structure are my research purposes.

Hydrothermal synthesis is a unique technique to crystallize substances from high-temperature aqueous solutions under high vapor pressure [18]. It can be defined as a method of synthesis of single crystals that depends on the solubility of minerals in hot water under high pressure [19]. The synthesis is normally performed in an autoclave which is a stainless-steel pressure vessel that contains the nutrient solution. A temperature gradient is maintained between the opposite ends of the growth chamber. Hydrothermal synthesis usually uses water as the solvent, acting as both catalyst and oxide components during the synthesis [20]. There are many advantages for the hydrothermal method, such as low cost and easy experiment set. By comparing with other synthesis techniques, the main advantage of this method over others is its ability to produce crystals which is unstable near the melting point. This method is also suitable for the growth of large good-quality crystals while maintaining control over their composition [21]. Figure 1-4 shows the autoclaves which were used for the experiments described here.

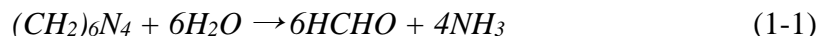


Figure 1-4. Autoclaves have been used during hydrothermal experiments.

Over the past decades, the hydrothermal growth of ZnO attracted extensive attraction since it can occur under mild conditions as well as allowing for controlling the crystal

morphology via changes in the solution conditions or introducing organic molecules during the growth process [22, 23]. Scientists often use Zn^{2+} salts such as zinc nitrate hexahydrate ($Zn(NO_3)_2 \cdot 6H_2O$) or Zinc acetate dihydrate ($Zn(CH_3CO_2)_2 \cdot 2H_2O$) and alkaline reagent such as hexamethylenetetramine ($C_6H_{12}N_4$) as precursors to synthesize ZnO nanoparticles. The general experimental procedure is (1) dissolving both solid precursors with DI water to prepare growth solutions with equal concentration. (2) The substrate is immersed into the growth solution with a polished side down to keep any precipitates suspended in the solution body from falling onto the substrate. (3) The growth solution (with substrate) is transferred into the sealed autoclave and the autoclave would be put into the oven to start the growth process [24]. Figure 1-5 illustrates the general experimental preparation and procedure for the ZnO hydrothermal synthesis. There are several literatures that published the mechanism for hydrothermal growth of crystalline ZnO [24-27]. Generally, the overall chemical reactions of the formation of the ZnO by using the zinc salt/hexamethylenetetramine ($C_6H_{12}N_4$) solution are represented as equation 1-4 [24, 28]:

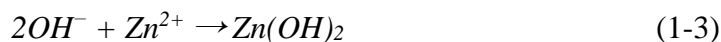
Decomposition Reaction:



Hydroxyl supply reaction:



Supersaturation reaction:



ZnO nanoparticles growth reaction:



ZnO crystals form in both the solution and on the substrate surface via homogeneous and heterogeneous nucleation, respectively. From the above reactions, Zn^{2+} and OH^- are two key components that influence the ZnO crystal growth. When attached to the nonpolar side facets, hexamethylenetetramine can facilitate the anisotropic growth in the [0001] direction [24]. Hexamethylenetetramine also acts as a weak base and a pH buffer. As shown in

equation 1 and equation 2, hexamethylenetetramine hydrolyzes in water and gradually produces HCHO and NH_3 , releasing the strain energy that is associated with its molecular structure, Then all hydroxide ions reacted with Zn^{2+} while the pH value of the solution remains constant, and $\text{Zn}(\text{OH})_2$ dehydrates into ZnO at the end which is represented as equation 3 and equation 4 [24, 28]. During the growth of ZnO nanoparticles, controlling the supersaturation of the reactants is important. Some articles have published that the high supersaturation levels favor nucleation and low supersaturation levels favor crystal growth [28, 29]. If OH^- is produced rapidly, the Zn^{2+} ions in the solution will precipitate out quickly which would affect the growth of ZnO crystal and the morphology of ZnO nanoparticles. since Zn^{2+} would contribute little to the ZnO nanowire growth and eventually result in the fast consumption of the nutrient and prohibit further growth of the ZnO nanowires [28]. Therefore, controlling the concentration of OH^- to remain at the low supersaturation level is the key parameter during the synthesis of ZnO nanoparticles.

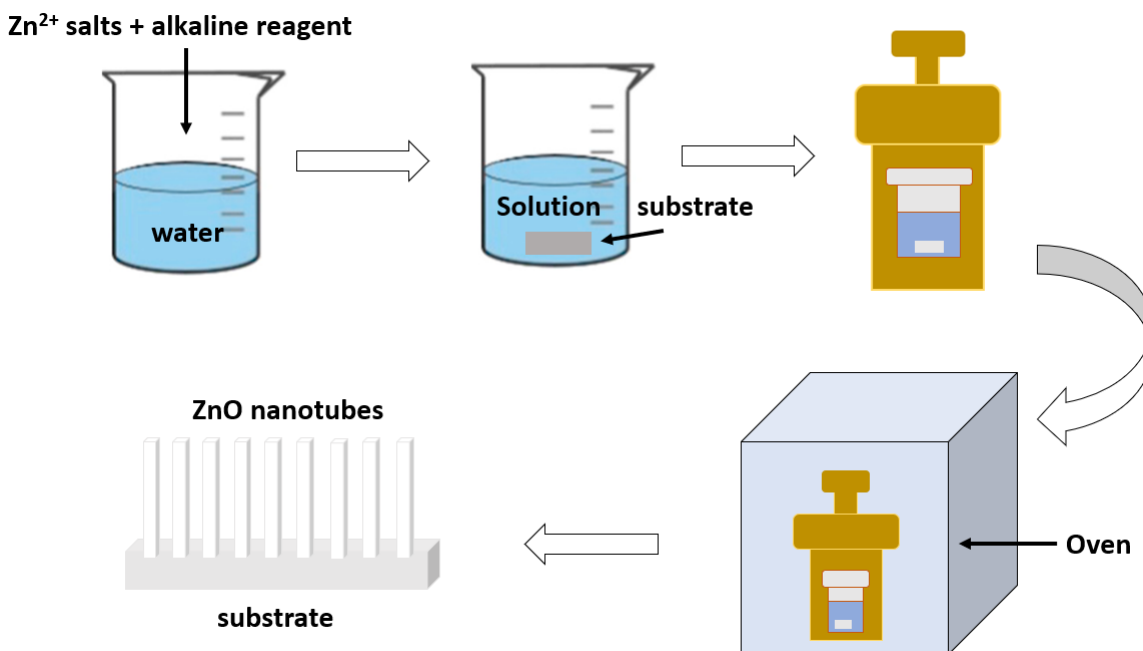


Figure 1-5. Schematic illustration of the general experimental preparation and procedure for the ZnO hydrothermal synthesis

1.2.2 Chemical Vapor Deposition (CVD) method via Vapor-Liquid-Solid (VLS) mechanism

Chemical Vapor Deposition (CVD) is a very common deposition method used to produce high-quality and high-performance material under vacuum [30]. It is the technique in which substances that are in the vapor phase are condensed to generate solid phase material [31]. CVD is the process involving chemical reactions by using one or more gaseous compounds or elemental substances to produce nonvolatile solid thin films on substrates [30, 32]. It is a crucial material preparation method that plays an essential role in precious metal thin films and had widely introduced in industrial applications [30]. By comparing with other synthesis methods, CVD has the highest level of control for the fabrication of 2D nanomaterials [33]. This technique can produce 2D nanomaterials with high crystal quality purity and limited defects on the substrate. The 2D nanomaterial prepared by the CVD technique is used in a variety of practical applications such as electronics, optoelectronics, and solar cell devices [33]. The main advantages provided by the CVD technique are adaptability of large-scale processing and controlling reaction environment [34]. Since there are many experiment parameters that need to be care during the process, “controlling reaction environment” also becomes the biggest disadvantage for CVD method at the same time. I used the VLS technique in this work. During the VLS process, there are many experiment parameters that need to consider such as gas flow rate and reaction temperature. There are several works of literatures published different gas flow rates and different reaction temperature periods that would have a huge influence on the morphology of nanomaterials which would affect their optical and structural properties [35-37]. Therefore, during these processes, all parameters must be accurately and reproducibly optimized to produce good films. Without strictly experimental conditions, there are also some other weaknesses and disadvantages for the VLS technique. For example, the VLS process needs high reaction temperatures since the chemical reaction needs to be done in the vapor phase which may be unsuitable for structures already fabricated on substrates. In the meantime, many precursors for VLS such as metalorganics are relatively expensive, therefore by comparing with other synthesis techniques such as the hydrothermal method, the cost of experimental set-up for VLS is relatively higher. Even though, high flexibility and high

growth rates make the VLS method attract extensive attraction on nanoparticles preparation. Figure 1-6 illustrates the general experimental set-up for the VLS synthesis.

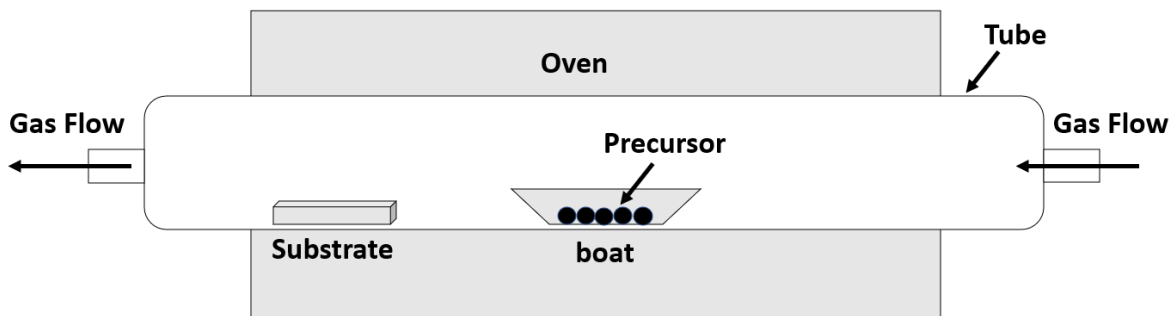


Figure 1-6. Schematic illustration of the general experimental set up for the CVD technique via VLS mechanism

The vapor-liquid-solid (VLS) mechanism is a mechanism for the growth of 1D structures starting in a gas phase, which feeds the precursor to dissolved in a liquid catalyst until saturation followed by nucleation and growth. Generally, the VLS mechanism is typically described in three stages: (1) preparation of a liquid alloy droplet upon the substrate from which nanoparticles are to be grown. (2) Introduction of the substance to be grown as a vapor, which adsorbs onto the liquid surface, and diffuses into the droplet. (3) Supersaturation and nucleation at the liquid/solid interface leading to crystal growth [38]. Regularly, the growth of a crystal from direct adsorption of a gas phase onto a solid surface is generally low. The VLS mechanism improves this by introducing a catalytic liquid phase that can rapidly adsorb a vapor to supersaturation levels, and from which crystal growth can subsequently occur from nucleated seeds at the liquid-solid interface. Therefore, scientists often introduce the VLS mechanism during the CVD synthesis to decrease the growth period and try to control the morphology of nanoproducts by changing the experiment parameters. The synthesis procedure and mechanism of ZnO synthesis by CVD technique via VLS mechanism has already been discussed in some literatures [39, 40]. Figure 1-7 illustrates the general growth mechanism for the ZnO via VLS mechanism. According to the diagram, the amount of precursor, the thickness of the metal catalyst and the gas flow rate are important parameters during the synthesis via VLS mechanism. Many research papers and journals have reported both n-type and p-type ZnO nanostructures can be synthesized on a substrate with catalyst by CVD technique via VLS mechanism [37, 40,

41]. However, since the VLS technique is highly dependent on reaction environments (substrate position, gas flow rate, temperature, etc.), how to synthesis high-quality ZnO nanoparticles with controlling morphologies is remaining a challenge. In my MSc. project, how to synthesize P-doped ZnO nanoparticles by VLS technique with controlling morphology and the study the local electronic structure are the research objectives.

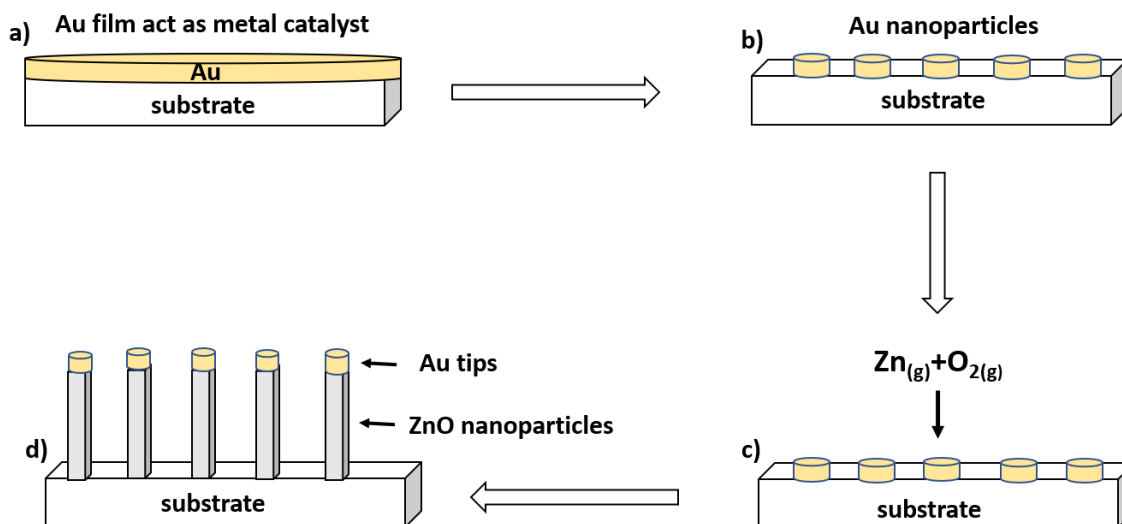


Figure 1-7. Schematic illustration of the general growth mechanism for the ZnO via VLS mechanism

1.3. Introduction to synchrotron radiation technique

Synchrotron radiation (SR) is powerful electromagnetic radiation that has a wide continuous range between infrared to gamma rays produced by a bright light source called synchrotron. In a synchrotron, electrons are accelerated to a speed that closes to the speed of light and circulate in the storage ring. SR is emitted in the tangential direction of the orbit when the relativistic electrons are bent under the external magnetic field [42].

SR was first observed in the General Electric Research Laboratory in Schenectady, New York, on April 24, 1947 [43], and it has been recognized as a powerful tool since 1960s [44]. The synchrotron technique was widely used to probe the structure and electronic information of various materials. With the development of instruments, more SR facilities have been developed and built around the world. In 1980s, the second-generation SR facilities came into researchers' sight such as BESSY I in Germany and Aladdin in the US.

After that, the third-generation SR has been developed because more insertion devices had been introduced such as undulators and wigglers which can generate more bright light. In my project, synchrotron experiments were carried out in three third-generation SR facilities: Canadian Light Source (CLS) in Saskatoon, Taiwan Photon Source (TPS) in Hsinchu and Advanced Photon Source (APS) near Chicago.

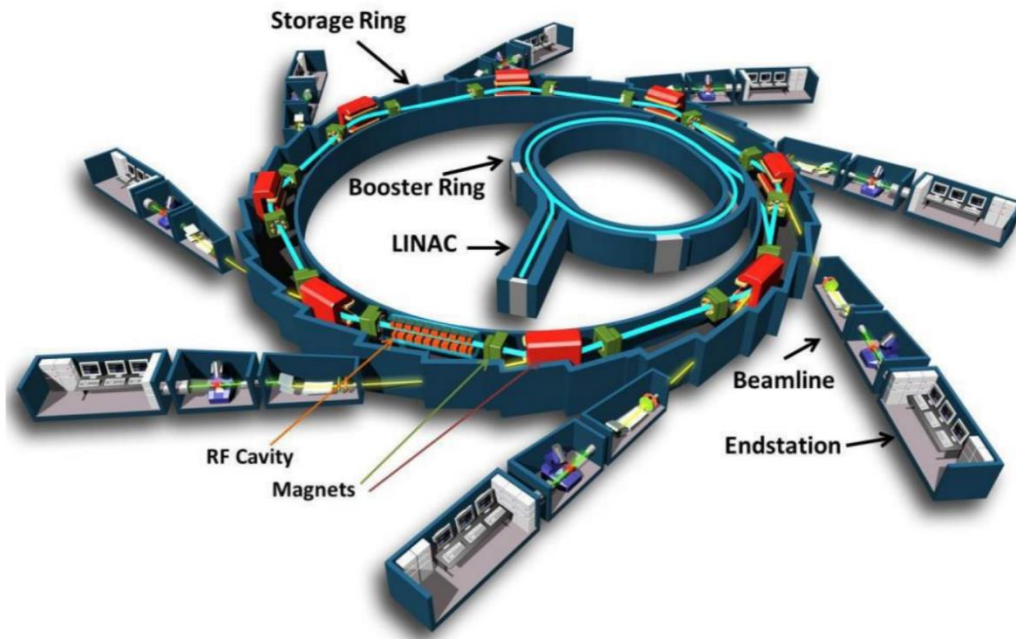


Figure 1-8. The schematic diagram of the CLS SR facility [45].

Figure 1-8 illustrates the schematic diagram of an SR facility like CLS. The function of SR is demonstrated in this diagram. First, the electron is ejected by using a direct high voltage to heat a cathode to a high temperature. Then, these emitted electrons are transferred to the linear accelerator (LINAC) and accelerated to a speed that closes to the speed of light and the energy unit is MeV. Next, these accelerated electrons are moved into the booster ring to obtain further acceleration until the energy of electrons reaches in GeV. After that, electrons are stored in the storage ring and circulate in the orbit at almost the speed of light. There are several magnets (red and green components in the diagram) located in the storage ring to control the direction of electrons during the same time. There is also a radio frequency (RF) cavity in the straight sanction of the storage ring which is used to replenish the energy loss during the synchrotron radiation process. It achieved boost electrons and

remain at the same travel speed by applying a time-varying electric field. As illustrated, the SR process occurs since the trajectory of the electron is changed by different magnets. The bending magnets are dipole magnets, which are in the curved section of the storage ring. Undulators and wigglers are arrays of magnets with alternating polarity, which are placed in the straight section of the storage ring. Different types of magnets contribute to different kinds of radiation. They can be determined by the opening angle ($1/\gamma$) and γ can be expressed by the equation 1-5:

$$\gamma = \frac{E}{M_0 c^2} \quad (1-5)$$

Where γ is the ratio of the mass of a relativistic electron, M_0 is the rest mass of the electron, c is the speed of the light, and E is the energy. Figure 1-9 illustrates the configurations of the bending magnet, wiggler and undulator. As illustrated, there is a sharp cone sweep produced in the bending plane under the bending magnet. The difference between the undulator and the wiggler is the opening angle. The wiggler leads to a large opening angle and the undulator is the opposite. There is a short period in wigglers and large bend structures that can result in a continuum of radiation. For the undulator, the longer period and small bend structure are desirable for experiments to need a collimated beam with higher brightness^{46,47}.

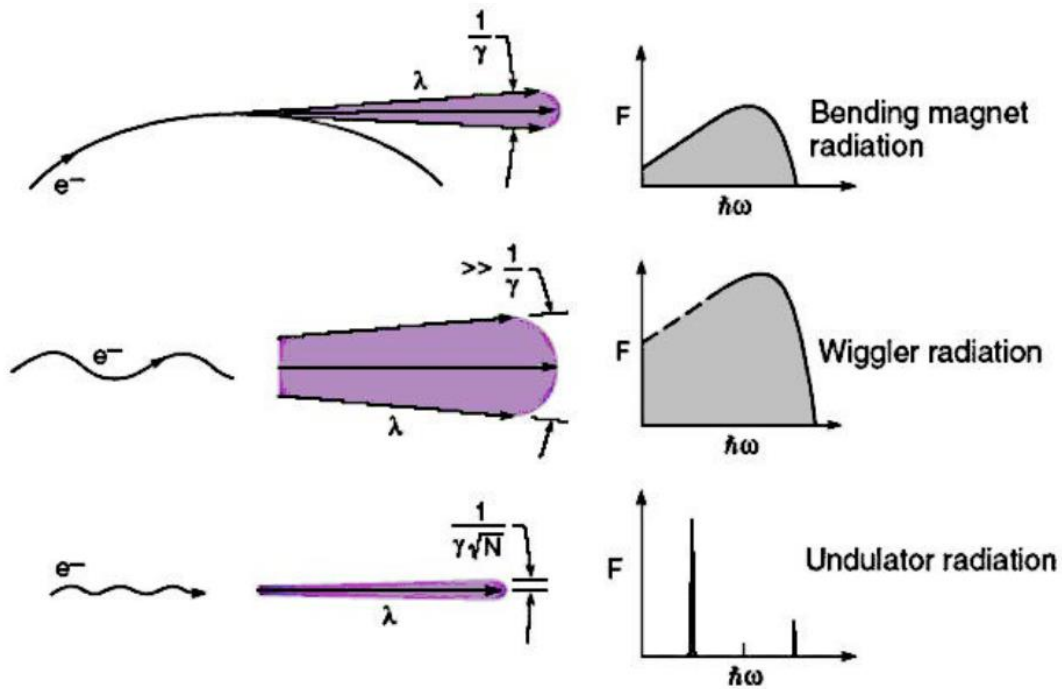


Figure 1-9. The schematic illustration of the spatial distribution of the photons emitted from the bending magnet, wiggler and undulator (left panel) and the energy distribution in a flux vs energy plot (right panel) [46, 47].

Since SR can be applied in a wide energy range (between IR and hard x-ray); the choice of the monochromator is important because it needs to be satisfied for various measurement requirements. Generally, to extract the desired wavelength range for a particular type of experiment, a grating monochromator is selected for soft X-rays and a double-crystal monochromator is employed for hard X-rays. Figure 1-9 is a schematic diagram of the soft X-ray selected by the grating monochromator. In the diagram, the incident photon (polychromatic) hits the grating monochromator at a grazing angle, it can diffract at different angles. To keep the beam at a fixed angle, the energy can be either rotatable or movable. The grating diffraction calculation can be expressed by the equation 1-6:

$$n\lambda = d(\sin\alpha \pm \sin\beta) \quad (1-6)$$

Where α is the angles of incidence, β is the angle of diffraction, n represents the order of the diffraction, λ represents the wavelength of the diffraction light and, and d is the distance between the grating lines.

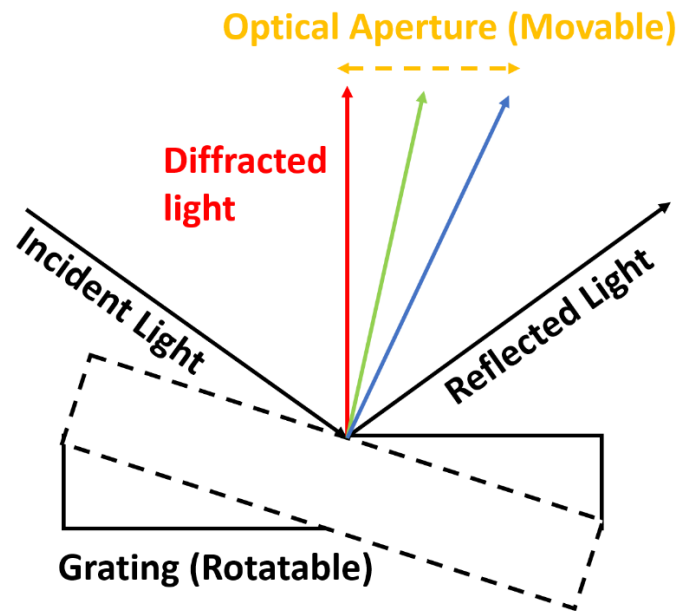


Figure 1-9. Schematic diagram of a grating monochromator with rotated positions

To operate hard X-ray experiments at beamlines, a double-crystal monochromator is usually selected. Two crystals are set parallel with each other in the monochromator and both crystals have the same physical parameters with the same element and same d spacing value. An X-ray beam with a fixed angle can be achieved by rotation and translation between two paralleled crystals. As shown in Figure 1-10, the first crystal is installed that can be rotated to have different incident beam angles (θ). Meanwhile, the second crystal can direct the Bragg diffracted beam to the fixed exit point (Figure 1-10 (b)) by rotation and translation. Thus, the mono-energy X-ray with constructive interference can be followed by Bragg's law:

$$n\lambda = 2d \sin \theta \quad (1-6)$$

where n is the order of diffraction, λ is the wavelength of the diffracted light, d is the lattice spacing of the crystal and, and θ is the Bragg angle. Depending on the required energy range for different measurements, the type of crystal with different d -spacing values can

be chosen. The inter-planar distance can be determined by Miller indices (h, k, l) and lattice constant a. For example, in cubic crystals, the relationship between them is expressed by the Equation 1-7:

$$d_{hkl} = \frac{a}{\sqrt{h^2+k^2+l^2}} \quad (1-7)$$

If we use Si as an example, after the calculation, Si (333) has a smaller d value than Si (111), therefore Si (333) has a better resolution as the crystal in monochromator than Si (111). The difference between grating and crystal monochromator is the distance between the line; in soft X-ray gratings, it can vary from 600 to 1800 lines per millimeter or microns separation between lines. Smaller gratings cannot be fabricated for hard X-rays which have wavelengths on the order of 0.1 nm or Å. Consequently, crystals with lattice spacing on the order of Å must be used.

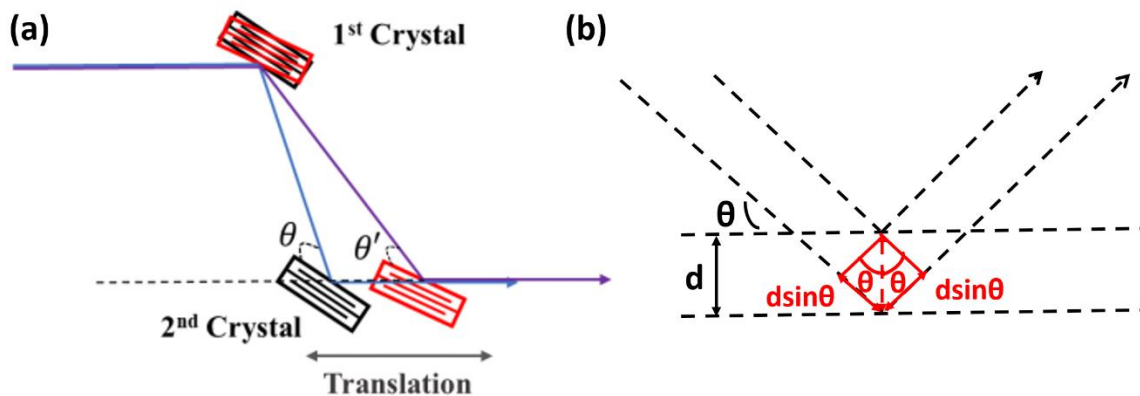


Figure 1-10. (a) Schematic illustration of a double-crystal monochromator, (b) illustration of Bragg diffraction

In summary, SR has several advantages by comparing with other traditional X-ray measurements. First, the SR can provide various energy ranges from IR to hard X-ray by using monochromators. Second, there are 12 orders of magnitude higher brightness of flux of SR than that of the traditional X-ray source. Moreover, the high spatial resolution spectra can be achieved by a highly collimated beam of SR. In the meantime, the SR can produce the photon that is linearly polarized in the orbit plane or elliptically polarized out of the orbit plane. Finally, pulsed wave with a few nanoseconds between pulses is due to bunched

electrons generated by the RF cavity, which provides an opportunity to conduct time-resolved spectroscopy experiments.

1.4. Objective and arrangement of thesis

In my MSc. project, my research objective is to synthesize both n-type and p-type ZnO nanoparticles. Since ZnO is an intrinsic n-type semiconductor, my experiments are focusing on how to synthesize p-type ZnO semiconductor by using phosphorus as the dopant. I used two synthesis methods, one is the hydrothermal method, and another is the VLS technique. I also applied SR as my main characterization method to analyse the chemical structure and optical properties of both undoped and P-doped ZnO nano/microparticles.

There are four chapters in this thesis. Chapter 1 gives the general introduction and background of semiconductors, ZnO nanostructures, synthesis method (hydrothermal method and VLS technique), an overview of synchrotron radiation, and the objective of this thesis. Chapter 2 describes detailed information on synchrotron-based characterizations including XANES, XEOL and XES. Chapter 2 also describes the information of laboratory characterization such as XRD, SEM and EDX. Chapter 3 and chapter 4 present my research results of both undoped and P-doped ZnO nano/microparticles by hydrothermal synthesis and VLS technique. In these chapters, both synchrotron-based characterization results and laboratory characterization results are included. Chapter 5 includes the conclusion of this thesis and proposed future work. Curriculum Vitae is presented at the end.

1.5. Reference

1. Ü. Özgür, Y.I. Alivov, C. Liu, A. Teke, M.A. Reshchikov, S. Doğan, et al. A comprehensive review of ZnO material and devices. *J. Appl Phys.* **2005**, 98, 041301
2. T. Lim, P.S. Mirabedini, K. Jung, P.A. Greaney, A.A. Martinez-Morales. High-index crystal plane of ZnO nonpyramidal structures: Stabilization, growth, and improved photocatalytic performance. *Appl. Surf. Sci.* **2021**, 536, 147326
3. Z.L. Wang, J.H. Song. Piezoelectric Nanogenerators Based on Zinc Oxide Nanowire Arrays. *Science.* **2006**, 312, 242

4. J.H. Lim, C.K. Kang, K.K. Kim, I.K. Park, D.K. Hwang, S.J. Park. UV Electroluminescence Emission from ZnO Light-Emitting Diodes Grown by High-Temperature Radiofrequency Sputtering. *Adv. Mater.* **2006**, *18*, 2720.
5. P. Li, S.H. Deng, J. Huang. First-principles studies on the dominant acceptor and the activation mechanism of phosphorus-doped ZnO. *Appl. Phys. Lett.* **2011**, *99*, 111902
6. A. Ashrafi, C. Jagadish. Review of Zincblende ZnO: Stability of metastable ZnO phases. *J Appl Phys.* **2007**, *120*, 071101
7. R.J. Guerrero-Moreno, N. Takeuchi. *Phys. Rev. B.* **2002**, *66*, 205205
8. C.H. Park, S.B. Zhang, S.-H. Wei. Origin of p-type doping difficulty in ZnO: The impurity perspective. *Phys. Rev. B* **2002**, *66*, 073202
9. S.H. Hwang, K.J. Moon, T.I. Lee, W. Lee, J.M. Myoung. Controlling phosphorus doping concentration in ZnO nanorods by low temperature hydrothermal method. *Mater. Chem. Phys.* **2014**, *143*, 600
10. G.H. Sonawane, S.H. Sonawane. Nanocomposites and Its Applications. In *Applications of Nanomaterials*; Bhagyaraj. S.M, Oluwafemi. O.S, Kalarikkal. N, Thomas. S, Ed.; Woodhead Publishing: Cambridge, 2018, p.1-22
11. Y. Heo, S. Park, K. Ip, S. Pearton, D. Norton. Transport properties of phosphorus-doped ZnO thin films. *Appl. Phys. Lett.* **2003**, *83*, 1128
12. Vaithianathan V, Moon. J.H, Chang. C.H, Asokan. K, Kim SS. Electronic Structure of P-Doped ZnO Films with p-Type Conductivity. *J. Nanosci. Nanotechnol.* **2006**, *6*, 3422
13. V. Vaithianathan, K. Asokan, J.Y. Park, S.S. Kim. Local electronic structure of phosphorus-doped ZnO films investigated by X-ray absorption near-edge spectroscopy. *Appl. Phys. A.* **2009**, *94*, 995
14. G. Huang, C.H. Lu, H.H. Yang. Magnetic Nanomaterials for Magnetic Bioanalysis. In *Novel Nanomaterials for Biomedical, Environmental and Energy Applications*; X. Wang, X. Chen, Ed.; Elsevier: Amsterdam, 2019, p.89-109.
15. K. Byrappa, M. Yoshimura. Hydrothermal Technology—Principles and Applications. In *Handbook of Hydrothermal Technology*. Norwich, New York: Noyes Publications, 2013, p.1-49

16. A. Polini, F. Yang. Physicochemical characterization of nanofiber composites. In *Nanofiber Composites for Biomedical Applications*. M. Ramalingam, S. Ramakrishna, Ed.; Woodhead Publishing: Cambridge, 2017, p.97-115
17. S.H. Hwang, K.J. Moon, T.I. Lee, W. Lee, J.M. Myoung. Controlling phosphorus doping concentration in ZnO nanorods by low temperature hydrothermal method. *Mater. Chem. Phys.* **2014**, *143*, 600
18. A. Kuamr, D. Nanda. Methods and fabrication techniques of superhydrophobic surfaces. In *Superhydrophobic Polymer Coatings*; S.K. Samal, S. Mohaty, S.J. Nayak, Ed.; Elsevier: Amsterdam, 2019, p.43-75
19. B.P. Kafle. Introduction to nanomaterials and application of UV–Visible spectroscopy for their characterization. In *Chemical Analysis and Material Characterization by Spectrophotometry*; B.P. Kafle, Ed.; Elsevier: Amsterdam, 2020, p.147-198,
20. A.D. Li, W.C. Liu. Optical properties of ferroelectric nanocrystal/polymer composites. In *Physical Properties and Applications of Polymer Nanocomposites*; S.C. Tjong, Y.W. Mai, Ed.; Woodhead Publishing: Cambridge, 2010, p. 108-158
21. G.H. Sonawane, S.H. Sonawane. Nanocomposites and Its Applications. In *Applications of Nanomaterials*; Bhagyaraj. S.M, Oluwafemi. O.S, Kalarikkal. N, Thomas. S, Ed.; Woodhead Publishing: Cambridge, 2018, p.1-22
22. L. Vayssieres. Growth of arrayed nanorods and nanowires of ZnO from aqueous solutions. *Adv. Mater.* **2003**, *15*, 464
23. D. Andeen, J.H. Kim, F.F. Lange, G.K.L. Goh, S. Tripathy. Lateral epitaxial overgrowth of ZnO in water at 90. Degree. *Adv. Funct. Mater.* **2006**, *16*, 799
24. L. Zhang, X. Liu, C. Geng, H. Fang, Z. Lian, X. Wang, D. Shen, Q. Yan. Hexagonal Crown-Capped Zinc Oxide Micro Rods: Hydrothermal Growth and Formation Mechanism. *Inorg. Chem.* **2013**, *52*, 10167
25. J. Cho, Q. Lin, S. Yang. et al. Sulfur-doped zinc oxide (ZnO) Nanostars: Synthesis and simulation of growth mechanism. *Nano Res.* **2012**, *5*, 20
26. H. Wang, J. Xie, K. Yan, M. Duan. Growth Mechanism of Different Morphologies of ZnO Crystals Prepared by Hydrothermal Method. *J. Mater. Sci. Technol.* **2011**, *27*, 153

27. N.J. Nicholas, J.V. Franks, W.A. Ducker. The mechanism for hydrothermal growth of zinc oxide. *CrystEngComm*. **2012**, *14*, 1232
28. Y. Zhang, M.K. Ram, E.K. Stefanakos, D.Y. Goswami. Synthesis, Characterization, and Applications of ZnO Nanowires. *J. Nanomater.* **2012**, *2012*, 1
29. B. Weintraub, Z. Zhou, Y. Li, Y. Deng. Solution synthesis of one-dimensional ZnO nanomaterials and their applications. *Nanoscale*. **2010**, *2*, 1573
30. A. Behera, P. Mallick, S.S. Mohapatra. Nanocoatings for anticorrosion: An introduction. In *Corrosion Protection at the Nanoscale*; S. Rajendran, T.A. Nguyen, S. Kakooei, M. Yeganeh, Y. Li, Ed.; Elsevier: Amsterdam, 2020, p.227-243
31. M.B. Tahir, M. Rafique, M.S. Rafique, T. Nawaz, M. Rizwan, M. Tanveer. Photocatalytic nanomaterials for degradation of organic pollutants and heavy metals. In *Micro and Nano Technologies, Nanotechnology and Photocatalysis for Environmental Applications*. M.B. Tahir, M. Rafique, M.S. Rafique, Ed.; Elsevier: Amsterdam, 2020, p.119-138
32. L. Xia. Importance of nanostructured surfaces. In *Bioceramics, From Macro to Nanoscale*. Osaka, A., Narayan. R., Ed.; Elsevier: Amsterdam, 2021, pp. 5-24.
33. Y.B. Pottathara, Y. Grohens, V. Kokol, N. Kalarikkal, S. Thomas. Synthesis and Processing of Emerging Two-Dimensional Nanomaterials. In *Nanomaterials Synthesis, Design, Fabrication and Applications*. Y.B. Pottathara, V. Kokol, N. Kalarikkal, Ed.; Elsevier: Amsterdam, 2019, p.1-25
34. P. Unnikrishnan, D. Srinivas. Heterogeneous Catalysis. In *Industrial Catalytic Processes for Fine and Specialty Chemicals*. S.S. Joshi, V.V. Ranade, Ed.; Elsevier: Amsterdam, 2016, p.41-111
35. O. Lobacheva, P.L. Corcoran, M.W. Murphy, J.Y.P. Ko, T.K. Shan. Cathodoluminescence, X-ray excited optical luminescence, and X-ray absorption near-edge structure studies of ZnO nanostructures. *Can. J. Chem.* **2012**, *90*, 298
36. S. Kumar, P.D. Sahare, S. Kumar. Optimization of the CVD parameters for ZnO nanorods growth: Its photoluminescence and field emission properties. *Mater. Res. Bull.* **2018**, *105*, 237

37. Y. Nie, Z. Wang, J. Wang, F. Bao, J. Zhang, Y. Ma, T.K. Sham, X. Sun. Synthesis and Structure-Dependent Optical Properties of ZnO Nanocomb and ZnO Nanoflag. *J. Phys. Chem. C.* **2017**, *121*, 26076
38. A.S. Mukasyan. Vapor-Liquid-Solid Mechanism of Structure Formation. In *Concise Encyclopedia of Self-Propagating High-Temperature Synthesis*; I.P. Borovinskaya, A.A. Gromov, E.A. Levashov, Y.M. Maksimov, A.S. Mukasyan, A.S. Rogachev, Ed.; Elsevier: Amsterdam, 2017, p.418-420
39. R. Müller, F. Huber, O. Gelme, M. Madel, J.P. Scholz, A. Minkow, U. Herr, K. Thonke. Chemical Vapor Deposition Growth of Zinc Oxide on Sapphire with Methane: Initial Crystal Formation Process. *Cryst. Growth Des.* **2019**, *19*, 4964
40. T. Lim, P.S. Mirabedinib, K. Jung, P.A. Greaney, A.A. Martinez-Morales. High-index crystal plane of ZnO nanopyramidal structures: Stabilization, growth, and improved photocatalytic performance. *Appl. Surf. Sci.* **2021**, *536*, 147326
41. S. Swathi. R. Yuvakkumar. G. Ravi, E.S. Babu, D. Velauthapillai, S,A, Alharbi. Morphological exploration of chemical vapor–deposited P-doped ZnO nanorods for efficient photoelectrochemical water splitting. *Ceram. Int.* **2021**, *47*, 6521
42. H. Yamashita. XAFS Analysis and Applications to Carbons and Catalysts. In *Carbon Alloys*. E.C. Yasuda, M. Inagaki, K. Kaneko, M. Endo, A. Oya, Y. Tanabe, Ed.; Elsevier Science: Amsterdam, 2003, pp.289-209.
43. A.L. Robinson. History of synchrotron radiation. *Synchrotron Radiat. News.* **2015**, *28*, 4
44. E.E. Koch, D.E. Eastman, Y. Farge. Synchrotron radiation-a powerful tool in science. *Synchrotron Radiat. News.* **1983**, *1*, 1
45. M.A. Gros, C. Knoechel, M. Uchida, D. Parkinson, G. McDermott, C. Larabell. Visualizing Sub-Cellular Organization Using Soft X-ray Tomography. In *Comprehensive Biophysics*. Egelman, E.H., Ed.; Academic Press: Cambridge, 2012, p. 90-110.
46. D. Attwood, A. Sakdinawat. A. Synchrotron Radiation. In *X-Rays and Extreme Ultraviolet Radiation: Principles and Applications*. D. Attwood, A. Sakdinawat, Ed.; Cambridge: Cambridge University Press. 2017, p.148-226.

47. B. Crasemann. Review/Synthèse Synchrotron radiation in atomic physics. *Can. J. Phys.* **1998**, 76, 251

Chapter 2

2. Synchrotron Radiation Facilities and Characterization Techniques

2.1. Synchrotron radiation facilities and beamlines

2.1.1. Canadian Light Source (CLS)

The Canadian Light Source (CLS) is a third-generation synchrotron light source located in Saskatoon, Saskatchewan, Canada. It consists of an electron storage ring with an energy of 2.9 GeV and a linear accelerator that injects electron to the ring. The circumference of the ring is 170.88 meters with a maximum current of 220 mA, and horizontal emittances of 18 nm-rad [1]. Figure 2-1 shows the schematic layout of the CLS experiment hall which include most beamlines in the CLS. There are 15 operating beamlines and 3 commissioning beamlines that can provide photon energy range from Far IR to hard X-ray [2].

MAP OF EXPERIMENTAL HALL

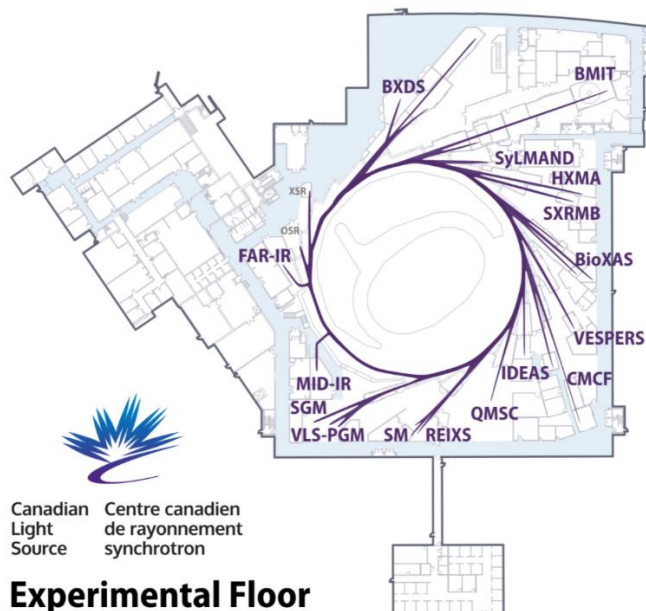


Figure 2-1. The schematic layout of the CLS experiment hall [2]

2.1.1.1. High Resolution Spherical Grating Monochromator (SGM) at CLS

The high-resolution spherical grating monochromator (SGM) beamline (11ID-1) is one of the operating beamlines at CLS. It can provide the bright, tunable and highly monochromatic photon beam within energy between 250 and 2000 eV [3], which is desirable for studying the K-edges of low-Z elements and the L-edges of transition metals. The beamline is ideal for solid sample or gas phase spectroscopy but can be fitted with a variety of end stations [3]. Figure 2-2 shows the layout of the SGM beamline. There are three gratings that can be chosen for the desire energy range, such as low energy grating with 250-700 eV, medium energy grating with 450-1250 eV, and high energy grating with 740-2000 eV. The resolution $E/\Delta E$ is greater than 5000 at energies below 1500 eV with the spot size of $1000 \mu\text{m} \times 100 \mu\text{m}$. The beamline flux at 100 mA is $>10^{12}$ at 250 eV and $>10^{11}$ at 1900 eV [4]. In figure 2-2, there are two end station areas. Area one is designed for photoemission studies, and area two is used for X-ray absorption measurement. In my project, all XANES experiments at O K-edge and Zn $L_{3,2}$ -edge are carried out in area two.

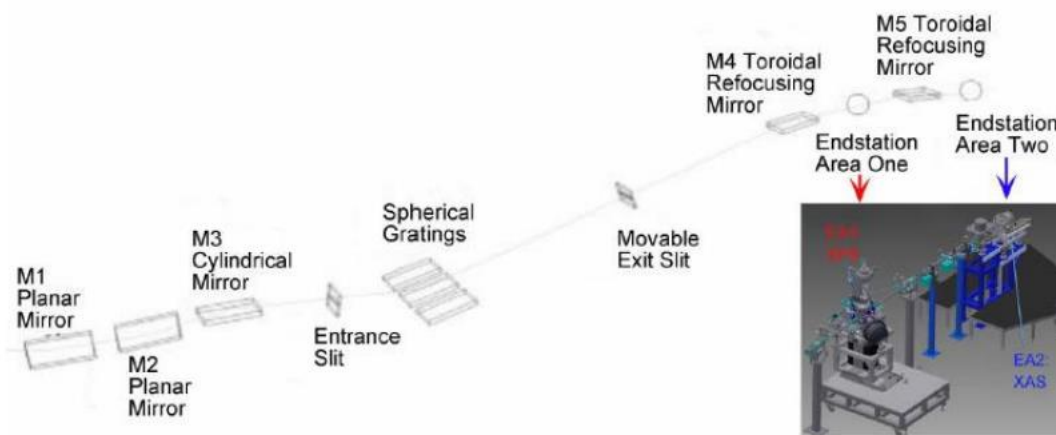


Figure 2-2. The layout of the SGM beamline [4]

2.1.1.2. Soft X-ray Microcharacterization Beamline (SXRMB) at CLS

The soft X-ray microcharacterization beamline (06B1-1) is another operating beamline at CLS. It is medium energy with an electron range between 1.7 and 10keV. This energy range can support research from the biological, environmental, and chemical sciences. Both X-ray photoelectron spectroscopy (XPS) and XAS are available in this beamline. The elemental mapping via microprobe is also available at SXRMB. There are four end stations in this beamline (solid-state end station, microprobe end station, ambient table and high energy XPS). Each end station can provide a unique configuration for a variety of experiments. For example, bulk analysis of the solid sample can be performed in the solid-state end station, mapping experiments can be performed in the microprobe end station, liquid and solid in-situ experiment can be performed in the ambient table, and high energy XPS can provide both surface and bulky information of the material by performing at different depths on the same sample [5]. In my project, all XANES experiments at P K-edge are carried out at this beamline. Figure 2-3 is the layout of the SXRMB beamline.

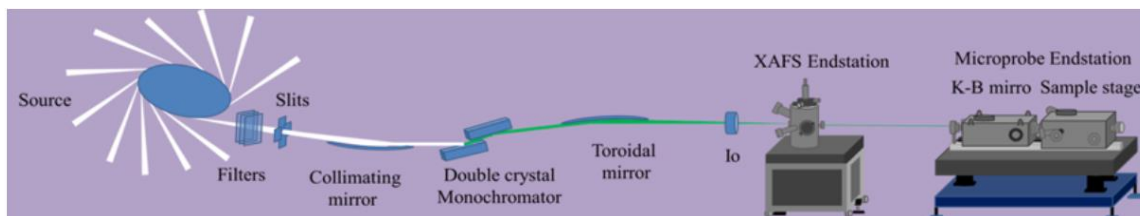


Figure 2-3. The layout of the SXRMB beamline [5]

2.1.2. Taiwan Photon Source (TPS)

Taiwan Photon Source (TPS) is one of the brightest synchrotron light sources in Hsinchu, Taiwan, China. It began its operation in September 2016. The accelerator equips with a low-emittance synchrotron storage ring and booster synchrotron producing a beam of energy 3 GeV with a circumference of 518.4 meters and it comprises 24 double-bend achromats (DBA) cells, with six straight sections of 12 meters and eighteen straight sections of 7 meters in length. The maximum ring current is 500 mA in a top-up injection mode by using two sets of KEKB type superconducting RF cavities [6]. Figure 2-4 shows the schematic layout of the TPS beamlines. In phase I, there are 7 insertion-device (ID)

beamlines. In phase II, there are 7 IDs and 3 bending magnets (BM). In phase III, there will be another 4 IDs and 5 BMS. Up to now, there are 16 beamlines can be operated (05A,07A, 09A, 13A, 15A,19A, 21A, 23A, 24A, 25A, 27A, 31A, 39A, 41A, 44A, and 45A).

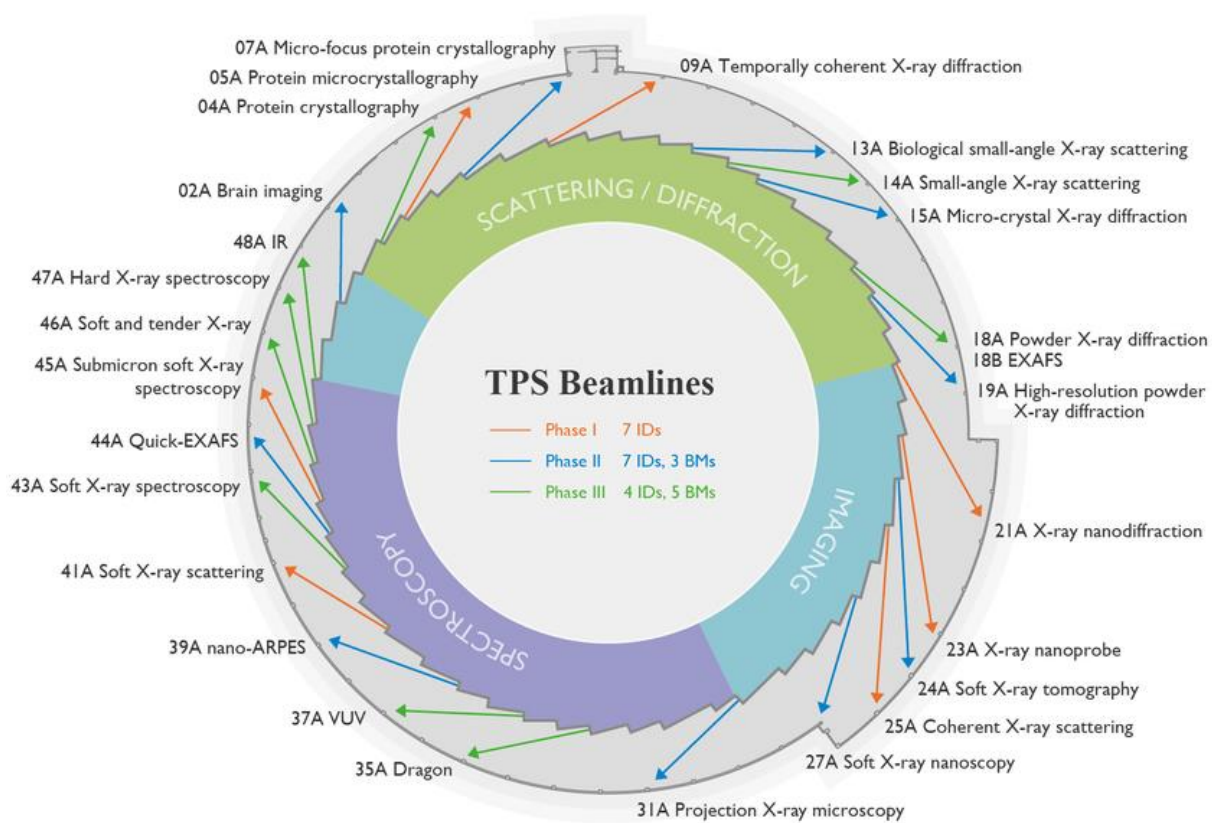


Figure 2-4. The schematic layout of the TPS beamlines [7].

2.1.2.1. 23A X-ray Nanoprobe

The X-ray Nanoprobe (XNP) beamline and associated facility at the Taiwan Photon Source (TPS) provide multimodal X-ray probes for resolving the atomic, chemical and electronic structures of modern advanced materials, with 40 nm spatial resolution in 3D tomographic and non-destructive manners [8]. Figure 2-5 shows the schematic diagram of the X-ray Nanoprobe. The photon energy range is between 4 and 15keV and the excited X-ray energy was tuned and selected by using a double Si (111) crystal monochromators with a typical resolution ($\Delta E/E$) of $\sim 2 \times 10^{-4}$. This beamline can measure the X-ray excited optical luminescence (XEOL), Time Resolved X-ray Excited Optical Luminescence (TR-XEOL),

(XRF), X-ray absorption spectroscopy (XAS), X-ray powder diffraction (XRD), etc. with high spatial and temporal resolution so that in a single probe one can simultaneously obtain the optical, compositional and structural information. The SEM was equipped in a high vacuum chamber (1×10^{-6} torr) with a load-lock system to quickly transfer the samples between the main chamber and the preparation chamber. The information at the precise location and morphology of the nano/microstructure can be obtained easily and quickly through this SEM system. The sample compartment is designed to equip with a cryostat system that maintains the temperature range of 10 K~300 K for the XEOL and TR-XEOL measurements. The ion chamber system provides not only quick X-ray energy calibration using standard element foils but also contrast image mapping to measure the X-ray beam size [9]. In this project, all XANES and XEOL results at Zn K-edge results in chapter 4 are carried out in this beamline.

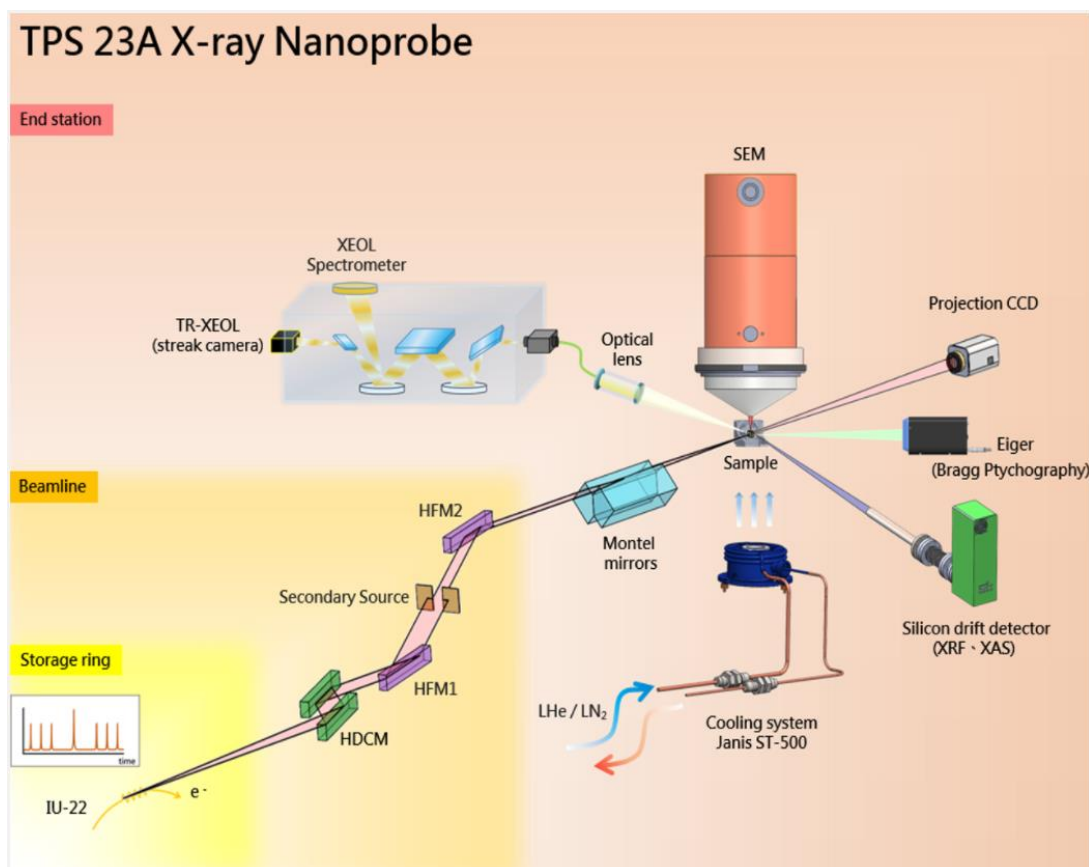


Figure 2-5. The schematic diagram of X-ray Nanoprobe [8]

2.1.3. The Advanced Photon Source (APS)

The Advanced Photon Source (APS) is one of the most technologically complex machines at Argonne National Laboratory in Lemont, Illinois, USA. Figure 2-6 shows the layout of the APS. The storage ring has a circumference of 1104 m, operates at 7 GeV, and is run in a “top-up” mode with injections every two minutes to maintain a constant ring current of 102 mA. The RF cavity has a radio frequency of 351.927 MHz and the ring has an electron beam emittance of $2.514 \text{ nm} \cdot \text{rad}$ [10].

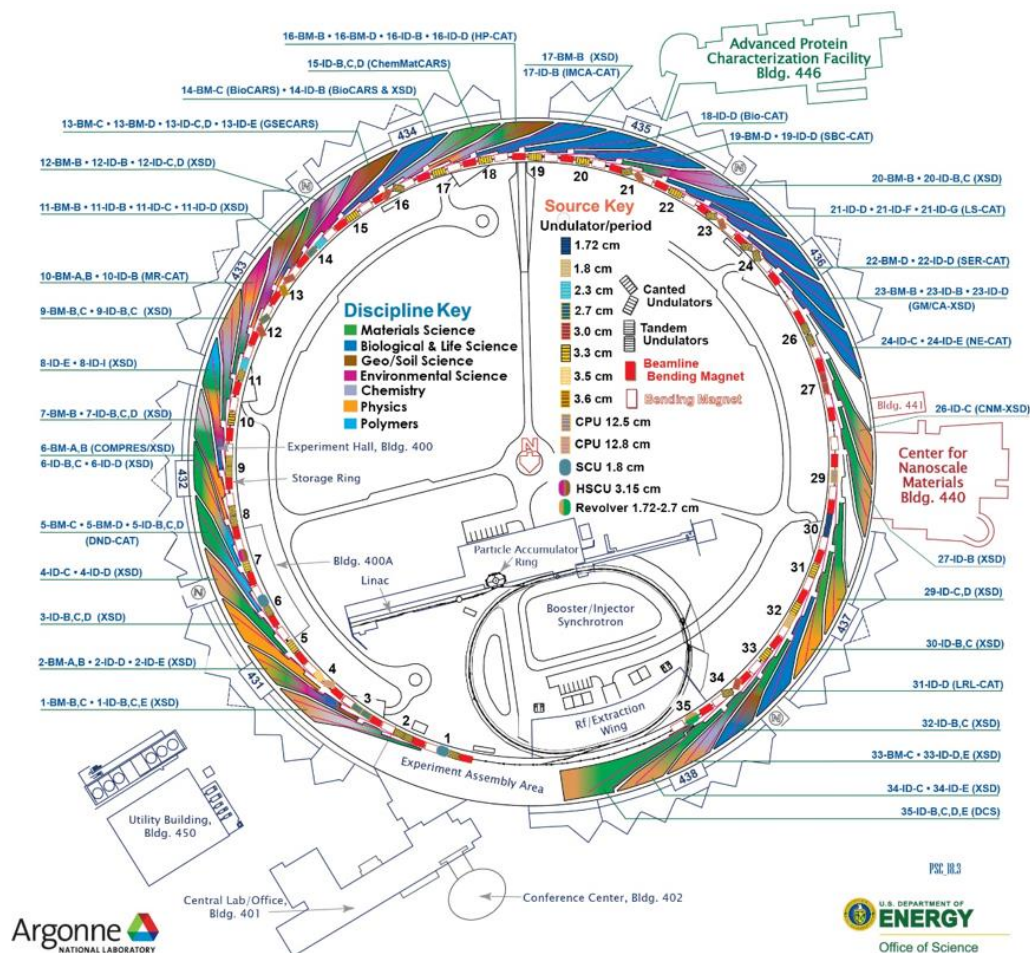


Figure 2-6. The layout of the APS [11]

2.1.3.1. Spectroscopy: Beamline 20-BM

20-BM is a double crystal monochromator (DCM) beamline. Figure 2-7 shows the layout of the 20-BM at APS. Photons are supplied to 20-BM from a bending magnet and then

passed into a Si (111) DCM which provides hard X-rays in the energy range of 2.7–32.7 keV¹². The function of DCM is introduced in chapter 1. The energy resolution of 20-BM is 1.4×10^{-4} ($\Delta E/E$) with a flux of 1×10^{11} photons/s/0.1%BW and a spot size of 30 mm x 1 mm (H x V) [12]. In my project, all XANES and XEOL results at Zn K-edge results in chapter 3 are carried out in this beamline.

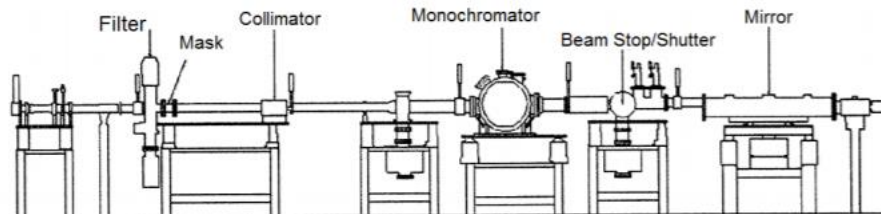


Figure 2-7. The layout of the 20-BM at APS [12]

2.2. Synchrotron Based Technique

2.2.1. The X-ray absorption fine structures (XAFS)

The X-ray absorption fine structure (XAFS) spectroscopy is a premier technique for measuring both electronic and atomic local structures around different atomic species in materials. The X-ray absorption occurs when the X-ray interacts with matter. The relationship between the intensity of the transmitted X-ray (I_t) and the incident X-ray (I_0) follows the Beer-Lambert Law (equation 2-1) where t is the thickness of samples and μ is the absorption coefficient.

$$\frac{I_t}{I_0} = e^{-\mu t} \quad (2-1)$$

The μ can also be expressed as equation 2-2, where ρ is the density of the sample, Z is the atomic number of the element, A is the atomic mass, and E is the X-ray energy. Since the absorption coefficient μ is highly dependent on Z and E ; therefore, X-ray absorption spectroscopy is an element-specific technique.

$$\mu = \frac{\rho Z^4}{AE^3} \quad (2-2)$$

When the energy of the incident photon (E) is equal to or higher than the binding energy of a core electron, there will be an increase in X-ray energy absorption by increasing the absorption cross-section. The absorption cross-section is the probability of absorption of a photon and producing an electron transition from the initial to the final state. When the core electron is excited, it will transit to the unoccupied bond state, quasi-bound state and the continuum if the incident energy is high enough. The energy at which there is a sharp rise (discontinuity) in the (linear) absorption coefficient (μ) of X-rays by an element, which occurs when the energy of the photon corresponds to the energy of a shell of electrons in the atom is also as known as the absorption edge. Figure 2-8 shows several absorption edges in the plot of absorption coefficient as a function of wavelength. In the figure, there are five absorption edges (K, $L_{1,2,3}$, and M) which corresponding to the excitation of various core electrons. These labels (K, $L_{1,2,3}$, and M) edge depends on the shell of the exciting core electrons. For example, K-edge represents the excitation of an electron from 1s orbital. $L_{1,2,3}$ -edge represents the excitation of an electron from 2s, $2p_{1/2}$, $2p_{2/3}$ orbital, respectively. M-edge edge represents the excitation of an electron from 3d orbital. Figure 2-9 shows the absorption edge of B, N in the plot of the attenuation length as a function of photon energy. Although absorption edges for these elements are all at K-edge, the energy for different elements is unique. Therefore, XAFS is a strong characterization method to identify elements.

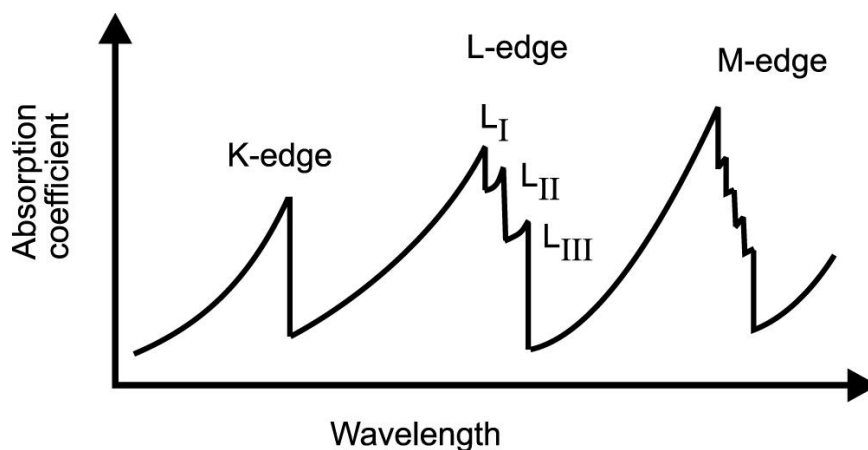


Figure 2-8. Absorption edges in the plot of absorption of coefficient as a function of wavelength [13]

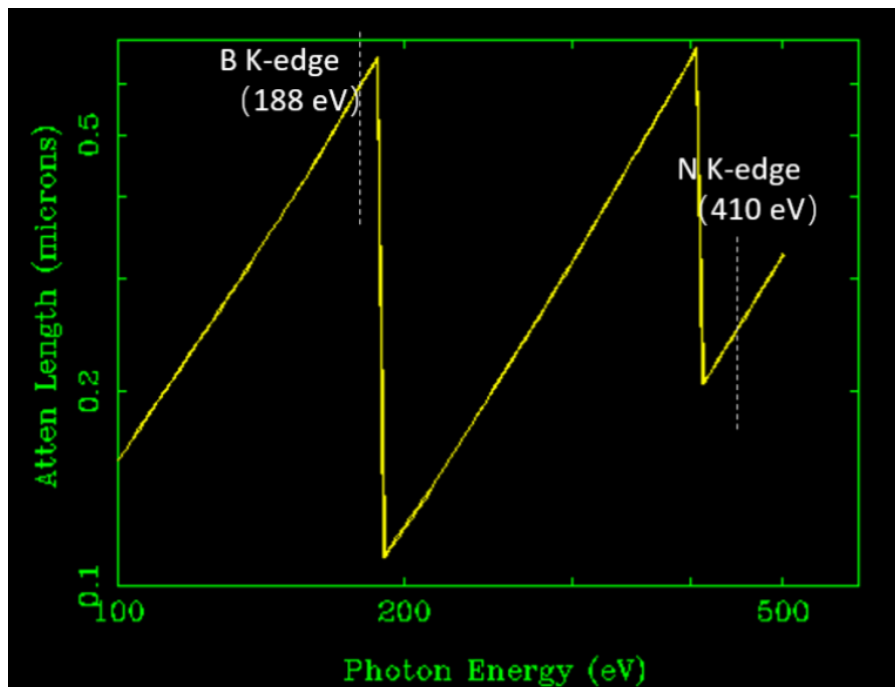


Figure 2-9. The absorption edge of B, N in the plot of the attenuation length as a function of photon energy [14]

The XAFS show up once the outgoing electrons interfere with itself having been backscattered by the neighbouring atoms in the chemical environment via single or multiple scattering. Usually, XAFS can be divided into two parts: X-ray absorption near-edge structure (XANES) and Extended X-ray absorption fine structure (EXAFS). XANES is the energy range between 20 eV below and 50 eV above the edge. EXAFS is the energy range between 50 eV to 1000 eV above the edge. This happens because of the different kinetic energy of electrons associated with different scattering behaviours. Generally, slow photoelectron (low KE) is scattered several times (XANES) by neighboring atoms before leaving the system, and fast photoelectron (high KE) tends to be scattered once (EXAFS) by neighboring atoms before leaving the system. XANES comes from electronic transitions into bound and quasi-bound states as well as multiple scattering interferences from neighbouring atoms. Therefore, XANES can provide information on the oxidation state, coordination and local symmetry of the element of interest [15]. EXAFS can also track the local structure of materials by providing information of bond length within first and second atomic shells and coordination number [16, 17]. In my project, the study of both undoped and P-doped ZnO nano/microparticles are focus on XANES spectra.

Figure 2-10 shows the schematic illustration of XAFS of a free atom and that within a chemical environment. In a free atom system (Figure 2-7 (a)), the photoelectron can be created when a core-level electron absorbs an incident photon with energy higher than the core-level binding energy. The wavenumber of the photon-electron can be considered as that inversely proportional to $\sqrt{E - E_0}$ (E is the energy of incident X-ray and E_0 is the binding energy of the core-level electron). The absorption coefficient (μ) decreases above the edge, and there is no chemical modulation of μ due to scattering with neighbours, and no XAFS [18]. In a diatomic system, the story is different (Figure 2-7(b)). When the energy of the incident X-ray is equal to or higher than the absorption edge, the photon-electron can fill the unoccupied bound states and quasi-bound states. The outgoing photo-electron from the absorbing atom can scatter from the neighbouring atom and the backscattered wave can return to the absorbing atom. There are possible constructive and destructive interferences between the outgoing waves and backscattered waves. It leads to modulations of absorption coefficient μ and this is the origin of XAFS.

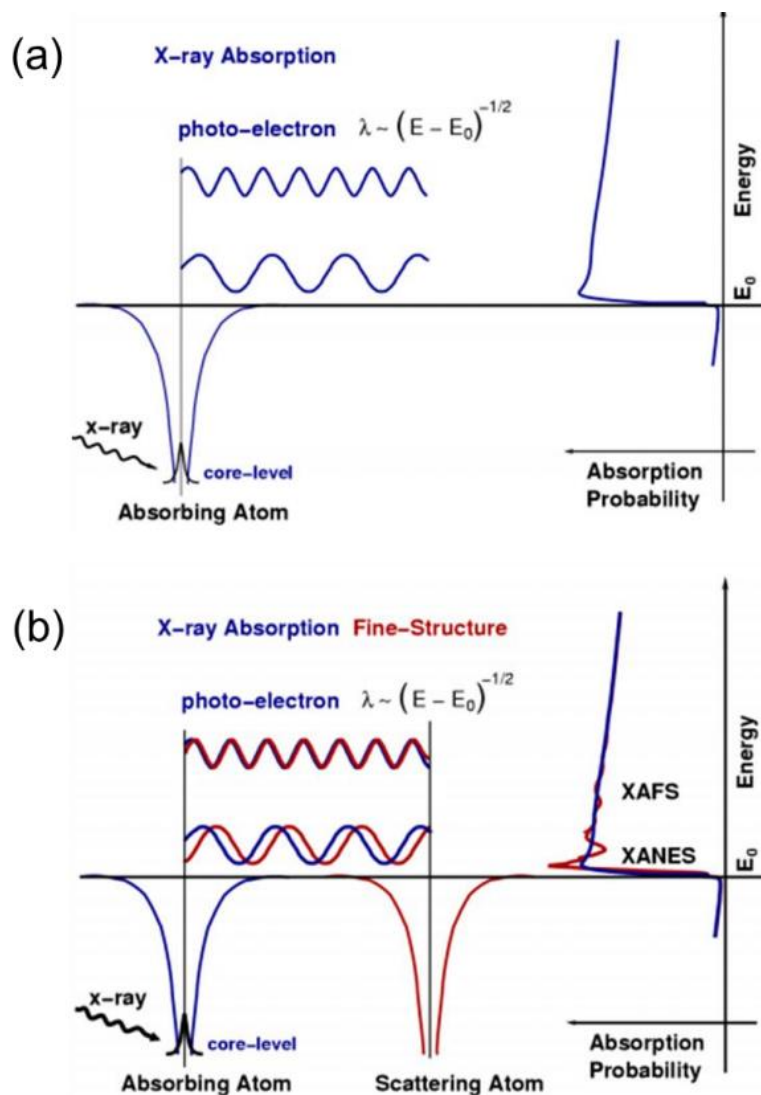


Figure 2-10. (a). Schematic illustration of X-ray absorption of a free atom via the photoelectric process. (b). X-ray absorption fine structure of a diatomic system via scattering of photoelectron with neighboring atom [18].

2.2.2. Detection Mode

In XANES experiments, there are three types of detection modes: transmission, total electron yield (TEY), and fluorescence yield (FY). Generally, transmission mode the most direct mode and the absorption coefficient μ can be determined by the equation 2-3.

$$\mu t = \ln\left(\frac{l_0}{l_t}\right) \quad (2-3)$$

where the transmitted X-ray (I_t) and the incident X-ray (I_0) can be measured during the experiment. However, the quality of the data in transmission mode is depending on the thickness of samples which is a shortage for this mode. The thickness should be around $\mu t = 1$, which would lead to 36.8% transmission. For example, when samples are too thick, it would lead to almost total absorption. When samples are too thin, then there would be no transmission since there is no reliable absorption coefficient. Generally, the transmission mode is desired for hard X-rays with thin samples. Figure 2-11 shows the transmission mode of XANES, where I_0 and I_t are tracked by gas ionization chambers

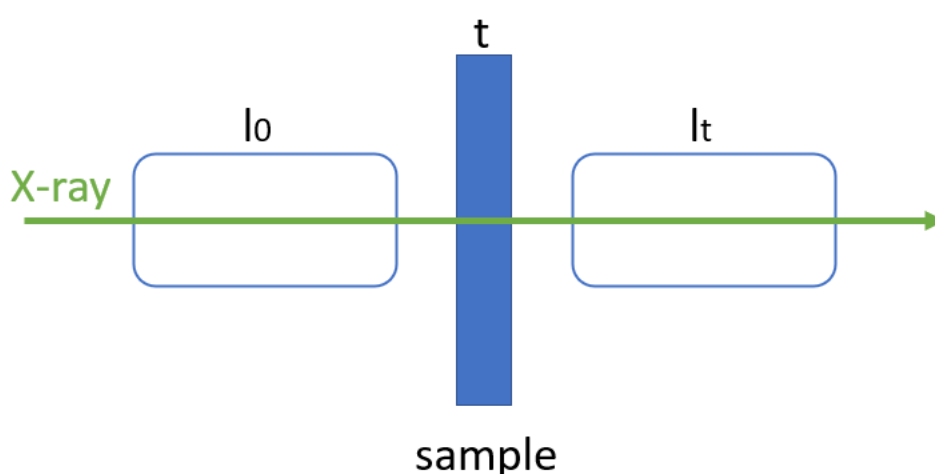


Figure 2-11. Schematic illustration of transmission mode of XANES

Both TEY and FY are also two popular mode in XANES experiments, and they are suitable for soft X-ray measurement since transmission mode here requires ultra-thin samples and these yields are assumed as proportional to the absorption coefficient μ . When the electron is excited and then the core-hole is left behind, the electron at a shallower level can occupy the core-hole and another electron can be ejected via the secondary or Auger process [19]. The TEY mode can detect these electrons ejected from the sample in the XANES experiments. The TEY mode is surface sensitive, therefore it can only detect within a few nanometers into the sample. The electron escape depth can be determined by its kinetic energy via the universal curve (Figure 2-12). TEY mode is the most popular mode in the soft X-ray XANES measurement because the short attenuation length can avoid the thickness effect.

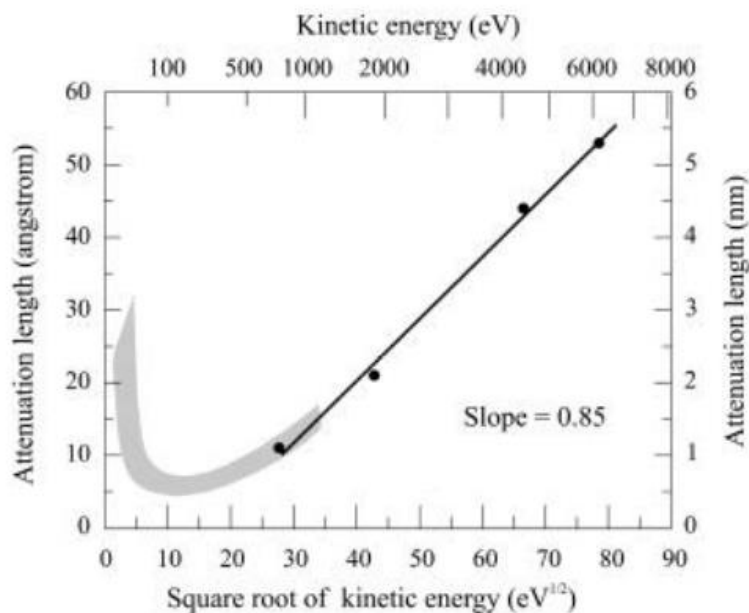


Figure 2-12. Attenuation lengths extracted from the SR measured spectra [20]

FY is another detection mode that has been introduced widely in the XANES experiments. When the electrons from the shallower levels fill the core-hole, there are X-ray fluorescence emitted. In FY mode, the number of emitted fluorescence photons are counted, and the number of these emitted photons is proportional to the number of the absorbed X-ray photons. By comparing with TEY mode, FY mode is bulky sensitive. Figure 2-13 shows both TEY and FY modes. In my project, both FLY and TEY are applied in my XANES experiments.

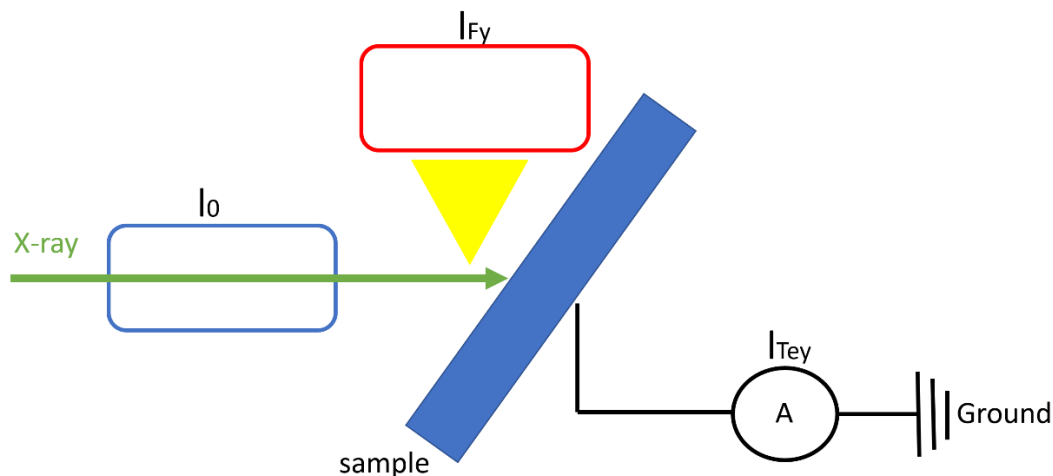


Figure 2-13. Detection modes for XANES; fluorescence yield (FY) and total electron yield (TEY)

2.2.3. X-ray Excited Optical Luminescence (XEOL)

X-ray excited optical luminescence (XEOL) is an X-ray-photon in, optical-photon out process. The first observation of XEOL coincided with the discovery of X-rays by Rontgen in 1895 [21]. As the de-excitation occurs following the X-ray absorption and the core-hole is filled, the hole at outer shells would leave and the additional energy would excite the electron at the shallower levels. This kind of excitation would take place in a cascade process and produce electron-hole pairs until no additional energy can support the further electrons excitations. For example, in a semiconductor, the thermalization would be achieved when the hole transfers to the top of the valence band (VB) and the electron would migrate to the bottom conduction band (CB). After that, the electron and the hole will recombine and release energy. During the electron hole radiative recombination process, XEOL can be generated through optical photoemission. In Figure 2-14, there are three possible paths of this recombination. The first possible path is direct recombination. After the thermalization, the electron in CB and the hole in VB can recombine directly via emitting light with energy close to the band gap (Figure 2-14 (b)). This recombination normally takes place via the formation of the exciton. The exciton has the binding energy just below the conduction band. This binding energy (60 meV for ZnO with a band gap of 3.4 eV) is much smaller than the band gap and is often called optical emission. The second

possible path is the indirect recombination (Figure 2-14 (c)). Both direct and indirect recombination produce luminescence with photon energy close to the bandgap and a short lifetime. The last possible path is the defect path (Figure 2-14 (d)). It can be achieved by producing optical photons from defect states between the bandgap. Since this path is generally due to defects and impurities, it can produce luminescence with photon energy lower than the bandgap and a relatively long lifetime.

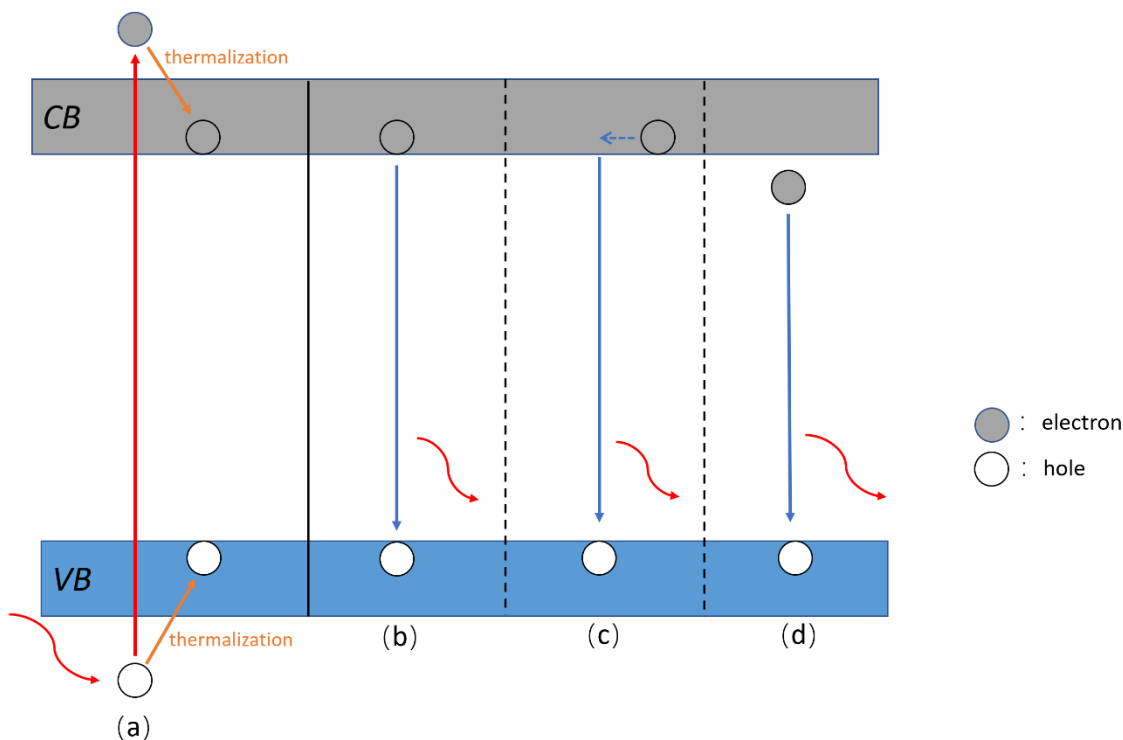


Figure 2-14. (a) electron-hole excitation and electron-hole recombination by (b) direct path, (c) indirect path and (d) defect path.

XEOL is a powerful element specific technique because certain energy can be used to excite core electrons and detect the corresponding deexcitation channels selectively [21]. Combining with XANES, XEOL can be both element-specific and site-specific. These advantages are coupled effectively to the luminescence channel when the incident photon energy is scanned across an absorption edge of an element, probing the responsible sites for X-ray energy transfer to optical emission [22-24]. In my project, XEOL experiments have been done in TPS and XEOL results will be discussed in chapter 4.

2.3. Other Characterization Methods

2.3.1 X-ray Diffraction (XRD)

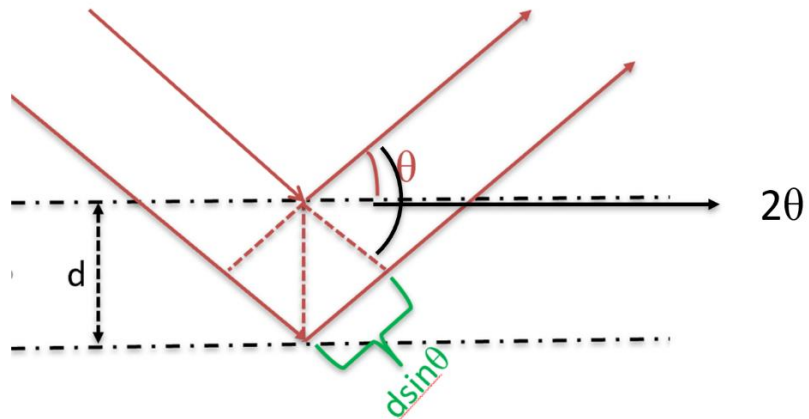
X-ray diffraction (XRD) is a nondestructive technique for characterizing crystalline materials and providing detailed information about crystal structure and physical properties [25]. It can help us to determine the orientation of a single crystal and the shape of crystalline regions. This technique can be used to study the crystalline structure of materials because the X-ray wavelengths are similar to the interatomic spacing of crystalline solids [26]. The diffraction of X-rays by a crystal is described by the Bragg law that relates the wavelength of the X-rays to the interatomic spacing, and is given by equation 2-4:

$$n\lambda = 2d\sin\theta \quad (2-4)$$

Where λ stands for the wavelength of the incident X-ray (e.g., 0.179nm for Co $K\alpha$), d stands for the lattice spacing, and θ stands for the angle of diffraction, and n is the positive integer, the order of diffraction. The peak position in an XRD pattern is associated with the interplanar distance of the corresponding lattice plane, d in the crystal. Figure 2-15 shows the geometry of Bragg diffraction. XRD can also provide information regarding crystallite size. The average crystallite size can be calculated by the peak broadening of the diffraction peaks using the Scherrer equation (equation 2-5):

$$t = \frac{K\lambda}{\beta\cos\theta} \quad (2-5)$$

Where t is the crystallite size, λ is the wavelength of the incident X-ray beam, β is the full width at half of the maximum intensity of the reflection peak, and K is the Scherrer constant [26]. However, the Scherrer equation does not consider internal particle strain and defects, which can also lead to peak broadening, and therefore, the particle size measured by XRD should not be considered as an absolute measure of the crystallite size but rather as the lower limit [26].



d = interplanar distance

λ = the wavelength of the incident wave

n = positive integer

θ = the glancing angle

Figure 2-15. An illustrating diagram of Bragg's diffraction

2.3.2. Scanning Electron Microscopy (SEM) and Energy Dispersive X-ray (EDX)

The scanning electron microscopy (SEM) image is one of the most convenient tools to give information of the microstructure of coated surface and the morphology of particles. Figure 2-16 shows a schematic diagram of the SEM setup. Firstly, an electron beam is shot from an electron gun and directed toward the specimen. The electron beam is formed by accelerated electrons which pass through the condenser lens and objective lens with a few nanometer diameters. When the beam hits the surface of the specimen, the interaction between the beam and specimen occurs to produce the electron signals. While the electron beam scans the surface of the species, the electron signals are detected by the detector and converted into the brightness of corresponding points. Finally, the corresponding image is displayed on the screen [27].

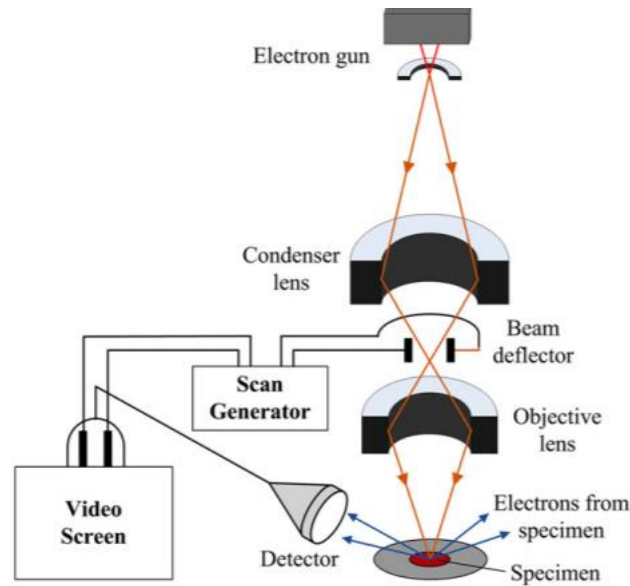


Figure 2-16. A schematic diagram of the SEM setup [27]

While in SEM, a focus electron beam which size primarily determines the resolution scans the sample, and the back scattered electrons and secondary electrons are collected for imaging the sample. By comparing with secondary electrons, back scattered electrons are more related to chemical elements and the resolution of back scattered electrons is also relatively lower. Therefore, secondary electron imaging is widely used in SEM equipment to characterize morphology.

The energy dispersive X-ray (EDX) tracks the fluorescence X-rays emitted from elements in the sample using the electron beam as an excitation source. It is a surface analytical technique where an electron beam hits the sample, exciting an electron in an inner shell, causing its ejection and the formation of an electron-hole in the electronic structure of the element [28]. Its characterization capabilities are due in large part to the fundamental principle that each element has a unique atomic structure allowing a unique set of peaks on its X-ray emission spectrum [29]. For elemental characterization, SEM usually has EDX to investigate the elemental distribution were on the sample's surface. In both Chapter 3 and Chapter 4, EDX has been introduced to confirm whether the phosphorus exists or not.

2.4. Reference

1. J. Cutler, D. Chapman, L. Dallin, R. Lamb. The Brightest Light in Canada: The Canadian Light Source. *Quantum Beam Sci.* **2017**, *1*, 4.
2. Beamlines. <https://www.lightsource.ca/beamlines.html> (accessed by May. 25th. 2021)
3. SGM (11ID-1).
https://www.lightsource.ca/beamlines/details/high_resolution_spherical_grating_monochromator_sgm.html (accessed by May. 25th. 2021)
4. T. Regier, J. Paulsen, G. Wright, I. Coulthard, K. Tan, T. K. Sham, R. Blyth. Commissioning of the Spherical Grating Monochromator Soft X-ray Spectroscopy Beamline at the Canadian Light Source. *AIP Conf Proc.* **2007**, 879, 473
5. About the Beamline. <https://sxrmb.lightsource.ca/about/> (accessed by May. 25th, 2021)
6. Taiwan Photon Source (TPS), introduction.
<https://www.nsrcc.org.tw/english/tps.aspx> (accessed by May 25th. 2021)
7. Beamline Map. <http://tpsbl.nsrcc.org.tw/index.aspx?lang=en> (accessed by May 26th.2021)
8. 23A X-ray Nanoprobe.
http://tpsbl.nsrcc.org.tw/bd_page.aspx?lang=en&pid=1026&port=23A (accessed by May 26th.2021)
9. B.H. Lin, X.Y. Li, D.J. Lin. et al. Investigation of Cavity Enhanced XEOL of a Single ZnO Microrod by Using Multifunctional Hard X-ray Nanoprobe. *Sci Rep.* **2019**, *9*, 207
10. The Advance Photon Source List of Parameters, compiled by H. M. Bizek, July 1996.
http://www.aps.anl.gov/Science/Publications/techbulletins/content/files/APS_142_1579.pdf (accessed by May 26th. 2021)
11. Beamlines Map. <https://www.aps.anl.gov/Beamlines/Beamlines-Map> (accessed by May 26th. 2021)

12. S.M. Heald, D.L. Brewster, E.A. Stern, K.H. Kim, F.C. Brown, D.T. Jiang, E.D. Crozier, R.A. Gordon. XAFS and micro-XAFS at the PNC-CAT beamlines. *J. Synchrotron Rad.* **1999**, *6*, 347
13. P. Ewart. X-rays: transitions involving inner-shell electrons. In *Atomic Physics*. Morgan & Claypool Publisher: San Rafael, 2019, p.9-1-9-6.
14. A.C. Thompson. et al. *X-ray Data Booklet* [Online]; Lawrence Berkeley National Laboratory, University of California, 2001, 2.
<https://books.google.ca/books?id=WV05HAAACAAJ> (accessed Jul. 11th, 2021)
15. J. Li, C. Liu, X. Li, Z. Wang, Y. Shao, S. Wang, X. Sun, W. Pong, J. Guo, T.K. Sham. Unraveling the Origin of Visible Light Capture by Core–Shell TiO₂ Nanotubes. *Chem. Mater.* **2016**, *28*, 4467
16. J.J. Rehr, R.C. Albers. Theoretical approaches to x-ray absorption fine structure. *RMP.* **2000**, *72*, 621.
17. J. Li, T.K. Sham, Y. Ye, J. Zhu, J. Guo. Structural and optical interplay of palladium-modified TiO₂ nanoheterostructure. *J. Phys Chem. C.* **2015**, *119*, 2222
18. M. Newville. *Fundamentals of XAFS. consortium for advanced radiation sources*. University of Chicago, Chicago, IL, 2004.
19. A. Erbil, W. Weber. Cargill III, G., Boehme, R. Lattice distortions for arsenic in single-crystal silicon. *Physical Review B.* **1986**, *34*, 1392
20. C. Dallera, L. Duo, L. Braicovich, G. Panaccione, G. Paolicelli, B. Cowie, J. Zegenhagen, Looking 100 Å deep into spatially inhomogeneous dilute systems with hard X-ray photoemission. *Appl. Phys. Lett.* **2004**, *85*, 4532
21. T.K. Sham, R. Sammynaiken, Y.J. Zhu, P. Zhang, I. Coulthard, S.J. Naftel. X-ray excited optical luminescence (XEOL): a potential tool for OLED studies. *Thin Solid Films* **2000**, *363*, 318
22. Z. Wang, X. Guo, T.K. Sham. 2D XANES-XEOL Mapping: Observation of Enhanced Band Gap Emission from ZnO Nanowire Arrays. *Nanoscale.* **2014**, *6*, 6531
23. Y. Nie, Z. Wang, J. Wang, F. Bao, J. Zhang, Y. Ma, T.K. Sham, X. Sun. Synthesis and Structure-Dependent Optical Properties of ZnO Nanocomb and ZnO Nanoflag. *J. Phys. Chem. C.* **2017**, *121*, 26076

24. T.K. Sham, S. Naftel, P.S. Kim, R. Sammynaiken, Y. Tang, I. Coulthard, A. Moewes, J. Freeland, Y.F. Hu, S. Lee, Electronic structure and optical properties of silicon nanowires: A study using x-ray excited optical luminescence and x-ray emission spectroscopy. *Phys. Rev. B.* **2004**, *70*, 045313.
25. F. Sima, C. Ristoscu, L. Duta, O. Gallet, K. Anselme, I.N. Mihailescu. Laser thin films deposition and characterization for biomedical applications. In *Laser Surface Modification of Biomaterials*. R. Vilar, Ed.; Woodhead publishing: Sawston, 2016, p.77-125.
26. M. Kaliva, M. Vamvakaki. Nanomaterials characterization. In *Polymer Science and Nanotechnology*. R. Narain, Ed.; Elsevier: Amsterdam, 2020, p.401-433
27. F.Y. Zhu, Q.Q. Wang, X.S. Zhang, W. Hu, X. Zhao, H.X. Zhang. 3D nanostructure reconstruction based on the SEM imaging principle, and applications. *Nanotechnology*. **2014**, *25*, 185705
28. A. Polini, F. Yang. Physicochemical characterization of nanofiber composites. In *Nanofiber Composites for Biomedical Applications*. M. Ramalingam, S. Ramakrishna, Ed.; Woodhead Publishing: Cambridge, 2017, p.97-115
29. G.C. Wang. Slag processing. In *The Utilization of Slag in Civil Infrastructure Construction*. Woodhead Publishing: Cambridge, 2016, p.87-113

Chapter 3

3 XANES and XEOL studies of both undoped and P-doped ZnO nano/microparticles prepared by hydrothermal method

3.1. Introduction

Zinc oxide nanoparticle is one of the inorganic compounds of group II–IV semiconductor for analytical sensing applications because it has a wide band gap of 3.4 eV and a large binding energy of 60 meV. These optoelectronic properties provide ZnO excellent chemical, electrical, and thermal stabilities. Due to its optical, electrical, and photocatalytic properties, ZnO is one of the most popular researched studies in nanomaterials due to its ability to apply in varied applications, such as solar cells, photocatalysis, and chemical sensor. It is also the second most abundant metal oxide and it can be prepared easily with relatively low-cost set up [1]. As mentioned in Chapter 1, ZnO is an intrinsic n-type semiconductor due to the existence of nonstoichiometric defects in the crystal lattice such as the oxygen vacancy and zinc interstitial. To strengthen the n-type doping of ZnO, either zinc can be substituted by group III elements or oxygen can be substituted with group VII elements. P-type ZnO can be synthesized by using dopant such as group I element or group V elements. However, there are some limitations. For example, the poor solubility of p-type dopants as well as the compensation between p-type dopants and n-type impurities within the ZnO crystal lattice. Many of dopant elements also function as deep acceptors instead of introducing p-type conductivity under ambient conditions [2]. Therefore, how to synthesize p-type ZnO and investigate its chemical and optical properties remains challenging.

In this chapter, both P-doped and undoped ZnO nano/microrods have been synthesized on the substrate of a Si wafer by hydrothermal method. $\text{NH}_4\text{H}_2\text{PO}_4$ was used as the phosphorus source to prepare P-doped ZnO nano/microrods. Two doping levels have been achieved by controlling the concentration of $\text{NH}_4\text{H}_2\text{PO}_4$ in the $\text{Zn}(\text{Ac})_2$ solution. Two reaction temperatures also have been introduced through the synthesis. Figure 3-1 shows a typical photo of the ZnO products grown on a piece of Si wafer (5 mm x 5 mm) via the hydrothermal method. The white-grey powder on the top of Si wafer is the ZnO

nano/microstructure. Scanning electron microscopy (SEM), energy dispersive X-ray (EDX), X-ray powder diffraction (XRD), X-ray absorption near-edge structure (XANES) spectroscopy were used to determine and investigate the morphology, composition, structure, and electronic structure of the prepared samples respectively. X-ray excited optical luminescence (XEOL) has also been introduced to find optical properties for undoped ZnO sample.

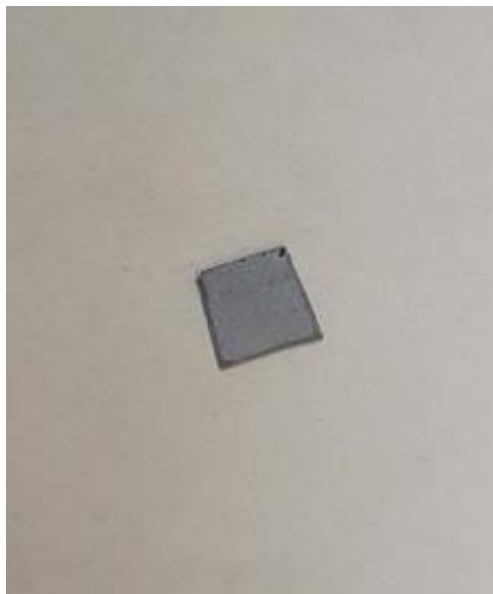


Figure 3-1. A photo of the undoped ZnO grown on the Si wafer via hydrothermal method.

3.2. Experimental

3.2.1. Synthesis of both undoped and P-doped ZnO particles

Deposition of ZnO seed layer on Si wafer: Before the hydrothermal growth of ZnO, a 10nm thick ZnO film was deposited on n-type Si (100) wafer by magnetron sputtering. Then the substrate was annealed under the ambient atmosphere at 400 C° for 1 hour to crystallize the ZnO thin film that would act as a seed layer for the growth of ZnO nano/microstructures [3].

Synthesis of P-doped ZnO structure: 10mM zinc acetate, 10mM hexamethylenetetramine and 2mM $\text{NH}_4\text{H}_2\text{PO}_4$ were dissolved in deionized (DI) water to produce 20mL solution.

Then 6.3mL solution was transferred to a Teflon-lined stainless-steel autoclave of 10.5mL capacity. A piece of ZnO thin film/Si wafer (5 mm x 5 mm) was put into the solution. The tank was heated in the oven at 100C° for 24hours. After the reaction, the sample was washed by DI water and dried under the ambient atmosphere at 60C° for 4 hours. In the end, the sample was annealed in the oven at 400C° for 2 hours [3]. To tune different P-doping levels in ZnO, another sample was synthesized by following the same procedures, but with 1.5mM NH₄H₂PO₄. Also, to explore the effect of reaction temperature on the morphology and size of the product, another synthesis was carried at 120 C° with all other parameters identical.

Synthesis of undoped ZnO structure: undoped ZnO nanorods were also grown following the same procedures and conditions in the synthesis of P-doped ZnO, without adding NH₄H₂PO₄ [3].

Table 3-1 summaries all sample names, descriptions, reaction temperatures and NH₄H₂PO₄ concentrations. The schematic diagram for the general experimental preparation and procedure for the ZnO synthesis by hydrothermal technique has been mentioned in Chapter 1. Figure 3-2 shows the general experimental procedure for the ZnO synthesis by hydrothermal method in my project.

Table 3-1. A summary of sample names, descriptions, reaction temperatures and NH₄H₂PO₄ concentrations for each sample.

Sample Name	Sample Description	Reaction Temperature (°C)	NH₄H₂PO₄ Concentration (mM)
ZnO powder	Purchased from Sigma Aldrich	N/A	N/A
ZnO: n-100	Undoped ZnO	100	N/A
ZnO: n-120	Undoped ZnO	120	N/A
ZnO: p-100-2	P-doped ZnO with relatively high level of P	100	2

ZnO: p-120-2	P-doped ZnO with relatively high level of P	120	2
ZnO: p-100-1.5	P-doped ZnO with relatively low level of P	100	1.5
ZnO: p-120-1.5	P-doped ZnO with relatively low level of P	120	1.5

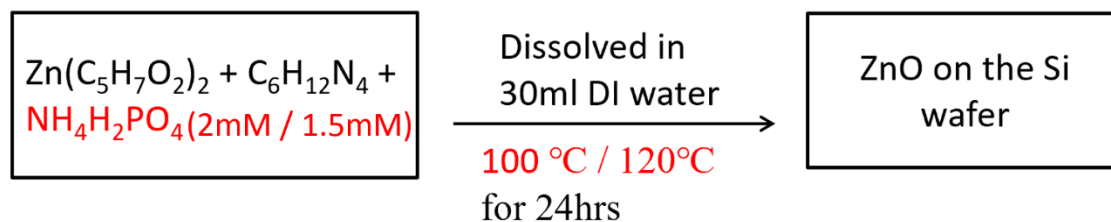


Figure 3-2. The general experimental procedure for the ZnO synthesis by hydrothermal technique

3.2.2. Characterization

The structure and morphology of the samples were characterized by XRD, (Rigaku, Co K-alpha radiation), SEM, (LEO 1530XB SEM and LEO1540 XB FIB/SEM with EDX) in Earth Science and the nanofabrication of Western, respectively. O K-edge, Zn L_{3,2}-edge and P K-edge XANES measurements were carried out at the high-resolution spherical grating monochromator (SGM) and Soft X-ray Microcharacterization Beamlines (SXRMB) at Canadian Light Sources (CLS) in Saskatoon, Saskatchewan. XANES was recorded in total electron yield (TEY) and partial fluorescence yield (PFY) mode. TEY was detected with the sample current and PFY was measured by detecting fluorescence X-ray emitted from the element of interest. As mentioned in chapter 2, TEY is surface sensitive and PFY is bulk sensitive because fluorescence X-ray can penetrate much deeper in solid than the electron [4]. Zn K-edge (PFY mode only) was also measured at sector 20-BM-B at Advance Photon Source of Argonne National Laboratory in Illinois, USA. XEOL measurement was carried out at the 23A X-ray Nanoprobe at the Taiwan Photon Source (TPS) in Hsinchu, Taiwan, China.

3.3. Results and discussion

3.3.1. SEM

SEM has been introduced to characterize the morphology of undoped and P-doped ZnO. Figure 3-3 and 3-4 are the SEM images for both undoped and P-doped ZnO structures. As shown in Figure 2, there are large amounts of rod-liked on the substrate. In Figure 3, the cross-section of these rods shows hexagonal shape. Table 3-2 summaries the average diameter and the structural shape for both undoped and P-doped ZnO structures.

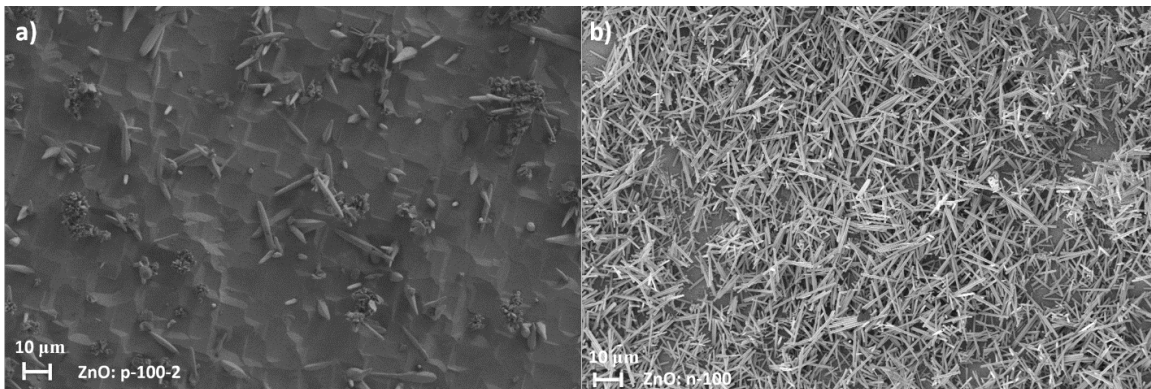


Figure 3-3. Low magnification SEM images of undoped and P-doped ZnO. a) ZnO: p-100-2. b) ZnO: n-100.

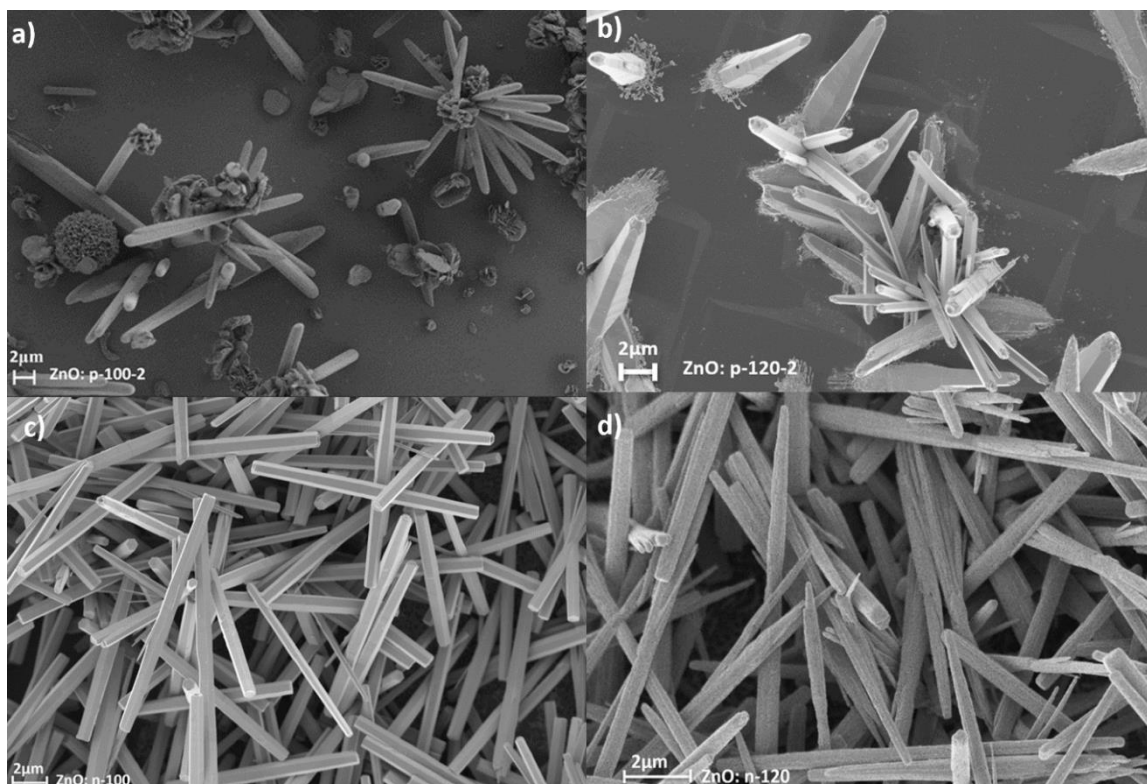


Figure3- 4. SEM images of undoped and P-doped ZnO. a) ZnO: p-100-2. b) ZnO: p-120-2. c) ZnO: n-100. d) ZnO: n-120.

Table 3-2. A summary of the morphology and the average diameter of undoped and P-doped ZnO prepared via hydrothermal method.

Sample Name	Average Diameter	Morphology	Average Length	Error Bar (diameter)
ZnO: n-100	550 nm	rod	12 μm	± 100 nm
ZnO: n-120	500 nm	rod	12 μm	± 100 nm
ZnO: p-100-2	1.1 μm	rod	4 μm	± 300 nm
ZnO: p-120-2	800 nm	rod	4 μm	± 200 nm

By comparing image 3-3a) and 3-3b), much more products can be found on the substrate in image 3-3b than image 3-3a, which means undoped ZnO product has more quantity than P-doped ZnO products. This phenomenon may be caused by the phosphorus dopant changing the growing environment of the ZnO crystal and affecting the growth of ZnO crystals. The precursor concentration determines the density of the rod distribution. When

the first generation of nanorods appears, further nucleation would be more likely to participate in the growth of existing nanorods instead of forming a new nucleus on the Si substrate [5]. Since the phosphorus substitute the Zn in P-doping ZnO products; therefore, the concentration of Zn^{2+} is influenced in P-doping ZnO products and affects the value of surface coverage.

By comparing image 3-4a) and 3-4b), morphologies of both P-doped ZnO products prepared at different temperature are the same. However, the average diameter for these two undoped ZnO products are slightly different. The average diameter for ZnO: p-100-2 structure is around 1 μm , and the average diameter for ZnO: p-120-2 structure is around 800 nm. The average length for ZnO: p-100-2 structure is around 12 μm and the average length for ZnO: p-120-2 is around 4 μm . Therefore, the temperature has more influences on the average diameter of ZnO products. The sizes of nanorods are strongly dependent on the concentration of Zn^{2+} [5, 6]. An increase in temperature of the solution leads to an increase in the rate of the chemical reactions. HMTA has been decomposed rapidly and produces more OH^- with water. This leads to enhancing nucleation and growth. Zn^{2+} would react with OH^- and produce ZnO rapidly. As I mentioned, further nucleation would be more likely to participate in the growth of existing nanorods; therefore, the growth of ZnO rods would be along the [0001] zone axis. Thus, the product would be long and thin. The width of ZnO nanorod can be reduced by increasing temperature [5, 6]. During the synthesis, the reaction temperature for ZnO: p-120-2 is higher than ZnO: p-100-2; therefore, the ZnO: p-120-2 structure would have a smaller width than ZnO: p-100-2 structure.

By comparing image 3-4c) and 3-4d), morphologies of both undoped ZnO products prepared at different temperature are the same. The average diameter for ZnO: n-100 structure is around 500 nm, and the average diameter for ZnO: n-120 structure is around 500 nm. The average length for ZnO: p-100-2 structure is around 12 μm and the average diameter for ZnO: p-120-2 is around 12 μm as well. This is corresponding to the P-doped ZnO products, which also indicates the temperature would affect the average diameter of ZnO products and proves the width of ZnO nanorod can be reduced by increasing the temperature. In the meantime, ZnO: n-120 has more needle-shaped structures than ZnO: n. As mentioned above, as the temperature increases, HMTA would decompose rapidly and

produce more OH^- with water. This would lead to enhancing nucleation and growth. However, rapid growth nanostructures cause a fast depletion of the reserves of Zn^{2+} . Thus, at the later stages of growth, the formation of full-shaped rods becomes impossible and leads to the formation of needle-shaped [5].

3.3.2. EDX

EDX has been used to determine the atomic percentage and elemental distribution of ZnO: p-100-2 and ZnO: p-100-1.5. Figure 3-5 illustrates the distribution of zinc, oxygen, phosphorus in ZnO: p-100-2 structures and ZnO: p-100-1.5 structures. Table 3-3 lists the atomic percentage and ratio for zinc, oxygen and phosphorus of ZnO: p-100-2 and ZnO: p-100-1.5 respectively.

Table 3-3. A summary of atomic percentage and percentage ratio for zinc, oxygen and phosphorus of ZnO: p-100-2 and ZnO: p-100-1.5

Sample	Element	Weight%	Atomic %	Atomic % ratio (P vs O/P/Zn)
ZnO: p-100-2	O	16.5	34.39	4.74:100
	P	1.51	1.63	100:100
	Zn	53.31	27.19	5.99:100
ZnO: p-100-1.5	O	21.93	45.34	0.97:100
	P	0.41	0.44	100:001
	Zn	68.28	34.56	1.27:100

As shown in table 3-3, the atomic % ratio between P and Zn which is $1.63: 27.19 = 5.99\%$ and the ration of P to Zn in table 2, that is $0.44: 34.56 = 1.27\%$. So, this means that p-100-2 has about 6% P substituting Zn or around 5 times more P than that of p-100-1.5 which is around 1%. By looking at the molar ratio of P and Zn, for ZnO: p-100-2, the molar ratio between P and Zn is $2:10 = 20\%$. For ZnO: p-120-1.5, the molar ratio between P and Zn is $1.5:10$. By comparing the atomic % ratio and molar ratio, the atomic % ratio between Zn and P is much lower than the molar ratio; therefore, it can conclude that not all phosphorus

has been doped into the ZnO lattice and substitute the Zn. However, by looking at the ratio between P and Zn, the substitution exists; thus, the phosphorus substitutes the Zn in P-doped ZnO products.

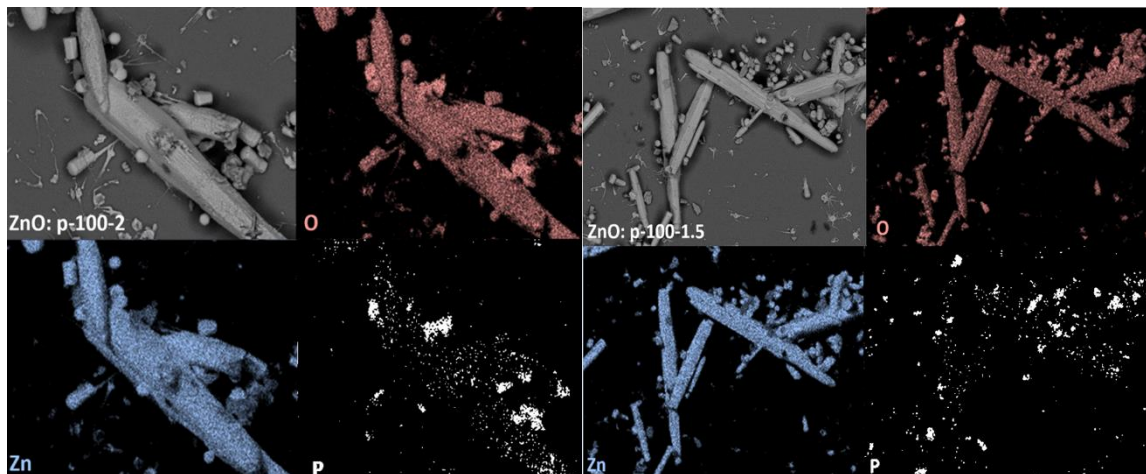


Figure 3-5. the EDX mapping of zinc, oxygen, phosphorus in ZnO: p-100-2 structures and ZnO: p-100-1.5 structures.

As shown in Figure 3-5, the majority elements of for both ZnO: p-100-2 and ZnO: p-100-1.5 are Zn and O. There are phosphorus signals can be found for both P-doped ZnO structures as well, but signals are very weak as expected based on the EDX, and they are most noticeable in the few scattered particles which are likely unreacted precursors. However, there is a P distribution that matches that of the Zn and O signal. Thus Figure 3-5 also suggests that the phosphorus has been doped into the ZnO crystal structures.

3.3.3. XRD

XRD has also been used to determine the crystalline lattice of ZnO nano/microstructures and investigate whether phosphorus is successfully doped into the ZnO crystal lattice. Figure 3-6 is the XRD pattern for both undoped ZnO nanostructures and P-doped ZnO nano/microstructures. All peaks are indexed to wurtzite- structure ZnO with lattice constant $a = 0.3232$, $c = 0.5209\text{nm}$ (JCPDS 80-0075), indicating that the products deposited on the substrate are all wurtzite ZnO.

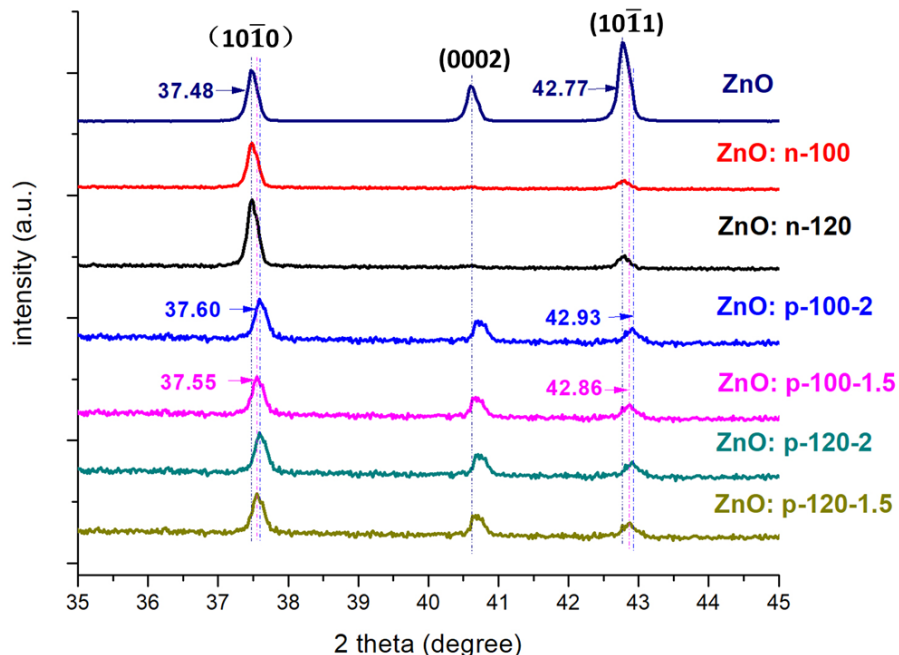


Figure 3-6. the XRD pattern of ZnO: n-100, ZnO: n-120, ZnO: p-100-2, ZnO: p-120-2, ZnO: p-100-1.5 and ZnO: p-120-1.5 at (10 $\bar{1}$ 0), (0002) and (10 $\bar{1}$ 1) diffraction peak.

By comparing all diffraction peaks, there is a small 2θ shift between undoped ZnO and P-doped ZnO products. As mentioned, the principle of XRD is based on the Bragg's law ($n\lambda = 2d\sin\theta$) where λ stands for the wavelength of the X-ray (Co K α), d stands for the lattice spacing, and θ stands for the angle of diffraction, and n is the order of diffraction. Since the whole number of wavelengths ($n\lambda$) does not change, therefore, if d becomes larger, then θ will become smaller or d becomes smaller, and θ becomes larger. In figure 3-6, comparing (10 $\bar{1}$ 0), (0002) and (10 $\bar{1}$ 1) diffraction peaks between undoped ZnO and P-doped ZnO products, the diffraction peaks of P-doped ZnO products shifts to the higher angle which indicates that the angle of diffraction becomes larger, and d becomes smaller in P-doped ZnO. Since, the atomic radius of phosphorous is smaller than the zinc but bigger than oxygen, therefore, this observation indicates that the P ions substitute the Zn site in ZnO crystal lattice. In the meantime, by comparing the angle shift, ZnO: p-100-2 and ZnO: p-120-2 has bigger shifts (0.11°) compare to ZnO: p-100-1.5 and ZnO: p-120-1.5 (0.07°). This is due to the concentration of phosphorus dopant. Since ZnO: p-100-2 and ZnO: p-120-2 have higher phosphorus atomic percentage (from EDX results); that is that more Zn atoms have been substituted by the phosphorus (also correspond to the P: Zn atomic

percentage ratio in EDX). Therefore, the lattice spacing in ZnO: p-100-2 and ZnO: p-120-2 are responsible for the upward shift.

3.3.4. XANES

To determine the local structure of undoped and P-doped ZnO products, XANES has been introduced. The main advantage of this technique is that it is elemental and site-sensitive, and it does not require a single crystal [7]. XANES deals with the measurement and interpretation of the near edge region, from just below to ~ 50 eV above the absorption threshold of the X-ray absorption fine structure (XAFS). There are two yields can be recorded for XANES measurement. One is total electron yield (TEY), another is partial fluorescence yield (PFY). TEY is surface sensitive because of the relative short sampling depth of electron. PFY is bulk sensitive because it is measured by detecting the X-ray fluorescence photon from the element of interest [8]. As mentioned in precious chapters, XANES is highly sensitive to the local environment of the element of interest, and this is because, for XANES measurement, the incident photon energy must be greater than the binding energy of core electrons, electrons will not be exited into the continuum where they can meet neighbouring elements which may be present; the backscattering of the photoelectron by neighbouring atom will modulate the absorption coefficient which carries all the information about the neighbouring atom [8]. In the case of a free atom in the gas phase, the XANES is monotonic. It is the modulation upon this monotonic background that contains information of the neighbouring atoms. In this chapter, Zn K-edge and L_{2,3}-edge, O K-edge and P K-edge XANES results will be discussed below.

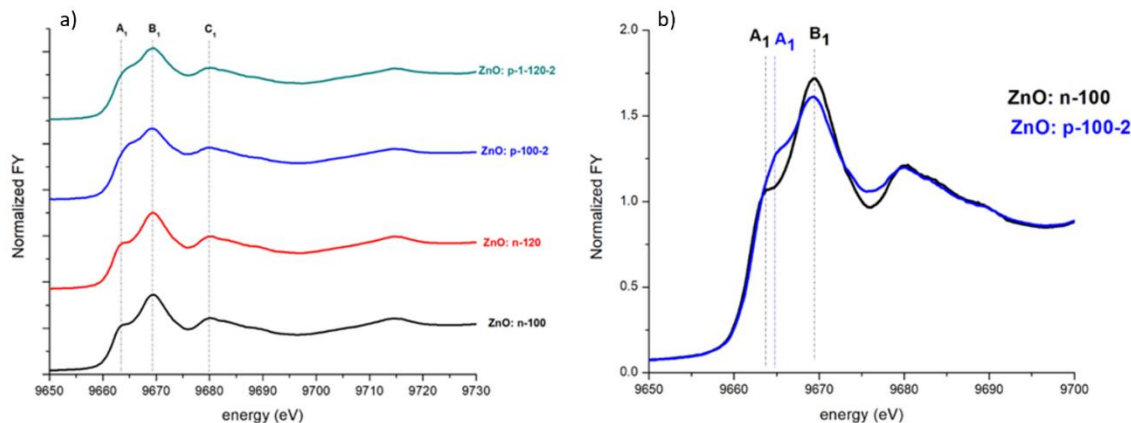


Figure 3-7. XANES spectrum of undoped and P-doped ZnO at Zn K-edge. a) XANES spectrum of ZnO: n-100, ZnO: n-120, ZnO: p-100-2 and ZnO: p-1-120-2 at the Zn K-edge in FY b) Zoom in of FY XANES of ZnO: n-100 and ZnO: p-100-2 at the Zn K-edge in FY

Figure 3-7a) shows the XANES spectrum of ZnO: n-100, ZnO: n-120, ZnO: p-100-2 and ZnO: p-1-100-1.5 at the Zn K-edge in FY mode. ZnO: n-100, ZnO: n-120, ZnO: p-100-2 and ZnO: p-1-120-2 shows the features of ZnO, which means that the local chemical environment of Zn in these samples are still in the ZnO lattice. According to the dipole-transition selection rule, the major features A_1 , B_1 , and C_1 are Zn 4p characters in the conduction band. In the figure, all the spectral features of the doped sample are broad, especially in the first two peaks. This indicates that the doped sample exhibit more disordered locally albeit the crystal structure remains intact. The disorder arises from doping changing the lattice constant slightly as seen in XRD and it can also be due to hybridization of the Zn 4p states with P 3sp states [9]. In Figure 3-7b), the undoped and P-doped ZnO are overlaid. The intensity of undoped ZnO has a higher intensity than P-doped ZnO at feature B_1 , and P-doped ZnO has a broader feature than undoped ZnO at A_1 position and the doped sample show broad features. In general, the feature for both P-doped and undoped ZnO products are very similar, if all nearest neighbors of Zn remain oxygen in a Td or slightly distorted Td environment, which suggests the neighbouring atom for Zn in ZnO lattice is only indirectly influence by the P-doping leading the lattice distortion and local disorder. This is an evidence which can help to confirm that the phosphorus does not substitute the oxygen. Finally, since ZnO: n-100 and ZnO: n-120 have the same feature, ZnO: p-100-2 and ZnO: p-1-120-2 have the same feature as well and the P content is on

the order of 1 to a few %; therefore, the temperature difference has little influence on the local chemical environment of the Zn.

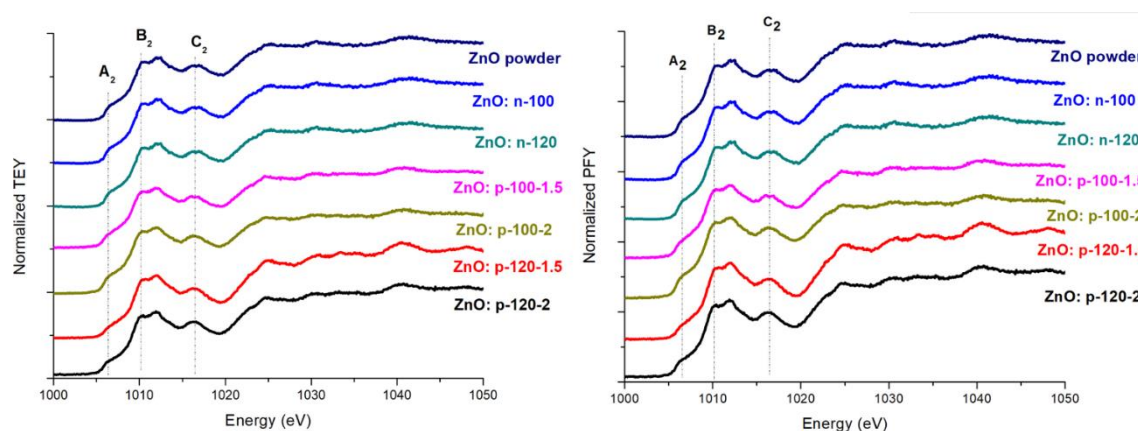


Figure 3-8. XANES spectrum of undoped and P-doped ZnO at Zn K-edge. a) XANES spectrum of ZnO: n-100, ZnO: n-120, ZnO: p-100-2 and ZnO: p-1-120-2 at the Zn K-edge in FY b) Zoom in of FY XANES of ZnO: n-100 and ZnO: p-100-2 at the Zn K-edge in FY

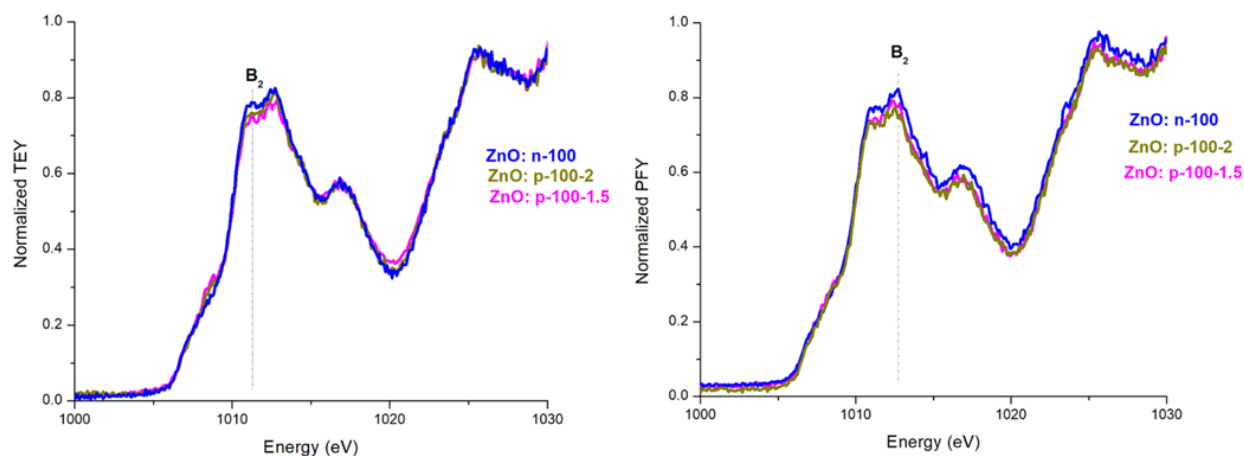


Figure 3-9. Zoom in of XANES spectrum of ZnO: n-100, ZnO: p-100-2, ZnO: p-, ZnO: p-100-1.5 at Zn $L_{3,2}$ -edge in TEY and PFY

Figure 3-8 shows the XANES spectrum of ZnO: n-100, ZnO: n-120, ZnO: p-100-2, ZnO: p-120-2, ZnO: p-100-1.5 and ZnO: p-120-1.5 at the Zn $L_{3,2}$ -edge in TEY and PFY mode. The E_0 of Zn $L_{3,2}$ -edge is 1010.3 eV. It needs to be noted that L-edge can be divided as L_1 , L_2 and L_3 edge. These three different edges indicate different electronic transition through different orbitals. According to the dipole-transition rule, At the L_1 edge, electron

transition is from 2s orbital to p orbital, and at L₂ and L₃ edge, electron transition takes place from 2p_{1/2} and 2p_{3/2} orbital to d and s orbital, respectively. At the Zn L_{3,2}-edge, the XANES spectra provide the information of the lowest unoccupied Zn 3d and 4s states. Since the Zn 3d orbital is fully occupied in general, the lowest unoccupied orbital of the Zn is 4s. Thus, the Zn L_{3,2}-edge XANES probes zinc 2p to 3d and 4s transition (3d is full and only has a little character in the conduction band). In Figure 3-8, feature A₂ is the 4s orbital, feature B₂ and C₂ are d like states [10]. Both TEY and PFY of ZnO: n-100, ZnO: n-120, ZnO: p-100-2, ZnO: p-120-2, ZnO: p-100-1.5 and ZnO: p-120-1.5 show the same features of ZnO, which means that the local chemical environment of Zn in these samples are in the ZnO lattice. In figure 8, the undoped and P-doped ZnO are overlaid in TEY and PFY mode. In figure 3-9, there is no obvious energy shift and huge intensity difference between undoped and P-doped ZnO. Therefore, both TEY and PFY mode suggest the neighbouring atoms Zn on the surface and in ZnO lattice remain intact upon P-doping. This result is in correspondence to the result from Zn K-edge. In the meantime, the TEY mode has the same feature as PFY mode, therefore the sample is thin and shows no thickness effect.

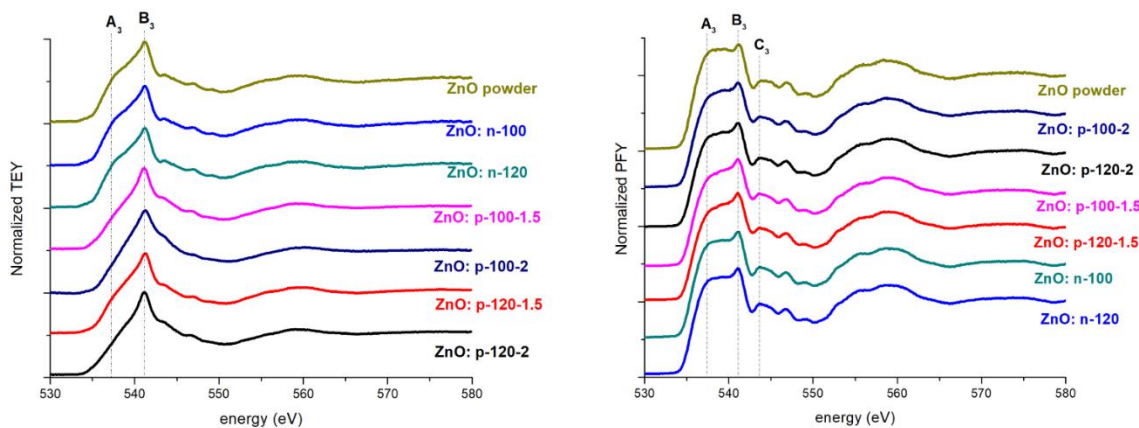


Figure 3-10. XANES spectrum of ZnO: n-100, ZnO: n-120, ZnO: p-100-2, ZnO: p-120-2, ZnO: p-100-1.5 and ZnO: p-120-1.5 at O K -edge in TEY and PFY

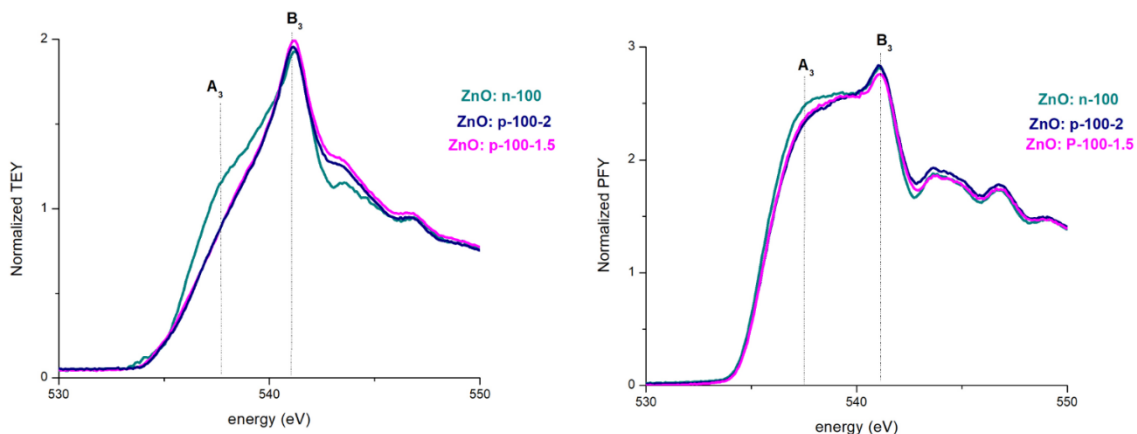


Figure 3-11. Zoom in of XANES spectrum of ZnO: n-100, ZnO: p-100-2, ZnO: p-, ZnO: p-100-1.5 at O K-edge in TEY and PFY

Figure 3-10 shows the XANES spectra of ZnO: n-100, ZnO: n-120, ZnO: p-100-2, ZnO: p-120-2, ZnO: p-100-1.5 and ZnO: p-120-1.5 at the O K-edge in TEY and PFY mode. The E_0 of O K-edge is 540.3 eV. Both TEY and PFY of ZnO: n-100, ZnO: n-120, ZnO: p-100-2, ZnO: p-120-2, ZnO: p-100-1.5 and ZnO: p-120-1.5 show the features of ZnO, which means that the local chemical environment of O in these samples are in the ZnO lattice. The area between the feature A_2 and B_2 is O 2p states hybridized with Zn 3d t_{2g} and 3d e_g states [11]. The feature C_3 is O 2p orbital hybridized with Zn 4sp states [11]. For both TEY and PFY mode, the intensity of feature A_3 is very small, and this is because Zn 3d orbital is full. The intensity of feature B_3 is raising, and this is due to the contribution from Zn 4s-O 2p hybridized states. In figure 11, the undoped and P-doped ZnO are overlaid in TEY and PFY mode. By looking at the intensity of feature A_3 in Figure 3-11, all P-doped ZnO products have a lower intensity than undoped ZnO products, especially in TEY mode. This is because of the hybridization of O 2p states with P 3sp states upon P doping and increase covalency. These phenomena indicate the bonding neighbor atom affect the local environment of O and suggest the phosphorus substitute the Zn in the ZnO lattice. The PFY mode has different features with TEY mode, and this is because the TEY mode is surface sensitive and the PFY mode is bulky sensitive. At this energy, the penetration depth of the fluorescence X-ray is short, the sample is too thick and PFY suffers self-absorption which reduces the fluorescence X-rays reaching the detector.

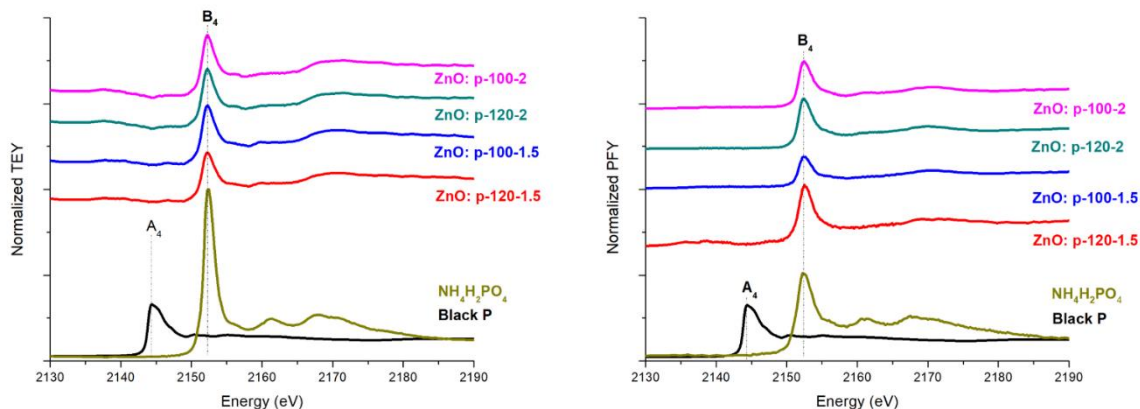


Figure 3-12. XANES spectrum of ZnO: p-100-2, ZnO: p-120-2, ZnO: p-100-1.5 and ZnO: p-120-1.5, $\text{NH}_4\text{H}_2\text{PO}_4$, black phosphorus at P K-edge in TEY and PFY

P K-edge XANES was also collected to probe the local chemical environment of P in P doped ZnO samples and further provide the information on where P sits in the lattice of wurtzite ZnO. Figure 3-12 is the XANES spectrum of ZnO: p-100-2, ZnO: p-120-2, ZnO: p-100-1.5 and ZnO: p-120-1.5, $\text{NH}_4\text{H}_2\text{PO}_4$, black phosphorus at P K-edge in TEY and PFY mode. The absorption peak for P K-edge is 2152.1 eV. At P K-edge, electron transition from P 1s orbital to 3p orbital. Both TEY and PFY modes have the same feature which indicates that the distribution is homogeneous and there is no thickness effect because the P fluorescence X-ray has long attenuation length. By comparing the white line position for each doped ZnO product, the white line is much closer to the feature B_4 than the feature A_4 , which means the oxidation state of phosphorus in all ZnO crystal lattice is the same as P_2O_5 , which is 5^+ . Therefore, the phosphorous substitutes the Zn in ZnO lattice, because if the phosphorous substitutes the oxygen in ZnO, then the lattice structure would become to PZn_4 like, and the XANES spectrum should be more like as oxygen K-edge diagram and the oxidation state of phosphorous is 3^- . Now the XANES spectrum looks more like the PO_4^{3-} moiety, and the oxidation state of phosphorous is 5^+ which indicates the phosphorous substitute the Zn instead of the O in ZnO lattice. In the meantime, results from Zn K-edge, Zn $L_{3,2}$ -edge, O K-edge all strongly suggest the bonding neighbor atom affect the local environment of the O. By combing all the XANES information, as well as the XRD results, it can be concluded that the phosphorous substitutes the Zn in hexagonal ZnO lattice. Since the local structure is PO_4 , the geometry should be tetrahedral.

3.3.5. XEOL

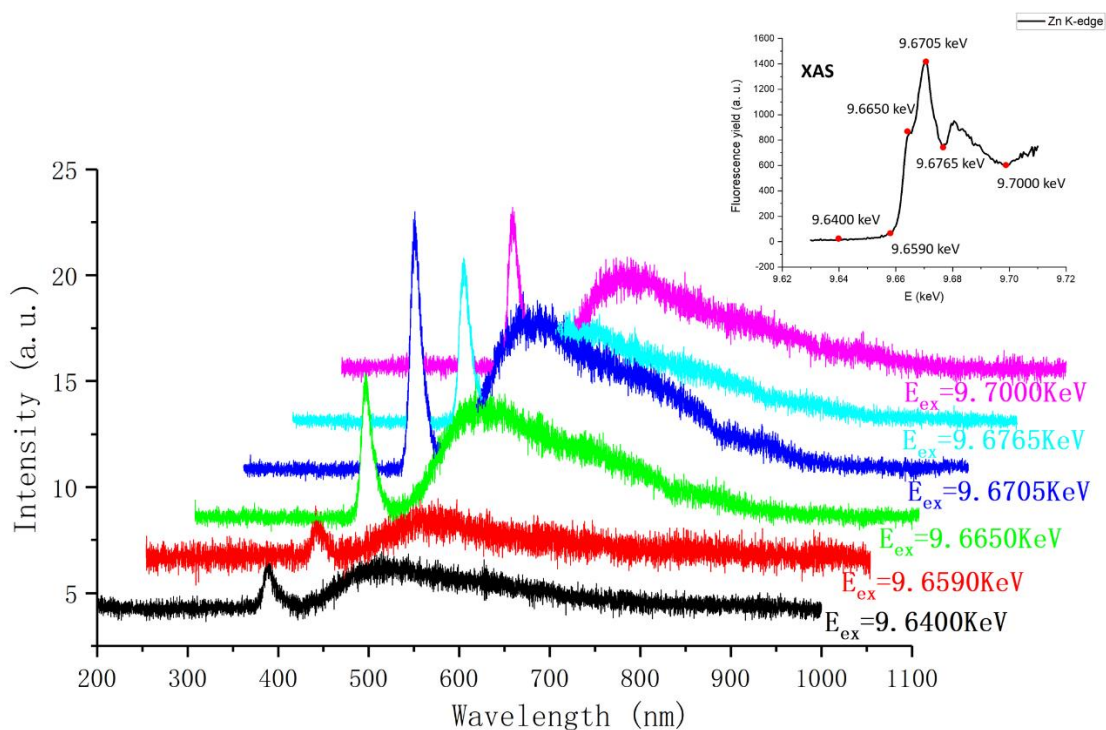


Figure 3-13. XEOL spectra of ZnO: n-100 under the excitation X-ray energy set across the Zn K-edge

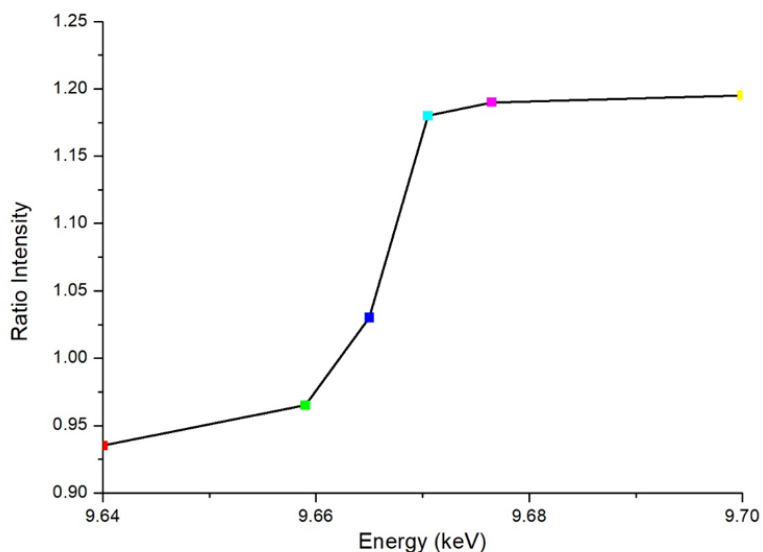


Figure 3-14. The intensity ratio (I_{NBE}/I_{DE}) with different X-ray energies at Zn K-edge. Figure 3-13 shows the XEOL spectra of ZnO: n-100 under the excitation X-ray energy set across the Zn K-edge measured at room temperature. The insert image is the XANES

spectra of ZnO: n-100 at the Zn-Kedge in FY mode. In XEOL spectrum, there are two peaks. The first peak is at around 388nm which belongs to the near band gap emission (NBE). The second peak is around 516nm which belongs to the defect emission (DE) of oxygen vacancy. According to the XEOL spectra, there is significant branching ratio change with increasing excitation energy across the Zn K-edge. The highest emission intensity for both NBE and DE is occurred at the X-ray energy of 9.6705 keV. The DE is dominant in the XEOL spectra when the X-ray energy is below the threshold energy of the Zn K-edge (9.659 keV). The intensities of both NBE and DE increases slightly when the X-ray energy is approaching to the threshold. When the X-ray energy is higher than the threshold, the NBE emission intensity increases more rapidly than the DE intensity. When the X-ray energy is higher than the 9.6705 keV, then intensity of both NBE and DE are decreasing, and keep decreasing with higher X-ray energies. Figure 3-14 shows the ratio between the intensity of NBE and the intensity of DE with the six X-ray energies at 9.64, 9.659, 9.665, 9.6705, 9.6765 and 9.7 keV respectively. According to the calculation, the estimated I_{NBE}/I_{DE} are around 0.93, 0.97, 1.03, 1.18, 1.19, 1.20 respectively. In figure 14, the intensity ratio increases rapidly when the X-ray energy is just above the threshold and changes a little when the X-ray energy keeps increasing. These phenomena can be explained by the increase of absorption and the thermalization of electrons and holes in the XEOL process. Thermalization of the Zn KLL Auger electrons which are produced by excitation above threshold can rapidly transfer their energy to the NBE optical channel. Energy transfer to defect states in the bandgap will lead to luminescence in longer wavelengths and a decrease in the BG luminescence [12]. Since the NBE is around 388nm, the bandgap for undoped ZnO is around 3.20eV which is close to the reference value (3.37eV) [13] where absorption is at the maximum.

3.4. Conclusion

In this chapter, I have synthesized undoped and P-doped ZnO products by hydrothermal method. The phosphorus doping source is $\text{NH}_4\text{H}_2\text{PO}_4$ and concentration levels are 1.5 and 2mM. The temperature levels are 100 and 120°C. All ZnO materials are grown on the Si substrate. SEM images show morphologies of all ZnO products are rod liked. The cross-section of these rods shows hexagonal shape. SEM images also suggest the temperature

and the dopant affect the average diameter of the ZnO micro/nanorod. With the higher reaction temperature, ZnO nanorods produce a smaller value of average diameter. EDX results suggest there are phosphorus signals in ZnO lattice. The mapping results suggest the phosphorus distributes throughout the rod but most noticeably at the edge of the ZnO micro/nanorod. The EDX composition indicates that the atomic percentage ratio of the phosphorus is lower than the molar ratio of the precursors. XRD results suggest that the phosphorus dopes into the ZnO material successfully, and the lattice structure for both undoped and P-doped ZnO material are slightly contracted hexagonal. XRD results also indicate the dopant concentration has influenced on the lattice constant. XANES results agree with results from XRD and EDX. Zn K-edge, Zn L_{3,2}-edge, O K-edge results all suggest the presence of dopant affects the local environment albeit the crystal structure is maintained. The P-K-edge results indicate that the oxidation state of phosphorus in all P-doped ZnO products is 5⁺, and that the P substitutes the Zn site in the ZnO lattice. The XEOL results suggest the bandgap for undoped ZnO is around 3.20eV. The highest emission intensity for both NBE and DE is occurred at the X-ray energy of 9.6705 keV.

3.5. Reference

1. T. Lakshmipriya, S.C.B. Gopinath. Introduction to nanoparticles and analytical devices. In *Nanoparticles in Analytical and Medical Devices*. S.C.B. Gopinath, F. Gang, Ed.; Elsevier: Amsterdam, 2021, p.1-29
2. J. Miao, B. Liu. II–VI semiconductor nanowires: ZnO. In *Semiconductor Nanowires*. J. Arbiol, Q. Xiong, Ed.; Woodhead Publishing: Cambridge. 2015. p.3-28
3. X. Fang, J. Li, D. Zhao, D. Shen, B. Li, X. Wang. Phosphorus-Doped p-Type ZnO Nanorods and ZnO Nanorod p-n Homojunction LED Fabricated by Hydrothermal Method. *J. Phys. Chem. C*. **2009**, *113*, 21208
4. A. Polini, F. Yang. Physicochemical characterization of nanofiber composites. In *Nanofiber Composites for Biomedical Applications*. M. Ramalingam, S. Ramakrishna, Ed.; Woodhead Publishing: Cambridge, 2017, p.97-115

5. V. Gerbreders, M. Krasovska, E. Sledevskis, A. Gerbreders, I. Mihailova, E. Tamanis, A. Ogurcovs. Hydrothermal Synthesis of ZnO nanostructures with controllable morphology change. *CrystEngComm* **2020**, 22, 1346
6. D. Polsongkram, P. Chamninok, S. Pukird, L. Chow, O. Lupan, G. Chai, H. Khallaf, S. Park, A. Schulte. Effect of synthesis conditions on the growth of ZnO nanorods via hydrothermal method. *Physica B Condens. Matter.* **2008**, 403, 3713
7. S.J. Gurman. EXAFS and XANES studies of Metallic Glasses. In *Rapidly Quenched Metals*. S. Steeb, H. Warlimont, Ed.; North Holland: Amsterdam, 1985, p.427-430
8. Z. Wang, J. Wang, T.K. Sham, S. Yang. Origin of Luminescence from ZnO/CdS Core/Shell Nanowire Arrays. *Nanoscale.* **2014**, 6, 9783
9. V. Vaithianathan, J.H. Moon, C.H. Chang, K. Asokan, S.S. Kim. Electronic Structure of P-Doped ZnO Films with p-Type Conductivity. *J. Nanosci. Nanotechnol.* **2006**, 6, 3422
10. Y. Nie, Z. Wang, J. Wang, F. Bao, J. Zhang, Y. Ma, T.K. Sham, X. Sun. Synthesis and Structure-Dependent Optical Properties of ZnO Nanocomb and ZnO Nanoflag. *J. Phys. Chem. C.* **2017**, 121, 26076
11. V. Vaithianathan, J.H. Moon, C.H. Chang, K. Asokan, S.S. Kim. Local electronic structure of phosphorus-doped ZnO films investigated by X-ray absorption near-edge spectroscopy. *Appl. Phys. A.* **2009**, 94, 995
12. Z. Wang, X. Guo, T.K. Sham. 2D XANES-XEOL mapping: observation of enhanced band gap emission from ZnO nanowire arrays. *Nanoscale*, **2014**, 6, 6531
13. J. Lee, D.C. Sorescu, X. Deng. Tunable Lattice Constant and Band Gap of Single and Few-Layer ZnO. *Phys. Chem. Lett.* **2016**, 7, 1335

Chapter 4

4. XANES and XEOL studies of both undoped and P-doped ZnO nano/microparticles prepared by chemical vapor deposition (CVD) method via vapor-liquid-solid (VLS) mechanism

4.1. Introduction

As mentioned in previous chapters, ZnO nanoparticle is one of the most popular researched topics in optoelectronic field since it has a wide band gap of 3.37 eV and a large binding energy of 60 meV. Since ZnO is a well-known intrinsic n-type semiconductor due to the existence of nonstoichiometric defects in the crystal lattice; therefore, how to synthesize high quality p-type ZnO semiconductor with doping and investigate their optoelectronic properties and local chemical structures are important and necessary. As introduced in Chapter 1, vapor-liquid-solid (VLS) is a very common technique used to produce high-quality and high-performance material under vacuum. By comparing with other synthesis methods, VLS can produce materials with high crystal quality purity and limited defects on the substrate [1]. Although VLS method have many advantages, there are still some weakness and disadvantages for VLS method. For example, researchers need to control the gas flow rate and reaction temperature preciously during the synthesis [2-4]. Even though, high flexibility and high growth rates make the VLS method attract extensive attraction on nanoparticles preparation.

In this chapter, both P-doped and undoped ZnO particles have been synthesized on the substrate of Si wafer by VLS technique. P_2O_5 was used as the phosphorus source to prepare P-doped ZnO particles. Two different gas flow rates and three substrate positions have been introduced during the P-doped ZnO synthesis. Figure 4-1 shows a typical photo of the ZnO products grown on Si wafer via VLS technique under UV excitation. The green luminous part on the top of Si wafer is ZnO products. Scanning electron microscopy (SEM), energy dispersive X-ray (EDX), X-ray powder diffraction (XRD), X-ray absorption near-edge structure (XANES) spectroscopy were used to determine and investigate the

morphology, composition, structure, and electronic structure of prepared samples respectively. X-ray excited optical luminescence (XEOL) has also been used to find optical properties for undoped ZnO sample.



Figure 4-1. A photo of the ZnO products grown on Si wafer via CVD technique under UV excitation.

4.2. Experimental

4.2.1. Synthesis of both undoped and P-doped ZnO particles.

Deposition of Au layer on Si wafer: Before the CVD growth of ZnO, a 10nm thick Au layer was deposited on n-type Si (100) wafer by sputtering at the Nanofabrication lab, UWO. The Au layer would act as a catalyst layer for the growth of ZnO particles [4].

Synthesis of P-doped ZnO particles: 1g Zn powder (99.99%, Alfa Aesar) and Ar gas were used as starting materials. 0.03g P_2O_5 has been chose as the P dopant. The synthesis processes are following steps: first, the Zn powder was placed in an Al boat. Next, the boat and the Si wafer were placed in a tube furnace. A constant gas flow rate (80sccm) was maintained during the growth process. During the growth process, the reaction temperature was kept at 550°C, and the temperature in the furnace was increased at 10°C /min, respectively for 1 hour [3-5]. To achieve the relationship between substrate positions and the morphology and size of the product, three different position distances have been introduced as 16cm, 19cm, 21 cm, respectively with all other parameters identical. To explore the effect of gas flow rate on the morphology and size of the product, one additional synthesises were carried out by changing the gas flow rate as 75 sccm with all other parameters identical.

Synthesis of undoped ZnO structure: undoped ZnO microstructure were also grown following the same procedures and conditions in the synthesis of P-doped ZnO, without adding P_2O_5 .

The schematic diagram for the general experimental set up for the ZnO synthesis by CVD technique and the general mechanism for ZnO synthesis via VLS mechanism are introduced in Chapter 1. Figure 4-2 shows the general experimental set up for the ZnO synthesis by CVD technique in my project. Table 4-1 summaries all sample names, descriptions, gas flow rates and substrate position distances for all ZnO samples

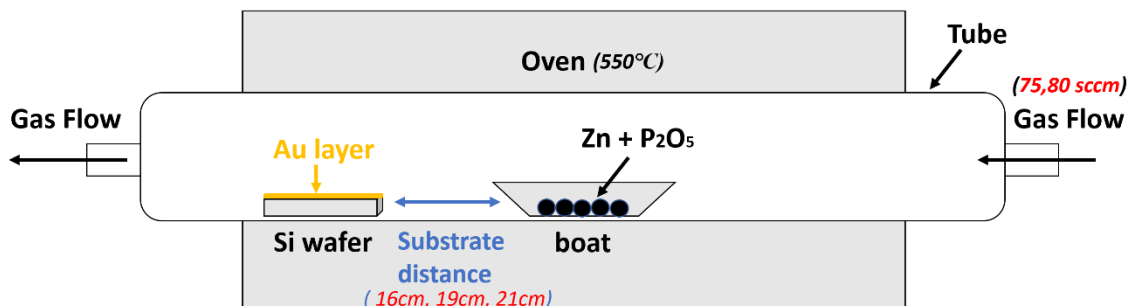


Figure 4-2. The schematic diagram for the general experimental set up for the ZnO synthesis by CVD technique in my project.

Table 4-1. A summary of all sample names, descriptions, gas flow rates and substrate position distances for all ZnO samples

Sample Name	Sample Description	Gas Flow Rate (sccm)	Substrate Position Distance (cm)
ZnO	Purchased from Sigma Aldrich	n/a	n/a
ZnO: n-80-16	Undoped ZnO products with relative low gas flow rate	80	16
ZnO: p-75-16	P-doped ZnO products with relative low gas flow rate	75	16
ZnO: p-80-16	P-doped ZnO products with relative high gas flow rate	80	16

ZnO: p-80-19	P-doped ZnO products with relative high gas flow rate	80	19
ZnO: p-80-21	P-doped ZnO products with relative high gas flow rate	80	21

4.2.2. Characterization

The structure and morphology of the samples were characterized by XRD, (Rigaku, Co K-alpha radiation), SEM, (LEO 1530XB SEM and LEO1540 XB FIB/SEM with EDX) in Earth Science and the nanofabrication of Western, respectively. P K-edge XANES measurements were carried out at the Soft X-ray Microcharacterization Beamlines (SXRMB) at Canadian Light Sources (CLS) in Saskatoon, Saskatchewan. XANES was recorded in total electron yield (TEY) and partial fluorescence yield (PFY) mode. As mentioned in previous chapters, TEY is surface sensitive, and it is detected with sample current. PFY is bulk sensitive, and it is measured by detecting fluorescence X-ray emitted from the element of interest. Zn K-edge (PFY mode only) and XEOL measurement was carried out at the 23A X-ray Nanoprobe at the Taiwan Photon Source (TPS) in Hsinchu, Taiwan, China.

4.3. Results and Discussion

4.3.1. XRD

XRD has also been used to determine the crystalline lattice of ZnO microstructures and investigate whether phosphorus is successfully doped into the ZnO crystal lattice. Figure 4-3 is the XRD pattern for both undoped ZnO nanostructures and P-doped ZnO microstructures. All peaks are indexed to wurtzite- structure ZnO with lattice constant $a = 0.3232$, $c = 0.5209$ nm (JCPDS 80-0075), indicating that the products deposited on the substrate are all wurtzite ZnO.

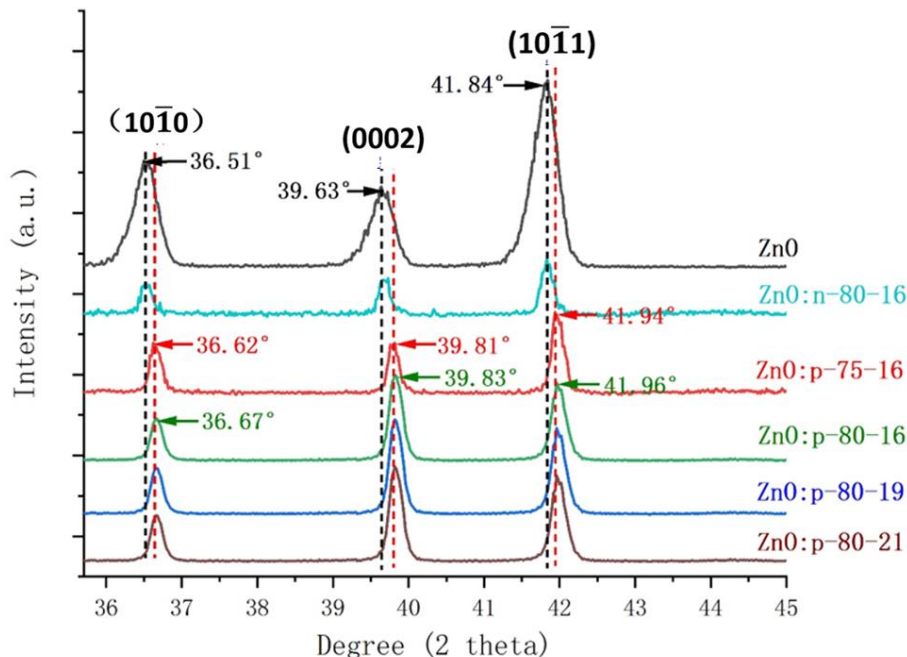


Figure 4-3. XRD pattern of ZnO: n-80-16, ZnO: p-75-16, ZnO: p-80-16, ZnO: p-80-19 and ZnO: p-80-21 at $(10\bar{1}0)$, (0002) and $(10\bar{1}1)$ diffraction peak.

By comparing all diffraction peaks, there is a small 2θ shift between undoped ZnO and P-doped ZnO products. As mentioned in previous chapters, the principle of XRD is based on the Bragg's law ($n\lambda = 2d\sin\theta$) where λ stands for the wavelength of the X-ray (Co K α), d stands for the lattice spacing, and θ stands for the angle of diffraction, and n is the order of diffraction. Since the whole number of wavelengths ($n\lambda$) does not change, therefore, if d becomes larger, then θ will become smaller or d becomes smaller, and θ becomes larger. In Figure 4-3, comparing $(10\bar{1}0)$, (0002) and $(10\bar{1}1)$ diffraction peaks from undoped ZnO and P-doped ZnO products, the diffraction peaks of P-doped ZnO products shifts to the higher angle which indicates that the angle of diffraction becomes larger, and d becomes smaller in P-doped ZnO. Since, the atomic radius of phosphorous is smaller than the zinc but bigger than oxygen, therefore, this observation indicates that the P ions substitute the Zn site in ZnO crystal lattice. In the meantime, by comparing the degree shift, there is no obvious degree shift among all ZnO: p-80 products. This phenomenon indicates the substrate positions do not affect the concentration of P during P-doped ZnO synthesis obviously. By comparing ZnO: p-80-16 and ZnO: p-75, there is a small degree shift. This may be due to the concentration of phosphorus in P-doped ZnO products. In the following

EDX results, by comparing the atomic percentage of P between ZnO: p-80-16 and ZnO: p-75-16, ZnO: p-80-16 has little higher atomic percentage of P than ZnO: p-75-16. Therefore, the lattice spacing in ZnO: p-80-16 is responsible for the upward shift.

By comparing the XRD results for P-doped ZnO products prepared by CVD technique with previous XRD results for those prepared by the hydrothermal method in Chapter 3, all the degree shifts for P-doped ZnO products are in the right direction. This phenomenon indicates all P ions substitute the Zn in ZnO lattice in sample prepared by the hydrothermal and VLS methods. In the meantime, by comparing the 2θ position for both undoped and P-doped ZnO results in Chapter 3 and Chapter 4, respectively, both undoped and P-doped ZnO results in Chapter 3 have higher 2θ than them in Chapter 4. This phenomenon may be due to the different morphologies for both undoped and P-doped ZnO products. In the following SEM results, the morphology for all ZnO products prepared by the VLS technique are films and rock-like, which are different from the SEM results in Chapter 3. All the P-doped ZnO products prepared by CVD technique also have higher 2θ shifts than those prepared by hydrothermal methods. This phenomenon suggests ZnO products prepared by the VLS technique have more P ion percentage than they prepared by hydrothermal methods.

4.3.2. SEM

SEM has been used to characterize the morphology of undoped and P-doped ZnO particles. Figure 4-4 and Figure 4-5 show the morphology of both undoped and P-doped ZnO particles. As shown in the figure, both undoped and P-doped ZnO are film like with irregular shape. Table 4-2 summaries the average diameter and the structural shape for both undoped and P-doped ZnO structures.

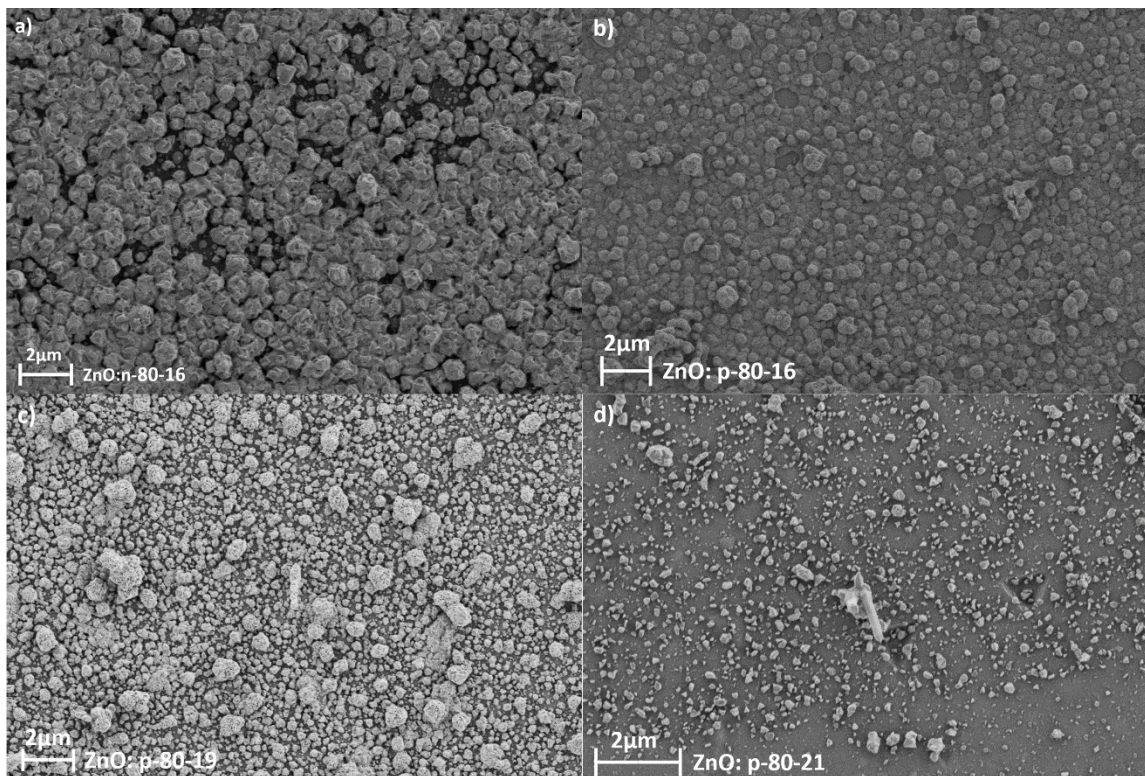


Figure 4-4. SEM images for both undoped and P-doped ZnO particles. a) ZnO: n-80-16, b) ZnO: p-80-16, c) ZnO: p-80-19, and d) ZnO: p-80-21

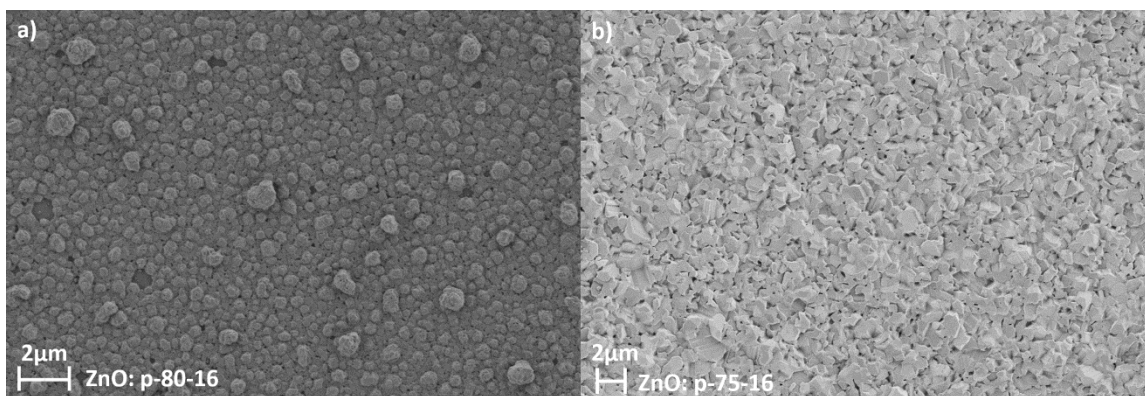


Figure 4-5. SEM images for P-doped ZnO p articles under different gas flow rate. a) ZnO: p-80-16, b) ZnO p-75-16

Table 4-2. A summary of the morphology and the average diameter of undoped and P-doped ZnO prepared via CVD technique.

Sample	Morphology	Average Diameter (nm)	Error Bar for Diameter (nm)
ZnO: n-80-16	rock	1000	±200
ZnO: p-75-16	film	1000	±200
ZnO: p-80-16	rock	1000	±200
ZnO: p-80-19	rock/rod	600	±100
ZnO: p-80-21	rock/rod	200	±20

By comparing Figure 4-4a) and Figure 4-4b), at the same substrate position and under the same gas flow rate, there are more products can be found on the substrate in Figure 4-4a) than Figure 4-4b), which means undoped ZnO product has more quantity than P-doped ZnO products. This phenomenon may be caused by the phosphorus dopant changing the growing environment of the ZnO particles and affecting the growth of ZnO products. As mentioned in Chapter 1, the chemical reaction for ZnO synthesis by CVD method is $2Zn + O_2 \rightarrow 2ZnO$ [6, 7]. The mechanism of ZnO synthesis can be mainly divided as two stages: the formation of zinc vapor, and the nucleation and oriented growth of ZnO [8]. First, the Zn powder would be heated until the gas phase. Then, the Zn vapor would react with Au layer and form alloy droplets. When the alloy droplet became supersaturated ZnO particles would be grown on the Si wafer surface [9]. Therefore, the amount of precursor (Zn) can be predicted as the dominant role during the ZnO synthesis process. Since the phosphorus substitute the Zn in P-doping ZnO products; therefore, the concentration of Zn^{2+} is influenced in P-doping ZnO products and affects the value of surface coverage, and the quantity of P-doped ZnO products is less than undoped ZnO products.

By comparing Figure 4-4b), Figure 4-4c) and Figure 4-4d), under the same gas flow rate with the same amount of precursors, Figure 4-4c) shows the highest quantity of ZnO products, and Figure 4-4d) shows the lowest quantity of ZnO products. This phenomenon may be due to different reaction temperatures. Although the reaction temperature was set as 550°C during the experiment, the temperature is still not fixed and may be different at

different tube zone. Figure 1-6 and Figure 4-2 illustrate the set up for the ZnO synthesis by CVD technique. As we can see in these figures, the substrate is placed in the downstream of the tube and the reaction temperature (550°C) can only be kept at the middle of oven. Therefore, as the further substrate position (higher value of the substrate distance), the reaction temperature is no longer as 550°C and it will be lower than the expected value. Thus, reaction temperatures for ZnO: p-80-16, ZnO: p-80-19 and ZnO: p-80-21 are different in real. Many literatures have already published that the morphology of ZnO particles by CVD method is highly related with reaction temperature [3-11]. For example, Lim and his colleagues found when the oven is heated to 450°C, the morphology of ZnO is nanopyramidal and when the oven is change to 500°C, the morphology of ZnO is nanorod [6]. Nie et al also successfully synthesized ZnO nanocomb and ZnO nanoflag at 900°C and 950°C, respectively [10]. Therefore, different reaction temperatures would affect the morphology of ZnO products seriously, and how to control the reaction temperature preciously during the synthesis remains many challenges. Kumar et al [11] found that at the low temperature ($\leq 600^\circ\text{C}$), the grown nanostructures have irregular shapes with large variation in their sizes in the range of nanometers to micrometers, which is very similar as my ZnO morphologies. This phenomenon may be attributed to the lack of Au seed layer [11]. When the temperature is not high enough, the melted Au catalyst layer and the Zn vapor cannot achieve the alloy droplet perfectly. Thus, the growth of nanorods is not possible as after nucleation on the substrate ZnO which will lead irregular shapes [11, 12].

By comparing Figure 4-5a) and Figure 4-5b), at the same position with the same value of precursors, Figure 4-5b) shows that the morphology of P-doped ZnO products is film like. This phenomenon is due to the gas flow rate. Lobacheva et al [3] found that ZnO particles display as nanocomb and nanorods when the insert gas is Ar/O₂ mixture with 50sccm/10 sccm. Xiang et al [13] found that ZnO particles display as nanowire when the inset gas is N₂/O₂ mixture. Therefore, the insert gas and the gas flow rate are also two important parameter which would affect the morphology and the growth of ZnO particles. ZnO: p-75-16 has the lower gas flow rate than ZnO: p-80-16 and only Ar has been introduced during the synthesis. Since the reaction temperature may not be high enough and the growth of nanorods is not possible after nucleation on the substrate; now, the gas flow rate may

also be lower than the expected value and the concentration of oxygen is not high enough to involve the whole reaction; therefore, the growth process of ZnO in ZnO: p-76-16 may not be finished, Thus, the SEM shows the morphology of ZnO: p-76-16 is film like instead of rock like. The EDX results also approve that ZnO: p-75-16 has lower O atomic percentage than ZnO: p-80-16.

4.3.3. EDX

EDX has been used to determine the atomic percentage and elemental distribution of ZnO: p-75 and ZnO: p-80-16. Figure 4-5 illustrates the distribution of zinc, oxygen, phosphorus in ZnO: ZnO: p-75-16 structures and ZnO: p-80-16 structures. Table 4-3 lists the atomic percentage and ratio for zinc, oxygen and phosphorus of ZnO: p-75 and ZnO: p-80-16 respectively.

Table 4-3. A summary of atomic percentage and percentage ratio for zinc, oxygen and phosphorus of ZnO: p-75-16 and ZnO: p-80-16.

Samples	Element	Weight%	Atomic%	Atomic % ratio (P vs O/P/Zn)
ZnO: p-80-16	O	25.43	58.06	0.91:100
	P	0.45	0.53	100:100
	Zn	74.12	41.41	1.27:100
ZnO: p-75-16	O	24.77	57.35	0.82:100
	P	0.41	0.47	100:100
	Zn	74.82	42.18	1.11:100

As shown in Table 4-3, the atomic % ratio between P and Zn for ZnO: p-80-16 is $0.53:41.41 = 1.27\%$ and the ratio of P to Zn for ZnO: p-75-16 is $0.47:42.18 = 1.11\%$. So, this means that ZnO: p-80-16 has about 1.27% P substituting Zn and 1.14 times more P than that of ZnO: p-75 which is 1.11%. Since the mass of P dopant for both P doped ZnO products are the same, it is reasonable that both products have almost the same concentration of P. By looking at the molar ratio of P and Zn, for ZnO: p-80-16, the molar

ratio between P and Zn is $0.211: 15:29 = 1.37\%$. Since the mass of Zn and P_2O_5 are the same for both P-doped ZnO products, the molar ratio of P and Zn are also the same. Therefore, the molar ratio of P and Zn for ZnO: p-75 is also 1.37%. By comparing the molar ratio and the atomic ratio, the value of atomic ratio is very close to the molar ratio; therefore, it can conclude that most of phosphorus has been doped into the ZnO lattice and substituted the Zn.

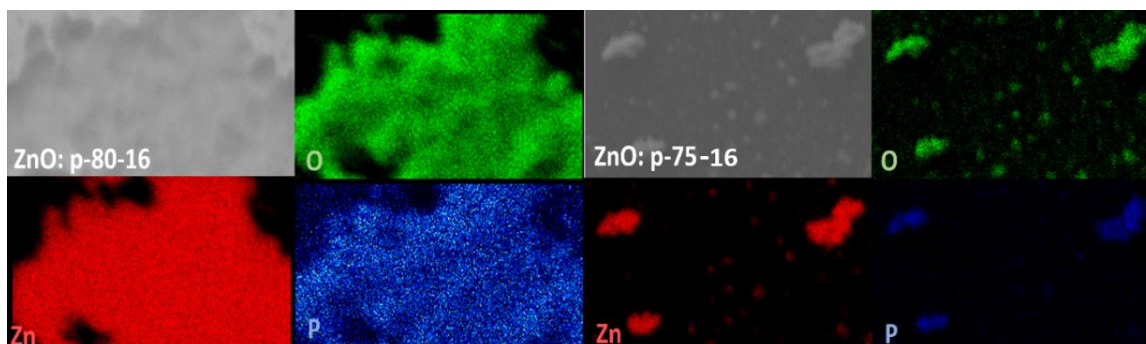


Figure 4-6. EDX mapping of zinc, oxygen, phosphorus in ZnO: p-80-16 structures and ZnO: p-75-16 structures.

As shown in Figure 4-6, the majority elements of for both ZnO: p-80-16 and ZnO: p-75-16 are Zn and O. There are phosphorus signals can be found for both P-doped ZnO structures as well, but signals are very weak as expected based on the EDX. There is a P distribution that matches that of the Zn and O signal. Thus Figure 4-6 also suggests that the phosphorus has been doped into the ZnO crystal structures.

By comparing the atomic percentage for P between ZnO: p-80-16 and ZnO: p-75-16, the difference between them is 0.06%. However, by comparing the atomic percentage for P in Chapter 3; the difference between two P-doped ZnO products is 1.19% which is a higher value. In the meantime, by comparing the EDX mapping of P in ZnO: p-80-16 and ZnO: p-75-16, the P distribution that matches that of the Zn and O signal homogenously. By comparing the EDX mapping of P in Chapter 3, although the P distribution also matches that of the Zn and O signal, the distribution is not evenly and there are some noticeable scattered particles that are likely unreacted precursors. Therefore, by combing all the EDX results in Chapter 3 and Chapter 4, the P-doped ZnO structures prepared by the VLS technique are more homogenous than those prepared by the hydrothermal method.

4.3.4. XANES

XANES has been used to determine the local structure of undoped and P-doped ZnO products. As mentioned in previous chapters, the main advantage of this technique is that it is elemental and site-sensitive, and this is because, for XANES measurement, the incident photon energy must be greater than the binding energy of core electrons, electrons will be excited into the continuum where they can meet neighbouring elements which may be present; the backscattering of the photoelectron by neighbouring atom will modulate the absorption coefficient which carries all the information about the neighbouring atom. For XANES measurement, there are two yield modes: total electron yield (TEY) and partial fluorescence yield (PFY) mode. TEY is surface sensitive because of the relative short sampling depth of the electron. PFY is bulk sensitive because it is measured by detecting the X-ray fluorescence photon from the element of interest. In this chapter, both TEY and PFY modes are recorded at P K-edge. Zn K-edge is only recorded with PFY mode.

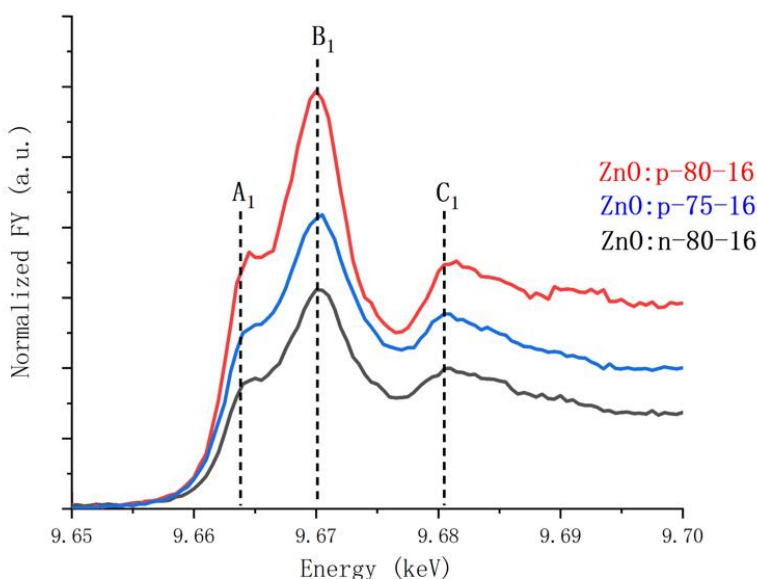


Figure 4-7. XANES spectra of ZnO: n-80-16, ZnO: p-75-16 and ZnO: p-80-16 at Zn K-edge in FY mode

Zn K-edge XANES was collected to probe the local chemical environment of Zn in both undoped and P-doped ZnO samples. Figure 4-7 is the FY XANES spectra of ZnO: n-80-16, ZnO: p-75-16 and ZnO: p-80-16 at Zn K-edge. ZnO: n-80-16, ZnO: p-75-16 and ZnO: p-80-16 shows the features of ZnO, which means that the local chemical environment of

Zn in these samples are still in the ZnO lattice. According to the dipole-transition selection rule, the major features A_1 , B_1 , and C_1 are Zn 4p characters in the conduction band. ZnO: p-75-16 has a broad feature at the A_1 position which indicates that the doped sample exhibit more disordered locally albeit the crystal structure remains intact. The disorder arises from doping changing the lattice constant slightly as seen in XRD and it can also be due to hybridization of the Zn 4p states with P 3sp states [14]. By comparing between ZnO: p-75-16 and ZnO: p-80-16, ZnO: p-80-16 has a sharper feature than ZnO: p-75-16 at A_1 position which is different from the hydrothermal products in Chapter 3. At the B_1 position, the intensities of P-doped ZnO products also have higher intensities than undoped ZnO products which are also different from the hydrothermal products. These phenomena may be caused by the morphology and the thickness of products. Since FY mode is bulk sensitive and the morphology between ZnO: p-75-16 and ZnO: p-80-16 are different; therefore, the feature for ZnO: p-75-16 and ZnO: p-80-16 may have slightly different. In general, the feature for both P-doped and undoped ZnO products are very similar, if all nearest neighbors of Zn remain oxygen in a Td or slightly distorted Td environment, which suggests the neighbouring atom for Zn in ZnO lattice is only indirectly influenced by the P-doping leading to the lattice distortion and local disorder. This is an evidence which can help to confirm that the phosphorus does not substitute the oxygen. At the meantime, since ZnO: n-80-16, ZnO: p-75-16 and ZnO: p-80-16 have a similar feature, and the P content is on the order of 1 to a few % as well; therefore, the gas flow rate difference has little noticeable influence on the local chemical environment of the Zn.

By comparing the Zn K-edge XANES results in samples prepared with hydrothermal and VLS methods, at the A_1 position, all P-doped ZnO products have a broad feature which indicates the disorder arises from doping changing the lattice. However, there is a small additional peak that can be found around the A_1 position for ZnO: p-80-16. Since the measurement is under the FY mode, therefore, this may be due to self-absorption. As mentioned, the intensities of P-doped ZnO products have higher intensities than undoped ZnO products at B_1 position. This phenomenon is also different from the Zn K-edge XANES results in Chapter 3. Since the general feature for all ZnO products is very similar in Chapter 3 and Chapter 4; therefore, both Zn K-edge XANES spectra suggest the neighbouring atom for Zn in ZnO lattice is only indirectly influenced by the P-doping

leading to the lattice distortion and local disorder, which indicates the phosphorus does not substitute the oxygen.

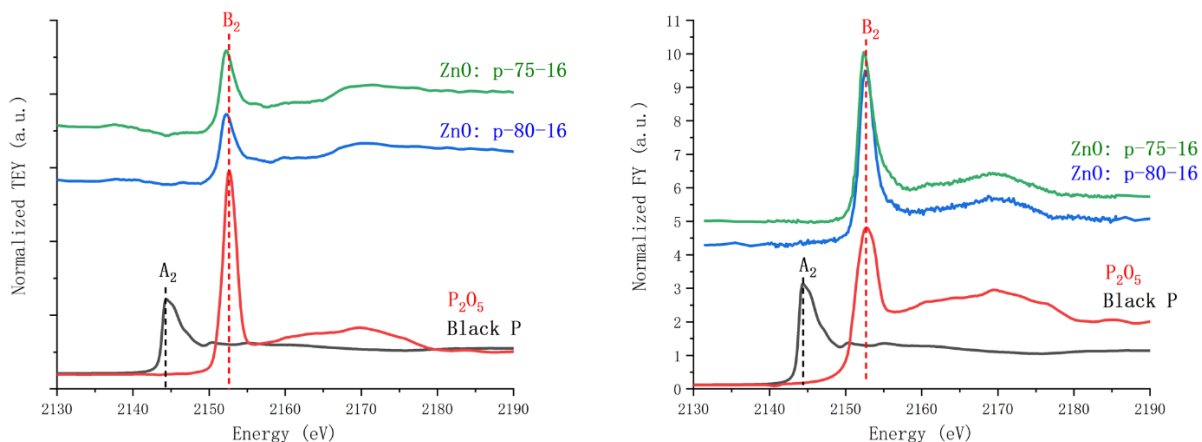


Figure 4-8. XANES spectrum of ZnO: p-75-16 and ZnO: p-80-16, P₂O₅ and black phosphorus at P K-edge in TEY and FY mode

P K-edge XANES was collected to probe the local chemical environment of P in P doped ZnO samples and further provide the information on where P sits in the lattice of wurtzite ZnO. Figure 4-8 are XANES spectrum of ZnO: p-75-16 and ZnO: p-80-16, P₂O₅ and black phosphorus at the P K-edge in TEY and FY mode. At the P K-edge, XANES tracks electron transition from P 1s orbital to 3p orbital in the tetrahedral environment if P is substituting Zn. Both TEY and PFY modes have the same feature which indicates that the distribution is homogeneous and there is no thickness effect because the P fluorescence X-ray has longer attenuation length than that from oxygen. By comparing the white line (spike at the edge due to high cross-section and high densities of states) position for each doped ZnO product, the white line is much closer to the feature B₂ (P(5⁺)) than the feature A₂ (P(0)), which means that the oxidation state of phosphorus in all ZnO crystal lattice is the same as P₂O₅, which is 5⁺. Therefore, the phosphorus substitute the Zn in ZnO lattice, because if the phosphorus substitutes the oxygen in ZnO, then the lattice structure would become to PZn₄ like, and the oxidation state of phosphorus is 3⁻. Now the XANES spectrum looks more like the PO₄³⁻ moiety, and the oxidation state of phosphorus is 5⁺ which indicates the phosphorus substitute the Zn instead of the O in ZnO lattice. Although there

is no O K-edge and Zn L_{3,2}-edge results for this chapter; both Zn K-edge and P K-edges results still strongly suggest the bonding neighbor atom affect the local environment of the O. Therefore, by combing all the XANES information and the XRD results, it can be concluded that the phosphorous substitutes the Zn in hexagonal ZnO lattice. Since the structure is PO₄, the geometry should be tetrahedral.

By comparing P K-edge XANES results for P-doped ZnO products prepared by VLS technique with previous P K-edge XANES results for those prepared by the hydrothermal method in Chapter 3, the oxidation state of phosphorus in all ZnO crystal lattice is 5⁺, respectively. Therefore, the phosphorous substitutes the Zn in ZnO lattice for all P-doped ZnO products in both chapters, respectively. The geometry for all P-doped ZnO products in both chapters are tetrahedral, respectively.

4.3.5. XEOL

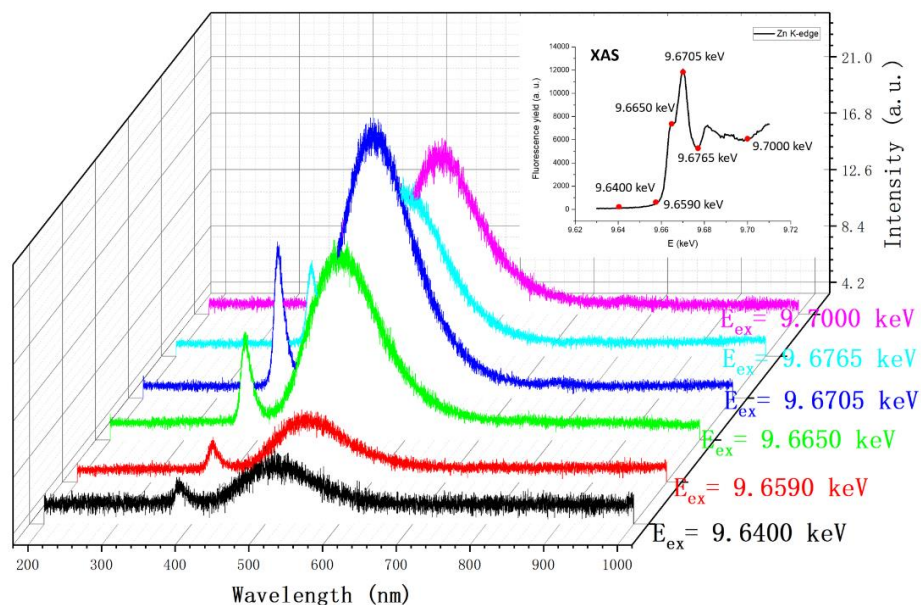


Figure 4-9. XEOL spectrum of ZnO: n-80-16 under the excitation X-ray energy set across the Zn K-edge measured at room temperature. The insert figure is the XANES spectra of ZnO: n-80-16 at FY mode.

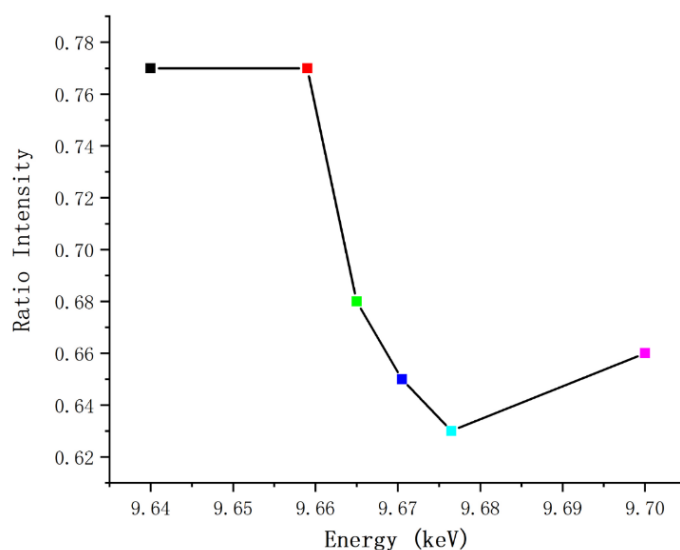


Figure 4-10. The ratio between the intensity of NBE and the intensity of DE with the six X-ray energies at 9.64, 9.659, 9.665, 9.6705, 9.6765 and 9.7 keV respectively. Figure 4-9 shows the XEOL spectrum of ZnO: n-80-16 under the excitation X-ray energy set across the Zn K-edge measured at room temperature. The insert figure is the XANES

spectra of ZnO: n-80-16 at FY mode. The first peak is at around 384nm which belongs to the near band gap emission (NBE). The second peak is around 510.7nm which belongs to the defect emission (DE) of oxygen vacancy. According to the XEOL spectra, there is significant branching ratio change with increasing excitation energy across the Zn K-edge. As observed in the hydrothermal ZnO products, the highest emission intensity for both NBE and DE is occurred at the X-ray energy of 9.6705 keV. However, the DE is dominant in the XEOL spectra among all excited energy levels in ZnO: n-80-16. This phenomenon indicates the ZnO: n-80-16 have more oxygen-based surface defect than undoped ZnO products prepared by hydrothermal method in Chapter 3. The intensities of both NBE and DE increases slightly when the X-ray energy is approaching to the threshold. When the X-ray energy is higher than the threshold, the NBE intensity increases more rapidly than the DE intensity. Similar observation for both NBE and DE can be also found by Wang et al [10, 15] and Lin et al [16] in ZnO nanorods with soft X-ray energy across the Zn L_{3,2}-edge and hard X-ray energy across the Zn K-edge. This is because the electron/ hole pair stops thermalization when the electron reaches the bottom of conduction band and the hole reaches the top of valence band. At the meantime, some excess energy transferring would improve the crystallinity of ZnO in the shallow region of structures [17]. The difference in my project is that when the X-ray energy is higher than the 9.6705 keV, then intensity of both NBE and DE are decreasing, and keep decreasing with higher X-ray energies. Figure 4-10 shows the ratio between the intensity of NBE and the intensity of DE with the six X-ray energies at 9.64, 9.659, 9.665, 9.6705, 9.6765 and 9.7 keV respectively. According to the calculation, the estimated I_{NBE}/I_{DE} at the above mentioned six energies are around 0.77, 0.77, 0.68, 0.65, 0.63, 0.66, respectively. In Figure 4-10, when the X-ray energy is approaching to the threshold, the intensity ratio keeps as the same. However, when the X-ray energy is higher than the threshold, the intensity ratio decreases rapidly. When the X-ray energy is 9.7 keV, the intensity ratio increases a little, but it is still lower than the first three intensity ratios. These phenomena are due to the high intensity of DE, which suggests that the crystal structure for ZnO: n-75-16 is imperfect. Since the NBE is around 384 nm, the bandgap for undoped ZnO is around 3.22eV which is close to the reference value (3.37eV) [17].

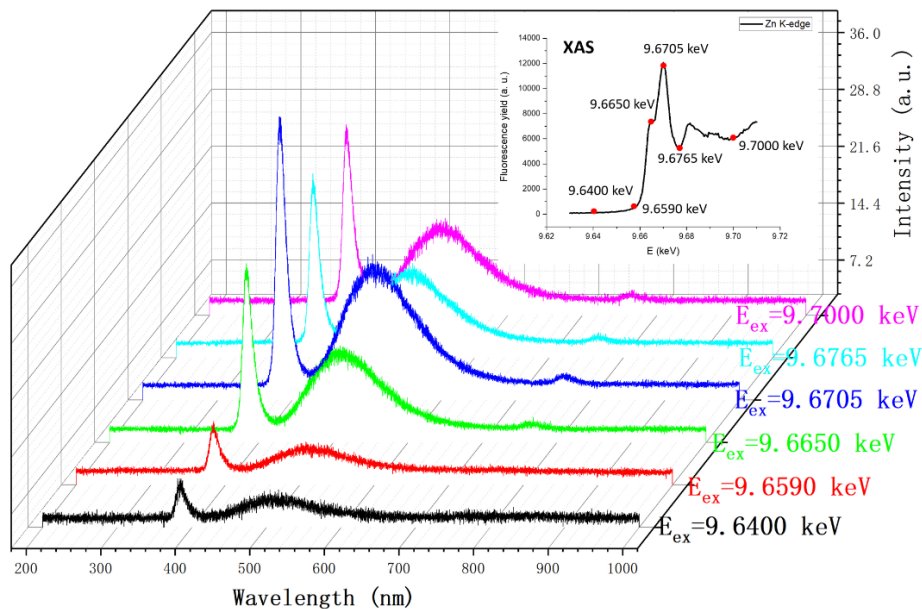


Figure 4-11. XEOL spectrum of ZnO: p-80-16 under the excitation X-ray energy set across the Zn K-edge measured at room temperature. The insert figure is the XANES spectra of ZnO: p-80-16 at FY mode.

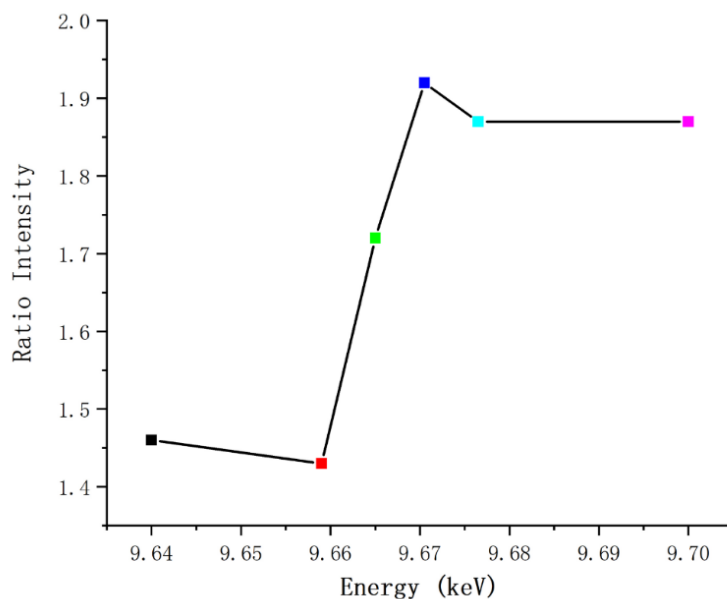


Figure 4-12. The ratio between the intensity of NBE and the intensity of DE with the six X-ray energies at 9.64, 9.659, 9.665, 9.6705, 9.6765 and 9.7 keV respectively. Figure 4-11 shows the XEOL spectrum of ZnO: p-80-16 under the excitation X-ray energy set across the Zn K-edge measured at room temperature. The insert figure is the XANES

spectra of ZnO: p-80-16 at FY mode. The first peak is at around 386 nm which belongs to the near band gap emission (NBE). The second peak is around 507.7nm which belongs to the defect emission (DE) of oxygen vacancy. According to the XEOL spectra. there is significant branching ratio change with increasing excitation energy across the Zn K-edge. As same as undoped ZnO products, the highest emission intensity for both NBE and DE is occurred at the X-ray energy of 9.6705 keV. However, the NBE is dominant in the XEOL spectra among all excited energy levels in ZnO: p-80-16. This phenomenon indicates that ZnO: p-80-16 has better crystallinity of ZnO and less oxygen-based surface defect than ZnO: n-80-16. This may be due to the P doping. According to the XRD and XANES results, the P substitute the Zn in ZnO lattice. Since the bond length of P-O bond (1.50Å) is less than Zn-O bond (1.89Å), it may affect the crystallinity of ZnO during the measurement. As observed in the ZnO: n-80-16, the intensities of both NBE and DE increases slightly when the X-ray energy is approaching to the threshold. When the X-ray energy is higher than the threshold, both the NBE intensity and DE intensity increases rapidly and the NBES intensity increases more rapidly than DE intensity until the X-ray energy reaches 9.6705 keV. Then the intensity of NBE and DE decreases rapidly until the X-ray energy becomes 9.7 keV. This phenomenon is similar as ZnO: n-80-16, except the arising and declining features in the P-doped ZnO sample is shaper than the undoped ZnO sample. This may also be due to the P dopant helps ZnO to improve its crystallinity after the thermalization. As mentioned, excess energy transferring would improve the crystallinity of ZnO in the shallow region of structures after the thermalization. With increasing X-ray energy, more excess energy is converted to improve the crystallinity of the ZnO structures. Therefore, the intensity of NBE is increasing more rapidly than the intensity of DE [15]. Figure 4-12 shows the ratio between the intensity of NBE and the intensity of DE with the six X-ray energies at 9.64, 9.659, 9.665, 9.6705, 9.6765 and 9.7 keV respectively. According to the calculation, the estimated I_{NBE}/I_{DE} at the above mentioned six energies are around 1.46, 1.43, 1.72, 1.92, 1.87,1.87, respectively. In Figure 4-12, when the X-ray energy is approaching to the threshold, the intensity ratio changes a little. When the X-ray energy is higher than the threshold, the intensity ratio increases rapidly until the X-ray energy is 9.6705 keV. When the X-ray energy is 9.7 keV, the intensity ratio decreases a little, but it is still higher. than the first three intensity ratios. By comparing the Figure 4-12 and the

Figure 4-10, the trend of intensity ratios between undoped and P-doped ZnO are opposite which may also suggest the P dopant changes the optical properties of ZnO structures. The P-doped ZnO products have better crystallinity and less oxygen-based surface defect than the undoped ZnO products. Since the NBE is around 386 nm, the bandgap for P-doped ZnO is around 3.21eV which is close to the theoretical value (3.37eV) [17] and less than the bandgap for undoped ZnO.

4.4. Conclusion

In this chapter, I have synthesized undoped and P-doped ZnO products by CVD method via the VLS mechanism. The phosphorus doping source is P_2O_5 . The temperature is 550°C. Three different positions with distances from the source have been denoted as 16cm, 19cm, and 21 cm. Two gas flow rates have also been introduced as 75 sccm and 80 sccm, respectively. All ZnO materials are grown on the Si substrate. SEM images show morphologies of all ZnO products are rock and film like. The cross-section of these ZnO shows hexagonal shape. SEM images also suggest the substrate position and gas flow rate affect the morphology and average diameter of the ZnO parties. EDX results suggest there are phosphorus signals in ZnO lattice. The mapping results suggest the phosphorus distributes throughout particles. The EDX composition indicates that the atomic percentage ratio of the phosphorus is closed to the molar ratio of the precursors. XRD results suggest that the phosphorus dopes into the ZnO material successfully, and the lattice structure for both undoped and P-doped ZnO material are slightly contracted hexagonal. XANES results agree with results from XRD and EDX. Zn K-edge results suggest the presence of dopant affects the local environment albeit the crystal structure is maintained. The P-K-edge results indicate that the oxidation state of phosphorus in all P-doped ZnO products is 5^+ , and that the P substitutes the Zn site in the ZnO lattice. The XEOL results suggest the bandgap for undoped ZnO is around 3.22eV and the bandgap for P-doped ZnO is around 3.21 eV. The highest emission intensity for both NBE and DE is occurred at the X-ray energy of 9.6705 keV where absorption is at the maximum in both undoped and P-doped ZnO products. The XEOL results also suggest the P dopant changes the optical properties of ZnO products as seen in the NBE and DE emission branching ratio improving the crystallinity of ZnO structures.

By comparing the XRD results for both undoped and P-doped ZnO products in Chapter 3 and Chapter 4, both XRD results indicate the P doped into the ZnO lattice and substitute the Zn. By comparing the 2θ position for both undoped and P-doped ZnO results in Chapter 3 and Chapter 4, respectively, both undoped and P-doped ZnO results in Chapter 3 have higher degrees than them in Chapter 4 which may be due to the different morphologies for both undoped and P-doped ZnO products in 2 chapters, respectively. All the P-doped ZnO products prepared by the CVD technique also have higher angle shifts than those prepared by hydrothermal methods which phenomenon suggests ZnO products prepared by the CVD technique have more P ion percentage than they prepared by hydrothermal methods. By comparing the EDX result for both undoped and P-doped ZnO products in Chapter 3 and Chapter 4, the difference of atomic percentage for P in Chapter 3 is higher than that value in Chapter 4. In the melamine, the distribution of P in Chapter 4 shows more homogenously than the distribution of P in Chapter 3. Therefore, by combing all the EDX results in Chapter 3 and Chapter 4, the P substitutes Zn in P-doped ZnO structures prepared by the CVD technique more homogenously and steadily than those prepared by the hydrothermal method. By comparing the Zn K-edge XANES spectrum between undoped and P-doped ZnO products in Chapter 3 and Chapter 4, all P-doped ZnO products have a broad feature at the A1 position which indicates the disorder arises from doping changing the lattice. Although the intensities of P-doped ZnO products have higher intensities than undoped ZnO products at B₁ position in Chapter 4 which is different from the Zn K-edge XANES results in Chapter 3, the general feature for all ZnO products is very similar in Chapter 3 and Chapter 4 which suggests the neighbouring atom for Zn in ZnO lattice is only indirectly influenced by the P-doping leading to the lattice distortion and local disorder, which indicates the phosphorus does not substitute the oxygen. The P K-edge XANES results in both Chapter 3 and Chapter 4 suggest that the oxidation state of P in P-doped ZnO is 5⁺ which also proves the phosphorus substitutes the Zn in hexagonal ZnO lattice in both chapters. By comparing the XEOL results for both undoped and P-doped ZnO products in Chapter 3 and Chapter 4, the undoped ZnO product prepared by the CVD technique have more oxygen-based surface defects than those prepared by the hydrothermal method. In the meantime, the P-doped ZnO products prepared by the CVD

technique have better crystallinity and less oxygen-based surface defects than the undoped ZnO products prepared by the hydrothermal method in described Chapter 3.

4.5. Reference:

1. Y.B. Pottathara, Y. Grohens, V. Kokol, N. Kalarikkal, S. Thomas. Synthesis and Processing of Emerging Two-Dimensional Nanomaterials. In *Nanomaterials Synthesis, Design, Fabrication and Applications*. Y.B. Pottathara, V. Kokol, N. Kalarikkal, Ed.; Elsevier: Amsterdam, 2019, p.1-25
2. P. Unnikrishnan, D. Srinivas. Heterogeneous Catalysis. In *Industrial Catalytic Processes for Fine and Specialty Chemicals*. S.S. Joshi, V.V. Ranade, Ed.; Elsevier: Amsterdam, 2016, p.41-111
3. O. Lobacheva, P.L. Corcoran, M.W. Murphy, J.Y.P. Ko, T.K. Shan. Cathodoluminescence, X-ray excited optical luminescence, and X-ray absorption near-edge structure studies of ZnO nanostructures. *Can. J. Chem.* **2012**, *90*, 298
4. S. Kumar, P.D. Sahare, S. Kumar. Optimization of the CVD parameters for ZnO nanorods growth: Its photoluminescence and field emission properties. *Mater. Res. Bull.* **2018**, *105*, 237
5. S. Swathi, R. Yuvakkumar. G. Ravi, E.S. Babu, D. Velauthapillai, S.A. Alharbi. Morphological exploration of chemical vapor–deposited P-doped ZnO nanorods for efficient photoelectrochemical water splitting. *Ceram. Int.* **2021**, *47*, 6521
6. T. Lim, P.S. Mirabedinib, K. Jung, P.A. Greaney, A.A. Martinez-Morales. High-index crystal plane of ZnO nanopyramidal structures: Stabilization, growth, and improved photocatalytic performance. *Appl. Surf. Sci.* **2021**, *536*, 147326
7. S. Swathi, R. Yuvakkumar, G. Ravi, E.S. Babu, D. Velauthapillai, S.A. Alharbi. Morphological exploration of chemical vapor–deposited P-doped ZnO nanorods for efficient photoelectrochemical water splitting. *Ceram. Int.* **2021**, *47*, 6521
8. H. Wan, H.E. Ruda. A study of the growth mechanism of CVD-grown ZnO nanowires. *J. Mater. Sci: Mater Electron* **2010**, *21*, 1014
9. P.H. Shih, S.Y. Wu. Growth Mechanism Studies of ZnO Nanowires: Experimental Observations and Short-Circuit Diffusion Analysis. *Nanomaterials (Basel)* **2017**, *7*, 188.

10. Y. Nie, Z. Wang, J. Wang, F. Bao, J. Zhang, Y. Ma, T.K. Sham, X. Sun. Synthesis and Structure-Dependent Optical Properties of ZnO Nanocomb and ZnO Nanoflag. *J. Phys. Chem. C*. **2017**, *121*, 26076
11. S. Kumar, P.D. Sahare, S. Kumar. Optimization of the CVD parameters for ZnO nanorods growth: Its photoluminescence and field emission properties. *Mater. Res. Bull.* **2018**, *105*, 237
12. G. Wang, N. Wu, J. Wang, J. Shao, X. Zhu, X. Lu, L. Guo. Abnormal change of melting points of gold nanoparticles confined between two-layer graphene nanosheets. *RSC Adv.* **2016**, *6*, 108343
13. B. Xiang, P. Wang, X. Zhang, S.A. Dayeh, D.P.R. Aplin, C. Soci, D. Yu, D. Wang. Rational Synthesis of p-Type Zinc Oxide Nanowire Arrays Using Simple Chemical Vapor Deposition. *Nano Lett.* **2007**, *7*, 323
14. V. Vaithianathan, J.H. Moon, C.H. Chang, K. Asokan, S.S. Kim. Electronic Structure of P-Doped ZnO Films with p-Type Conductivity. *J. Nanosci. Nanotechnol.* **2006**, *6*, 3422
15. Wang, Z., Guo, X., Sham, T.K. 2D XANES-XEOL mapping: observation of enhanced band gap emission from ZnO nanowire arrays. *Nanoscale* **2014**, *6*, 6531
16. B.H. Lin, X.Y. Li, D.J. Lin. *et al.* Investigation of Cavity Enhanced XEOL of a Single ZnO Microrod by Using Multifunctional Hard X-ray Nanoprobe. *Sci Rep.* **2019**, *9*, 207
17. J. Lee, D.C. Sorescu, X. Deng. Tunable Lattice Constant and Band Gap of Single and Few-Layer ZnO. *Phys. Chem. Lett.* **2016**, *7*, 1335

Chapter 5

5. Summary and Future Work

5.1. Summary

This thesis is focusing on studying the structure and optical properties of both n-type and p-type ZnO nano/microparticles which are prepared by hydrothermal and chemical vapor deposition (CVD) technique via vapor-liquid-solid (VLS) mechanism, respectively. The SEM and EDX have been applied to study morphology and elemental distribution of both undoped and P-doped ZnO samples. The XRD has been used to find the structure of ZnO crystallinity. The XANES and XEOL are applied to study phenomena with both element and chemical site specificities. Associated results and discussion are presented in chapter 3 and chapter 4.

In Chapter 1, I introduce some basic background of what ZnO semiconductor is, what advantages of ZnO semiconductors are, why we need to study the P-type ZnO semiconductor. I also introduce some basic background about ZnO synthesis techniques such as the hydrothermal synthesis and the CVD method. At the same time, there is some basic knowledge about synchrotron radiation which has been introduced in chapter 1 as well.

In Chapter 2, I introduce some photon sources and their beamlines such as 20BM in Advance Photon Source (APS), soft X-ray microcharacterization beamline (SXRMB) in Canadian Light Source (CLS) and 23A X-ray Nanoprobe in Taiwan Photon Source (TPS). I measurement my samples at these beamlines. I also present detailed information on synchrotron-based techniques such as XANES and XEOL. I introduce some basic knowledge of other characterization methods as well, such as XRD, SEM and EDX.

In Chapter 3, I present a study of both undoped and P-doped ZnO nano/microrods by XANES and XEOL. Two different doping levels and two reaction temperatures are introduced, respectively by the hydrothermal synthesis. The morphology features including size (width and length) are tracked by the SEM technique. The SEM images show the doping level and temperature did influence the sizing and length of both undoped and P-

doped ZnO nano/microrods, respectively. The influence of doping level and temperatures on the growth of ZnO nano/microrods are discussed. It is found that without the doping level and with the higher reaction temperature, ZnO nano/microrods produce a smaller value of average diameter. The laboratory XRD is used to study the structure of both undoped and P-doped ZnO crystallinity. According to the XRD results, the crystal structures for both undoped and P-doped ZnO are hexagonal, and the P is doped into ZnO lattice, producing a contracted lattice. The influence of doping level on the lattice for P-doped nano/microparticles are discussed; the relationship between the concentration of P ion and the 2θ shift in P doped ZnO lattice is in direct proportion.

More importantly, XANES is used to determine the local chemical environment and structure of both undoped and P-doped ZnO nano/microparticles across the Zn K-edge, Zn $L_{3,2}$ -edge, O K-edge and P K-edge. In general, both Zn K-edge and Zn $L_{3,2}$ -edge spectra show the feature for both P-doped and undoped ZnO products are very similar, which suggests the neighbour atom for Zn in ZnO lattice is not influenced by the P-doping and indicates the phosphorus does not substitute the oxygen. The O K-edge XNAES spectrum suggests the bonding neighboring atom affect the local environment of O which indicates that the phosphorus substitutes Zn in the ZnO lattice. The P K-edge XANES spectrum indicates that the oxidation state for P in P-doped ZnO samples is 5^+ which is powerful evidence that P substitute the Zn instead of the O in ZnO lattice because if the P substitute O in ZnO, then the lattice structure would become to PZn_4 like, and the oxidation state of phosphorus is 3^- . Both XANES and XRD results suggest the P doped into ZnO lattice and substitute the Zn. Furthermore, XEOL has also been used to determine the optical properties of undoped ZnO. According to XEOL spectra, undoped ZnO nanorods across the Zn K-edge and the intensity ratio (I_{NBE}/I_{DE}) with different X-ray energies, the intensity of defect emission (I_{DE}) is dominant when the X-ray energy is approaching the threshold. When the X-ray energy is higher than the threshold, the intensity of near bandgap emission (I_{NBE}) is dominant. This is due to the increase of the absorption and the thermalization of electrons and holes in the XEOL process [1]. According to the maximum of near bandgap emission (NBE), the bandgap for undoped ZnO is around 3.2eV.

In chapter 4, I present another study of both undoped and P-doped ZnO nano/microparticles by XANES and XEOL. Two gas flow rates and three substrate positions are introduced, respectively by the VLS method. SEM technique has also been used to track the morphology of features such as width and length. The SEM images show the gas flow rate and different substrate positions did influence the sizing and length of both undoped and P-doped ZnO nano/ microparticles, respectively. The influence of doping level and temperatures on the growth of ZnO nano/ microparticles are discussed; with the further substrate position, ZnO nano/ microparticles produce a smaller value of average diameter. The laboratory XRD is also used to study the structure of both undoped and P-doped ZnO crystallinity. According to the XRD results, the crystal structures for both undoped and P-doped ZnO products are hexagonal, and the P is doped into a slightly contracted ZnO lattice. Furthermore, XANES and XEOL are used to determine the structure and optical properties of both undoped and P-doped ZnO nano/ microparticles, respectively. In general, both undoped and P-doped ZnO products at Zn K-edge results shows a similar feature which suggests the neighbour atom for Zn in ZnO lattice is not influenced by the P-doping and indicates the phosphorus does not substitute the oxygen. The P K-edge XANES spectrum indicates the oxidation state for P in P-doped ZnO samples is 5^+ which proves that P substitute the Zn in ZnO lattice. According to the XEOL spectrum, undoped and P-doped ZnO products have different features across the Zn K-edge. By looking at the feature and intensity ratio ($I_{\text{NBE}}/I_{\text{DE}}$) of undoped ZnO products, the intensity of defect emission (I_{DE}) is dominant during the whole process. This is due to the imperfect crystallinity of undoped ZnO products. By looking at the feature and intensity ratio ($I_{\text{NBE}}/I_{\text{DE}}$) of P-doped ZnO products, the intensity of near bandgap emission (I_{NBE}) is dominant during the whole process. This may be due to the P dopant helps ZnO to improve its crystallinity after thermalization. By comparing intensity ratio ($I_{\text{NBE}}/I_{\text{DE}}$) between undoped and P-doped ZnO products, the trend of intensity ratios between undoped and P-doped ZnO are opposite which may also suggest the P dopant changes the optical properties of ZnO structures. The P-doped ZnO products have better crystallinity and less oxygen-based surface defect than the undoped ZnO products. By looking at the maximum of NBE for both undoped and P-doped ZnO products respectively, P-doped ZnO structures have a smaller bandgap (3.21eV) than undoped ZnO structures (3.22eV).

5.2. Future Work

Semiconductor nanostructures have attracted extensive attraction because they can transport electrons/holes and function as building blocks for nanoscale electronics and optoelectronics assembled without the need for complex and costly fabrication facilities. ZnO semiconductors and their derivatives have been extensively developed due to their potential use in water-splitting, solar cells, and sensor applications. However, due to its native defects, such as zinc interstitial and oxygen vacancy, ZnO is well known as the intrinsic n-type semiconductor [2-4]. Therefore, how to synthesize high-quality p-type ZnO semiconductors with doping and investigate their optoelectronic properties and local chemical structures are important and necessary.

This thesis is focusing on synthesizing p-type ZnO semiconductors by introducing P ions as the dopant. Two synthesis methods (hydrothermal method and CVD technique) have been used; several experimental conditions have been applied to find the best structure and optical properties of P-doped ZnO nano/microparticles, respectively. Based on the current study, further optical measurements need to be applied to discover the optoelectronic properties of P-doped ZnO nano/microparticles more detailly.

Base on the above suppose XEOL measurements across P K-edge and P $L_{3,2}$ -edge can be applied at CLS, SXRMB and VLS-PGM (Variable Line Spacing Plane Grating Monochromator) beamlines, respectively. SXRMB beamline has already been introduced in chapter 1. All FY and TEY XANES spectrum for P-doped ZnO nano/microparticles at P K-edge are measured at SXRMB beamline. Therefore, to study the role of P in P-doped ZnO nano/microparticles for both structure and optical properties; SXRMB can give high-quality information by measuring both XANES and XEOL, respectively. VLS-PGM is another operating beamline in CLS. The energy range for this beamline is between 5.5 – 250 eV [5] which is perfect to measure the P $L_{3,2}$ -edge. Therefore, to study both structures and optical properties of P in P-doped ZnO nano/microparticles, VLS-PGM can provide the information of P more detailly.

5.3. Reference:

1. Z. Wang, X. Guo, T.K. Sham. 2D XANES-XEOL mapping: observation of enhanced band gap emission from ZnO nanowire arrays. *Nanoscale*, **2014**, 6, p. 6531
2. T. Lim, P.S. Mirabedini, K. Jung, P.A. Greaney, A.A. Martinez-Morales. High-index crystal plane of ZnO nonpyramidal structures: Stabilization, growth, and improved photocatalytic performance. *Appl. Surf. Sci.* **2021**, 536, 147326
3. Z. L. Wang, J. H. Song. Piezoelectric Nanogenerators Based on Zinc Oxide Nanowire Arrays. *Science*. **2006**, 312, 242
4. S. Brahma, Y.W. Yeh, J.L. Huang, C.P. Liu. Cu-doped p-type ZnO nanostructures as unique acetone sensor at room temperature (~25 °C). *Appl. Surf. Sci.* **2021**, 564, p. 150351
5. Variable Line Spacing Plane Grating Monochromator. Overview. https://www.lightsource.ca/beamlines/details/variable_line_spacing_plane_grating_monochromator_vls_pgm.html (accessed by July. 10th. 2021)

Curriculum Vitae

Name: Zhi Liang Dong

Post-Secondary Education and Degrees: The University of Western Ontario
London, Ontario, Canada
2019-present M.Sc. Candidate
The University of Western Ontario
London, Ontario, Canada
2013-2019 B.Sc.

Research Experience: Teaching Assistant
The University of Western Ontario
2019-2021
Synchrotron experiment experience
Canadian Light Source (CLS, SK, Canada)
2019-2020
Advanced Photon Source (APS, IL, U.S.A)
2019

Grants and Awards: Graduate research assistantship
The University of Western Ontario
2019-2021
University Entry Scholarship
2013

Publication:

Ya-Kun Wang, Chen-Chao Huang, Sarvendra Kumar, Si-Hua Li, Zhi-Liang Dong, Man-Keung Fung, Zuo-Quan Jiang, Liang-Sheng Liao. Thermally activated delayed fluorescence sensitizer for D-A-A type emitter with orange-red light emission. *J. Mater. Chem. C*, **2018**, 6, p.10030-10035